Magnetic microvortex for convective transport of molecules : towards a biomedical application

Maxime Raboisson-Michel

UNIVERSITÉ CÔTE D'AZUR

ÉCOLE DOCTORALE
SCIENCES FONDAMENTALES ET APPLIQUÉES

THÈSE DE DOCTORAT

Micro-vortex magnétique pour le transport convectif de molécules : vers une application biomédicale

Maxime Raboisson-Michel

Institut de Physique de Nice (INPHYNI) /Axlepios Biomedical

Présentée en vue de l'obtention du grade de docteur en Physique d'Université Côte d'Azur

Dirigée par : Kuzhir Pavel

Soutenue le : 13 Décembre 2022

Devant le jury, composé de :
Micheline ABBAS, Maître de conférences HDR, Université de Toulouse
Pavel KUZHIR, Maître de conférences HDR, Université Côte d'Azur
Modesto LOPEZ-LOPEZ, Professeur des universités, Université de Grenade
Alain PONTON, Directeur de recherche, Université Paris Diderot
Christophe RAUFASTE, Professeur des Universités, Université Côte d'Azur
Andrey ZUBAREV, Professeur des universités, Université fédérale de l'Oural

Université Côte d'Azur

École Doctorale de Sciences Fondamentales et Appliquées

(EDSFA) Institut de Physique de Nice (INPHYNI)

Thèse de doctorat

Présentée en vue de l'obtention du grade de docteur en physique de l'Université Côte d'Azur par

Maxime Raboisson-Michel

Magnetic micro vortex for convective transport of molecules: towards a biomedical application

Dirigée par Dr. Pavel Kuzhir

Soutenue le 13 Décembre 2022

JURY :

Président :
Christophe RAUFASTE, Maître de conférences, Université Côte d'Azur

Rapporteurs
Micheline ABBAS, Maître de conférences, Université de Toulouse
Alain PONTON, Directeur de recherche, Université Paris Diderot

Examinateurs
Modesto LOPEZ-LOPEZ, Professeur des universités, Université de Grenade
Andrey ZUBAREV, Professeur des universités, Université fédérale de l'Oural

Directeur de thèse
Pavel KUZHIR, Maître de conférences, Université Côte d'Azur

AXLEPIOS BIOMEDICAL

Abstract

Ischemic stroke is the first disabling disease in France and accounts for 87% of all strokes. An ischemic stroke occurs when a thrombus, a fatty deposit lining the vessel walls, detaches and obstructs a blood vessel, blocking the blood flow and preventing the neighbouring tissues' oxygen supply, resulting in necrosis. The intravenous injection of tissue plasminogen activator, a serine protease that dissolves clots, during the first 3-4,5 hours following an event is crucial for the success of therapeutic treatment. However, such a method does not allow the efficient diffusion (more than 60 min) of the drug to the clot due to the stagnation of blood in the clogged vessel. Using magnetic iron oxide nanoparticles (IONP) can be very efficient in accelerating the transport of the drug in the occluded vessel. The idea is to rotate the elongated aggregates of the IONP by an oscillating magnetic field applied via the electric coils placed outside.

In this manuscript, we first reviewed the application and relevance of magnetic colloids in the biomedical field to help us understand the physical interactions of the particles with the magnetic field and the clot. This work allowed us to design an experimental setup that facilitated the characterization and manipulation of aqueous dispersions of synthesized magnetic IONPs in a closed *in-vitro* environment rudimentary simulating a blood vessel. Most of the thesis work was done on the analysis of the experimental data and their compliance to the elaborated theoretical models: the self-assembly of IONP into elongated aggregates under the action of a rotating magnetic field; collective rotation of these aggregates, as well as the creation of a recirculating flow in a closed channel, mimicking a blocked blood vessel. We finally tested the system based on polymer calcium alginate beads, used as a simple proxy for the physical model of blood clot dissolution and proof of concept of the proposed thrombolysis technique. Quantitatively, we manage to create the IONP rotating aggregates (of an average length of about 50 μm) in a very short time-lapse (about 1 min) elapsed from the moment when a rotating magnetic field of an amplitude 6 kA/m and frequency 5 Hz is applied; these aggregates are capable of generating the flows in a closed channel at a typical speed of 5-10 μm/s; these flows have been proved to enhance the mass transport of a dissolution reagent (trisodium citrate) towards a polymeric calcium alginate bead, such that its dissolution time decreases at least by order of magnitude with respect to that in the absence of the magnetic field when the dissolution agent is delivered to the bead through diffusion through a quiescent liquid medium. These results are finally extrapolated to the thrombus system, i.e., a fibrine clot in a blood medium dissolved by a thrombolytic drug.

Keywords: ischemic stroke, magnetic iron oxide nanoparticles aggregates, recirculatory flow

Résumé

L'accident vasculaire cérébrale (AVC) ischémique est la première maladie invalidante en France et représente 87 % de tous les AVC. Un AVC ischémique survient lorsqu'un thrombus, un dépôt graisseux tapissant les parois des vaisseaux, se détache et obstrue un vaisseau sanguin, bloquant le flux sanguin et empêchant l'apport d'oxygène aux tissus voisins, entraînant leur nécrose. L'injection intraveineuse d'activateur tissulaire du plasminogène, une sérine protéase qui dissout les caillots, au cours des 3 à 4,5 premières heures suivant un événement est cruciale pour le succès du traitement thérapeutique. Cependant, une telle méthode ne permet pas la diffusion efficace (plus de 60 min) du médicament vers le caillot en raison de la stagnation du sang dans le vaisseau obstrué. L'utilisation de nanoparticules magnétiques d'oxyde de fer (NPOF) peut être très efficace pour accélérer le transport du médicament dans le vaisseau occlus. L'idée est de faire tourner les agrégats allongés de NPOFs par un champ magnétique oscillant appliqué via des bobines électriques placées à l'extérieur.

Dans ce manuscrit, nous avons d'abord examiné l'application et la pertinence des colloïdes magnétiques dans le domaine biomédical pour nous aider à comprendre les interactions physiques des particules avec le champ magnétique et le caillot. Ce travail nous a permis de concevoir un montage expérimental qui a facilité la caractérisation et la manipulation de dispersions aqueuses d'NPOFs magnétiques synthétisés dans un environnement fermé in-vitro rudimentaire simulant un vaisseau sanguin. L'essentiel du travail de thèse a porté sur l'analyse des données expérimentales et leur conformité aux modèles théoriques élaborés : l'autoassemblage des NPOFs en agrégats allongés sous l'action d'un champ magnétique tournant ; rotation collective de ces agrégats, ainsi que la création d'un flux de recirculation dans un canal fermé, imitant un vaisseau sanguin bloqué. Nous avons enfin testé le système à base de billes d'alginate de calcium polymère, utilisé comme simple proxy du modèle physique de dissolution du caillot sanguin et preuve de concept de la technique de thrombolyse proposée. Quantitativement, nous parvenons à créer les agrégats tournants NPOF (d'une longueur moyenne d'environ 50 µm) dans un laps de temps très court (environ 1 min) écoulé à partir du moment où un champ magnétique tournant d'une amplitude 6 kA/m et d'une fréquence 5 Hz est appliqué ; ces agrégats sont capables de générer les écoulements en canal fermé à une vitesse typique de 5-10 µm/s ; il a été prouvé que ces flux améliorent le transport de masse d'un réactif de dissolution (citrate trisodique) vers une bille d'alginate de calcium polymère, de sorte que son temps de dissolution diminue au moins d'un ordre de grandeur par rapport à celui en l'absence de champ magnétique lorsque le l'agent de dissolution est délivré à la perle par diffusion à travers un milieu liquide au repos. Ces résultats sont finalement extrapolés au système thrombus, c'est-à-dire un caillot de fibrine dans un milieu sanguin dissous par un médicament thrombolytique.

Mots-clés : accident vasculaire cérébrale ischémique, agrégats de nanoparticules magnétiques d'oxyde de fer, flux re-circulatoire

Remerciements

Je souhaite tout d'abord remercier sincèrement le Dr. Micheline Abbas et le Dr. Alain Ponton qui ont accepté d'être rapporteurs de cette thèse. J'adresse également mes remerciements aux Dr. Modesto Lopez, Dr. Christophe Raufaste et au Dr. Andrey Zubarev qui complètent le jury de thèse en tant qu'examinateurs. Je suis très reconnaissant de bénéficier de leur expertise.

J'aimerais remercier tout particulièrement mon directeur de thèse, le Dr. Pavel Kuzhir pour m'avoir permis de poursuivre cette thèse dans les meilleures conditions en m'accueillant au sein de son équipe. Je voudrais en profiter pour saluer son dévouement, sa compétence et sa pédagogie qui sont un privilège que je ne mérite pas. Je ne saurais assez te remercierai pour ta patience et ton soutien au cours de ces quatre années. Cela a été un honneur d'apprendre sous ta tutelle !

J'adresse de grands remerciements à nos collègues de l'équipe parisienne du laboratoire PHENIX, le Dr. Agnes BEE et le Dr. Delphine Talbot, pour nous avoir fourni le ferrofluide colloïdale qui a servi aux expérimentations de cette thèse.

Merci également Yaroslava Izmaylov et Cyrille Claudet pour leur expertise en microfluidique, vos conseils avisés m'auront permis de mener à bien cette thèse. Merci aussi à Sandra Bosio pour l'élaboration et la réalisation des diverses pièces utilisées dans nos systèmes.

Je tiens aussi à adresser mes remercîments à Sebastien Schaub, responsable du plateau de microscopie, qui grâce à son expertise, nous a sauver de nuits interminables d'analyses d'images.

Car l'on garde toujours les meilleurs pour la fin, je tiens à remercier Gregory Verger-Dubois qui as cru en moi et m'as donné l'occasion de développer Axlepios Biomedical. La dernière dédicace revient à Jordy Queiros Campos, plus connu sous le nom d'Ask Jesus, le bras droit de ma main gauche qui aura rendu ces quatre années mémorables et remplies de souvenirs impérissables.

Table of contents

List of abbreviations

AC:	Alternating current
CMOS:	Complementary metal oxide semiconductor
CT:	Computed tomography
DLS:	Dynamic Light Scattering
FDA:	Food and Drug Administration
FUS:	Functional ultrasound
HCl:	Hydrochloric acid
ICP-OES:	Inductive Coupled Plasma – Optical Emission Spectrometry
IONP:	Iron oxide nanoparticle
LED:	Light-emitting diode
MPI:	Magnetic particle imaging
MRI:	Magnetic resonance imaging
NaCl:	Sodium chloride
PDMS:	Poly dimethyl siloxane
PET:	Positron emission tomography
PIV:	Particle image velocimetry
SPECT:	Single photon emission computed tomography
SPION:	Superparamagnetic iron oxide nanoparticle
tPA:	Tissue Plasminogen Activator
uPA:	Urokinase-type plasminogen activator
VSM:	Vibrating Sample Magnetometry

List of Figures

List of tables

Preface

During a brain stroke, blood clots form in the blood vessels that block blood flow and prevent oxygen supply to the brain. The success of therapeutic treatment in the first hours after stroke depends on the effectiveness of the active ingredient delivery to dissolve clots as fast as possible. Intravenous administration of the active substance does not allow the rapid diffusion of the drug to the clot because of the blood stagnation in clogged vessels. The delivery of the active ingredient is all the more problematic in the peripheral areas of the brain responsible for motor functions. Using magnetic iron oxide nanoparticles (IONP) can be very efficient in accelerating the transport of the drug in clogged peripheral vessels. The idea is to rotate the elongated aggregates of the IONP by an oscillating magnetic field applied via the electric coils placed outside. The technique can be coupled with magnetic resonance imaging (MRI) or magnetic particle imaging (MPI), especially since IONP is commonly used as a contrast agent. A relatively modest (but promising) advance in developing this cutting-edge technology has been done by a few scientific and R&D groups worldwide. However, the main physical aspects of this application, related to self-assembling magnetic colloids, dynamics of the magnetic assemblies, field-induced flow, and field-enhanced mass (drug) transport, have never been systematically studied.

In the present manuscript, we develop a microfluidic in vitro model, allowing rigorous experimental monitoring of these phenomena to fill this gap. The obtained experimental correlations are, whenever possible, completed by theoretical modelling to ensure a deeper insight into the topic and bring a necessary physical background for the future development of the target application[1].

The manuscript is organized as follows. Chapter 1 will review some in vivo applications of magnetic colloids along with the physical aspects relevant to those applications. We will also formulate the thesis objectives given lacking physical understanding of the target application. Chapter 2 will describe the synthesis and characterization of IONP used in all our experiments and the experimental setup, measuring, and data processing protocols. Chapters 3 to 5 will report the results of physical experiments and modelling of the phenomena related to the proposed technique of magnetically assisted thrombolysis, namely the formation and growth of

[1] The thesis work makes a part of the R&D project aimed at the technology prototyping and conducted in the frame of the collaboration project between the French CNRS and the Axlepios Biomedical start-up

self-assembled magnetic aggregates (Chapter 3), generation of recirculated flows in a closed channel (Chapter 4), and enhanced mass transport and polymer bead dissolution using magnetic colloids under an applied rotating magnetic field (Chapter 5). Notice that the polymeric (calcium alginate) beads serve us as a physical model of a blood clot and allow proof of concept of the proposed thrombolysis technique, even though considerable work still must be done to validate this concept *in vivo* on actual fibrine clots. At the end of the manuscript, we present general conclusions and outline a few critical perspectives for future developments.

Chapter 1. Magnetic colloids: biomedical applications and related physical phenomena. Thesis objectives

Magnetic colloids are suspensions of magnetic nanoparticles in a liquid carrier. The nanoparticle material can differ from classical iron oxide to less magnetic goethite or more magnetic cobalt ferrite. In most cases, monodomain nanocrystals are used as magnetic nanoparticles ensuring the superparamagnetic behaviour of the whole colloid. Magnetic nanoparticles used in biomedical applications are usually synthesised using a variety of chemical routes, which give, generally liquid dispersions of nanoparticles rather than dry powders of nanoparticles. Furthermore, these nanoparticle dispersions are continuously injected into or mixed with liquid-like or gel-like physiological media (phosphate buffers, blood, cerebrospinal fluid, soft biological tissues). In this context, it is irrelevant to consider the magnetic nanoparticle behaviour disconnected from their dispersing liquid, provided that interparticle colloidal interactions are strongly mediated by the solvent and its constitutive molecular entities (ions, proteins, etc.). Therefore, it is essential to graft specific chemical ligands on the magnetic nanoparticle surface to ensure their colloidal stability, biocompatibility, and specific biological function (drug delivery, hyperthermia, gene transfection and others). Suppose one achieves perfect colloidal nanoparticle stability once injected into the target biological medium. In that case, one can consider the ensemble of nanoparticles with the dispersing liquid as a ferrofluid, conventionally defined as a stable colloidal dispersion of magnetic nanoparticles [Rosensweig (1985)].

Considering colloidal aspects of magnetic dispersions, we will review in this chapter a few of their biomedical applications [Sec. 1.1] with a particular focus on magnetically assisted thrombolysis. We will then review important physical behaviours occurring in this last application [Sec. 1.2]. Finally, the literature survey of Sec. 1.2 will allow us to summarise the unresolved issues of this topic and formulate the thesis objectives [Sec. 1.3].

1.1 In vivo biomedical applications of magnetic colloids

Since the early 2000th, magnetic colloids have had various *ex vivo* applications in magnetic cell separation, protein purification, gene transfection, and immunoassays. However, *in vivo* applications are more challenging because of the vital importance of all the safety aspects related to the administration, immune response, and metabolism of magnetic nanoparticles in a human organism. Since the present manuscript constitutes physical bases of magnetic nanoparticle applications in blood clot dissolution, we will briefly review in this Section only a

few *in vivo* applications that are somehow connected to our target application. Namely, the thrombolysis by magnetic nanoparticles should likely be coupled to medical imaging (Sec. 1.1.1) for a more straightforward magnetic particle guiding the affected regions and real-time observation of the clot dissolution process. On the other hand, cancer therapy (Sec. 1.1.2) employs several techniques that could be extremely useful for the thrombolysis application, such as: (a) magnetic drug delivery to guide magnetic nanoparticles and active substance to the target sites; (b) magnetic hyperthermia that can be used for the localised controlled release of the drug from nanoparticle surface near the blood clots; (c) magnetolysis of cancer cells, which employs rotating magnetic fields for involving magnetic particles into spinning motion to destroy the membranes of the tumour cells mechanically –similar mechanical destruction of blood clots can be in principle realised in our application. Finally, a few existing works on magnetic field-induced thrombolysis will be reviewed in Sec. 1.1.3.

1.1.1 Imaging

Early medical prognostic of diseases is a crucial factor for the increased probability of successful treatment and is often due to the revolutions intervening in the medical imaging technologies. As one of the most American Food and Drug Administration (FDA)-approved nanomedicines material [Montiel Schneider et al. (2022)], iron oxide nanoparticles (IONP) are playing a significant role in the evolution of those imaging techniques such as X-ray radiography, computed tomography (CT), magnetic resonance imaging (MRI), functional ultrasound (FUS) imaging, positron emission tomography (PET), single photon emission computed tomography (SPECT), and fluorescence imaging. At diameters exceeding the renal clearance (from 15 nm and no more than 100 nm), IONPs, which are mainly made of magnetite ($Fe3O_4$) or maghemite (γ-Fe_2O_3), have proved to be effective as contrast agents, drug delivery vehicles, and thermal-based therapeutics [Li et al. (2018)]. It gives them multiple exciting properties, such as more prolonged circulation in the vascular system leading to higher uptake in leaky vasculature regions [Goel et al. (2011)] and an increased surface area (cf. Fig. 1) available for ligand binding or drug/probe coupling.

The biocompatibility and stability are filling the niche of applications that requires properties impossible by organic materials. However, they are restricted for some clinical applications by low solubility and toxicity effects.

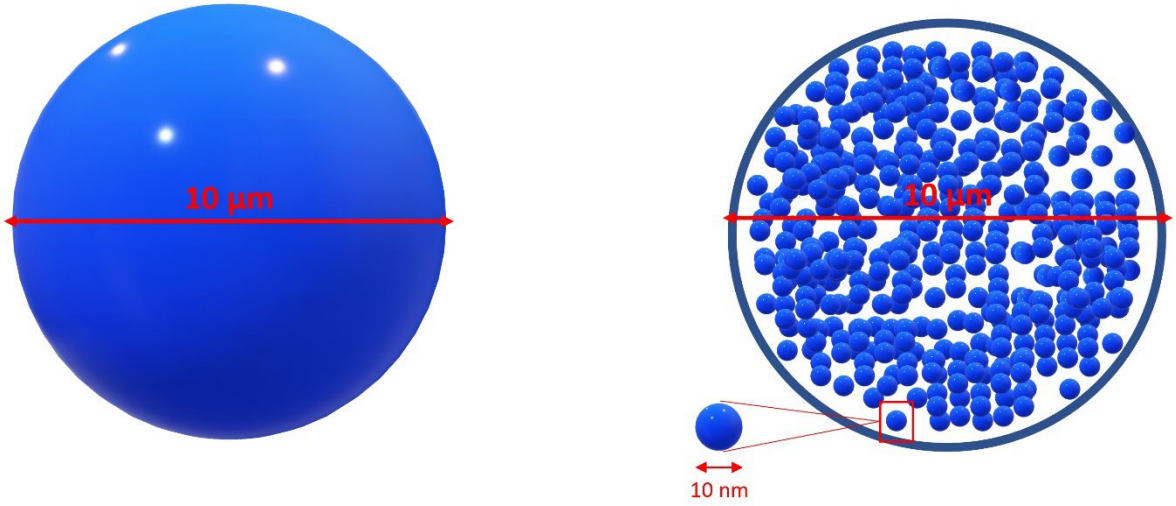

Figure 1.1: Illustration of the high ratio of surface area to volume with a smaller particle size

Different types of IONPs have numerous broad advantages and disadvantages regarding cargo, delivery, and patient response [Revia and Zhang (2016)] in a target biomedical imaging or theragnostic technique. The superparamagnetic properties of IONP are broadly used for diagnosis, drug delivery and therapy. Likewise, theragnostic multifunctional IONPs brand them a proper dual agent.

Thus, ferric oxide-based contrast agents reduce T2 relaxation time in MRI to produce dark images on T_2-weighted imaging to create a 'negative' MRI contrast [Szpak et al. (2014)]. These SPIONs have a size ranging between 10 and 300 nm. However, extra small monocrystalline IONPs of a size smaller than 5 nm can be potentially used as positive contrast agents [Shen et al. (2017)]. Ferric oxide MRI contrast agents have been used in various imaging applications, such as molecular imaging, gene monitoring, cell tracking, blood pool imaging, lymph node identification and cancer diagnosis [Korchinski et al. (2015)].

In FUS imaging, IONPs are employed as contrast agents, alternative to commonly used gas microbubbles, as long as they can reach extravascular targets when magnetic field gradients pull them. The IONPs are recognised to extend possibilities for molecular imaging, where the contrast agent is labelled with specific antibodies so that pathologic tissue may be visualised directly [Sjöstrand et al. (2020)]. The fUS imaging can be coupled with US hyperthermia – an efficient method of cancer treatment by local temperature elevation, in which the IONPs are

used as efficient sonosensitizers, i.e. the nanoobjects enhancing the attenuation and dissipation of acoustic energy [Kaczmarek et al. (2018)].

Another emerging imaging technique relevant to our target application is magnetic particle imaging (MPI), based on the magnetic detection of IONP tracers within the biological tissue. This technique is currently considered one of the most adapted for functional brain imaging. It has the enormous advantage of being free of any background noise at high-speed scan rates [Neumann et al. (2022)].

1.1.2 Cancer Therapy

The main cancer therapy methods employing IONPs are magnetic drug delivery, magnetic hyperthermia and magnetolysis of cancer cells, in which the cancer cell apoptosis is achieved through chemical, thermal or mechanical stimuli. Each of these three methods is still under active development and can be applied either separately or in combination with another method like, for example, magnetic hyperthermia, which is often preceded the magnetic drug delivery. These magnetically assisted therapies have an advantage over classical chemo- or radiotherapy to mostly target cancer cells, minimally affecting healthy tissues.

The past 15 years have seen a tremendous rise in the application of nanotechnologies in the field of drug delivery, either in the application of cell targeting or functionalised nanoparticles to carry a specialised drug [Douziech-Eyrolles et al. (2007)]. Those characteristics are essential in cancer therapy to limit the tumours' development of multidrug resistance and diminish the chemotherapy side effect. The detrimental effects of chemotherapy come from the fact that the drugs used are non-specific, and their cytotoxicity affects all cells in the neighbouring treatment site [Momtazi (2014). One of the prominent actors in this domain is the magnetic nanoparticles: being susceptible to an applied magnetic field means they can be directed at the affected zone and thus reduce the "spillage" of the non-specific chemotherapeutic agents [Douziech-Eyrolles et al. (2007)]. To ensure maximal efficiency of this system, the IONPs must have a diameter ranging from 10 to 40 nm: not too small to fall through gap junctions or cleared off from the renal system nor too big, so they exhibit superparamagnetic behaviour. Otherwise, they would remain in their aggregated form after the magnetic field is turned off and targeted by macrophages [Momtazi (2014)].

The primary constraint for manipulating magnetic nanocarriers in cancer treatments comes from their mode of transportation: being injected into the vascular system means they are subject to the hydrodynamic conditions of the blood flow. Previous theoretical works

[Estelrich et al., (2015)] stipulate that the magnetic field intensity at the site should be in the order of 160-560 $kA.m^{-1}$ with gradients along the z-axis depending on the blood flow rates (0.5-1.5 $mm.sec^{-1}$ in brain capillaries).

Notably, the physicochemistry of IONPs with loaded drugs can considerably influence their magnetophoretic mobility under applied external magnetic field gradients. Thus, our recent studies show a synergy between curcumin drug uptake and enhanced remote control over IONPs thanks to the curcumin-assisted formation of small IONP agglomerates, which promote easy phase separation and increase the magnetophoretic mobility significantly under applied magnetic fields [Queiros Campos et al. (2021b)].

At the beginning of the 21st century, magnetic fluid hyperthermia was a new approach to deep tissue cancer hyperthermia treatment. While it was common to employ microwave heating, the homogeneity of the procedure was lacking, and nanoparticles were a much finer tool [Jordan et al. (2001)]. Hyperthermia is the heating of targeted tumour cells at 42-45°C for a few hours in association with chemotherapy or irradiation to enhance their effects such as protein denaturation, co-aggregation, increased permeability, or cascade pathways inhibition [Chang et al. (2018)]. On the other hand, thermoablation destroys the cells by exposing them to temperatures exceeding 50°C for a few minutes. Magnetic nanoparticles dissipate thermal energy by magnetic losses through the phenomenon of hysteresis heat loss and the Néel and Brownian relaxation loss, otherwise called relaxation losses. Heat generation is tied to the structure of the particles: size, shape, and surface functionalisation, as well as their magnetic properties: saturation, susceptibility, and anisotropy [Rajan et al. (2020)]. High AC fields of low frequency (100-300 kHz) are used to minimise the concentration of nanoparticles injected while reaching the desired temperature [Hergt et al. (2006)].

An alternative technique, magnetolysis, or mechanical destruction of cancer cells by magnetically actuated IONP, has recently been proposed. Unlike magnetic hyperthermia, this technique operates at low amplitude (~10 mT) and low frequency (~10 Hz) alternating magnetic fields. Different shaped IONPs have been tested in this application, Going from spindle-like iron micro-rods [Wang et al. (2013)] to disk-like NiFe micro vortex nanoparticles [Leulmi et al. (2015)] or rectangular-shaped Fe-Cr-Nb-B superferromagnetic nanoparticles [Chiriac et al. (2018)]. The particles were subjected to translational or spinning motion through the application of uniaxial oscillating or rotating magnetic fields, respectively, that allowed the breaking of the tumour cell membrane and lead to a drastic decrease in tumour cell viability. The physical

limitations of this technique are extensively studied in the PhD thesis of [Wang (2012)] in terms of a phase diagram showing different dynamic regimes of the spindle-like particles as a function of the ambient medium rheology and frequency of the applied magnetic field. For the rotating magnetic fields, it could be concluded that the low-frequency regime (with magnetic particles synchronously rotating with the field) usually provides the best performance for membrane destruction. This information is crucial for possible erosive destruction of the blood clots under hydrodynamic fluxes created by rotating magnetic assemblies, as will be inspected in Chapter5.

1.1.3 Magnetically assisted thrombolysis

Another key potential biomedical application of IONPs concerns the blood clot lysis in blocked vessels, the application of the significant interest of the present manuscript. The classical treatment by intravenous injection of a thrombolytic drug appears to be relatively inefficient because of slow diffusive drug transport along a blocked vessel in the absence of flow through this vessel [Gräfe et al. (2016)]. It has been recently proposed to use magnetic nanoparticles actuated by an external rotating magnetic field to induce a recirculation flow in the blocked vessel [Creighton (2012); Cheng et al. (2014); Creighton et al. (2020)]. Indeed, the nanoparticles must be able to self-assemble into elongated aggregates that must spin with the rotating field. In some conditions, the aggregate rotation is expected to induce recirculation flows, "pumping" the thrombolytic drug from non-obstructed vessels towards the blood clot through the blocked vessel. Some preliminary *in vitro* studies have shown that the induced flows may cause the mechanical erosion of the thrombus [Gabayno et al. (2015)] or enhance its chemical lysis through accelerated drug delivery [Cheng et al. (2014); Li et al. (2018)], while preliminary *in vivo* tests confirm three times faster lysis of a blood clot formed in rabbit jugular vein [Creighton (2012)]. Alternatively, magnetic aggregates have been shown to form a dense cloud in artificial blood network under combined rotating and gradient magnetic fields; this cloud can translate along the vessels with speed as high as ~0.5 cm/s that is very beneficial for drug delivery through the blocked vessels [Pernal et al. (2020); Willis et al. (2020)]. Despite promising advancements in this cutting-edge biotechnology, the physics of the flow generation and drug transport by rotating magnetic aggregates remains almost unexplored.

1.2 Physical phenomena encountered in magnetically assisted thrombolysis

According to a brief conceptual description of the blood clot lysis application [Sec. 1.1.3], a variety of physical phenomena related to magnetic particle actuation is encountered in this technique. A few of them, most relevant for the current manuscript, are briefly reviewed in the present Section: field-induced self-assembly of magnetic nanoparticles and kinetics of field-

induced aggregation [Sec. 1.2.1], dynamics of magnetic aggregates under rotating magnetic fields [Sec. 1.2.2] and field-induced recirculation flows in magnetic colloids [Sec. 1.2.3].

1.2.1 Equilibrium and kinetics of field-induced self-assembly of magnetic nanoparticles

In most biomedical applications, magnetic nanoparticles are subject to field-induced phase separation manifested through the self-assembly of individual nanoparticles into micrometre-sized particle aggregates with an anisotropic shape. From the thermodynamics perspective, such a phase separation or self-assembly is considered a condensation phase transition, with appropriate phase diagrams and equilibrium microstructures extensively studied theoretically and experimentally [Tsebers (1982); Buyevich et al (1990); Liu et al. (1995); Hong et al. (1997); Zubarev and Iskakova (2002); Hynninen and Dijkstra (2005); Dubois et al. (2000); Cousin et al. (2001, 2003); Prokopieva et al. (2009); Holm and Weis (2005)]. Such self-assembly is a necessary phenomenon for some applications (probing of intracellular viscoelasticity and lysis of blood clots) and is a parasite phenomenon for other applications (immunoassays and hyperthermia). In any event, the knowledge of the aggregation timescale is crucial for successfully realising a given application. This requires a detailed study of the kinetics of the phase separation process. Such kinetics is quite well documented in the case of a permanent magnetic field. Experimental studies by light scattering or direct optical visualisation on 10 nm–20 nm-sized nanoparticles revealed elongated scattered patterns ascribed to long drop-like aggregates whose growth with time was limited by lateral dipolar repulsion between them [Socoliuc and Bica, 2002; Laskar et al. (2010); and Vinod and Philip, (2019)]. This contradicts the long-time observation by [Swan et al. (2012)] under microgravity conditions when all the aggregates coalesced into a single bulk phase. Similar experiments on superparamagnetic nanoclusters or nano-emulsion droplets of 30 nm–200 nm-size range also revealed the appearance of long needle-like aggregates growing with time due to the absorption of single nanoclusters from the dilute phase surrounding the aggregates followed by the coalescence of aggregates due to dipolar attractions. This coalescence was, however, hindered for a long time by dipolar repulsion [Socoliuc et al. (2013); Ezzaier et al. (2017); Ezzaier et al. (2018); and Mohapatra and Philip, (2019)].

From a theoretical perspective, the driving force of the field-induced phase separation is the supersaturation $\Delta = \varphi - \varphi'$, which is defined as the difference between the nanoparticle volume fraction φ of the phase separating colloid and φ'—the threshold volume fraction below which there is no phase separation. The term φ' is nothing but the equilibrium concentration of the dilute phase at the end of the phase separation process. In their works, Zubarev and Ivanov

(1997) and Ivanov and Zubarev (1997) have considered the homogeneous nucleation and aggregate growth through the diffusion of nanoparticles (15 nm–20 nm) toward the aggregates, followed by Ostwald ripening, allowing the formation of a concentrated bulk phase. They have established the scaling laws for the average aggregate volume as a function of time at the aggregate growth stage, $\langle V \rangle \propto t^{7/4}$, and at the Ostwald ripening stage, $\langle V \rangle \propto t^{7/6}$. Later, Ezzaier et al. (2017) modelled the kinetics of aggregation of relatively large superparamagnetic nanoclusters (~50 nm). They have established that the diffusive flux dominates over the magnetophoretic one for the aggregate growth stage. The coalescence of aggregates on longer timescales conducts a high-speed aggregation, with $\langle V \rangle \propto t^{7/2}$ and dominates over the Ostwald ripening in agreement with experiments.

A series of publications have been devoted to equilibrium structures and kinetics of phase separation in pulsed unidirectional fields with a rectangular waveform. Depending on the ratio between the "field on" and "field off" periods, needle-like ellipsoidal aggregates [Promislow and Gast (1997)], percolated or columnar structures [Swan et al. (2014)], or even branched structures perpendicular to the applied field [Kim et al. (2020)] have been observed and predicted through numerical simulations [Sherman and Swan (2016). The average width $\langle s \rangle \propto t^m$ of these structures shows modest diffusion-limited growth at the beginning with $m \approx 1/4$–$1/3$, followed by a faster growth due to coalescence with $m \approx 3/2$ [Swan et al. (2014); Kim et al. (2020)]. To the best of our knowledge, the kinetics of phase separation has never been studied in rotating magnetic fields. However, "steady-state" dynamics of the magnetic self-assemblies under rotating magnetic fields are relatively well documented, as revised in the next Sec. 1.2.2.

1.2.2 Dynamics of magnetic self-assemblies under rotating fields

Like their behaviour in the permanent field, the rotating field at a relatively low frequency gathers magnetic nanoparticles into elongated drop-like aggregates that rotate synchronously with the field [Sandre et al. (1999)]. However, the final state of a magnetic colloid is considerably different. In a permanent field, all the aggregates coalesce into the concentrated bulk phase, and the system settles in its equilibrium ground state with minimal energy [Swan et al. (2012)]. In a rotating field, the formation of the concentrated bulk phase seems to be hindered by hydrodynamic repulsion between rotating aggregates. Stikuts et al. (2020) have recently observed that the magnetic droplets do not coalesce but organise themselves into a crystalline structure. They argue that a balance between attractive magnetic dipolar and repulsive hydrodynamic interactions is responsible for such non-equilibrium structuring. At

higher frequencies of the rotating field, drop-like aggregates rotate asynchronously with the field. Thanks to hydrodynamic interactions with the suspending liquid, their shapes evolve into a bent rod, starfish, or oblate ellipsoid depending on the field amplitude and frequency [Bacri et al. (1994); Cēbers (2002); Lebedev et al. (2003)], but in any case, the collapse of all the aggregates into a single bulk phase has never been reported.

Whatever their morphology, when spinning under a rotating magnetic field, the magnetic assemblies (micro-aggregates or ferrofluid droplets) generate local flows around them that extend into the solvent at a length-scale comparable to their size. The question is whether they can generate a macroscopic flow propelling the whole magnetic colloid within the channel where this colloid is confined. The response is provided in the following Section 1.2.3.

1.2.3 Field-induced flow actuation and mass transport in magnetic colloids

It is true that, under certain conditions, magnetic particles can induce a macroscopic flow of the whole colloidal suspension. The two most documented examples are: (a) macroscopic spinning motion of a magnetic nanoparticle colloid (ferrofluid) in a cylindrical vessel induced by a rotating magnetic field [see Rosensweig (1985) and the references therein], and (b) strong vortex flows induced in a suspension of magnetic microparticles by triaxial alternating magnetic fields [Martin and Solis (2015)].

These two cases correspond to the two opposite particle size limits and emerge different mechanisms of the flow actuation. Small monodomain nanoparticles of a ferrofluid collectively spin under a rotating magnetic field, and the whole ferrofluid corotates with the applied field, except for a surface layer that anti-corotates [Chaves et al. (2006)]. This effect is qualitatively captured by a theoretical model involving magnetisation relaxation and diffusion of the internal angular momentum [Zaitsev and Shliomis (1972); Shliomis (2021)]. Quantitatively, the ferrofluid angular speed is about two orders of magnitude lower than the magnetic field angular frequency, and the effect is usually observable in very concentrated ferrofluids. This is likely the reason why such an effect remains unexplored in nanotechnology. On the contrary, vortex flows induced by magnetic micron-sized particles have promising applications in microfluidic mixing, bioassays, or heat transfer [Martin and Snezhko (2013)]. The microparticle self-assembly and flow patterns are tuned by magnetic dipolar interactions forming the particle chains that undergo complex dynamics under triaxial alternating fields, including spinning, bending, fragmentation and coalescence [Martin and Solis (2015)]. However, our target application (blood clot lysis in blocked vessels) requires using magnetic nanoparticles at low

concentrations instead of microparticles to generate the flow. The challenge is to find appropriate physical and physicochemical conditions at which magnetic nanoparticles can self-assemble under rotating magnetic fields because their magnetic assemblies can generate macroscopic flows.

Several preliminary theoretical studies[2] predict reciprocal oscillatory flows along slit-like cylindrical channels in running non-homogeneous magnetic fields [Musickhin et al. (2021); Zubarev et al. (2020); Zubarev et al. (2021); Chirikov et al. (2022)]. However, steady-state recirculation flows vital for the target application likely do not arise in those configurations.

Field-induced mass transport can be described as the trapping, separation, and mixing of non-magnetic solutes (cells, proteins or colloids) dispersed in a ferrofluid via magnetic forces. In most cases, a substantial enhancement of the mixing of non-magnetic solutes under applied magnetic fields is reported. This is extremely important for our target clot lysis application, in which we seek acceleration of the thrombolytic drug delivery by applying magnetic fields. In general, the mass transport of non-magnetic solutes depends on the geometry of the system and the magnetic field configuration. For instance, a unidirectional oscillating magnetic field allows efficient mixing of a ferrofluid (and dissolved solutes) in a small rectangular channel [Mao and Koser, (2007)]; a permanent gradient magnetic field allows efficient transverse mixing of a ferrofluid core stream with two water sheath streams in a flow-focusing device due to magneto-convective instabilities on ferrofluid/water interface [Hejazian et al. (2016)]; a magnetic field rotating in the plane of the cross-section of a cylindrical channel allows an enhanced radial transport of non-magnetic solutes [Boroun and Larachi (2020)]. All the aforementioned configurations are believed to be promising for microscale mixing in biomedical devices, such as on-chip immunoassays.

1.3 Unresolved issues and thesis objectives

Analysis of the literature survey presented in Sec. 1.1.3 and 1.2 reveals several open questions, both practical and fundamental, but anyway being of extreme relevance for the target biomedical application of IONPs in the blood clot lysis. These questions and associated physical phenomena can be summarised as follows:

(a) Once the IONP is delivered in the vicinity of the blood clot, how efficient and how fast will their self-assembly be under rotating magnetic fields? How will the self-assembly

[2] Collaboration between the hosting team at University Côte d'Azur and the University of Ekaterinburg (Russian Federation) and in which the PhD fellow was involved

timescale be compared to the duration of a typical surgical intervention? These questions impose a detailed study of the kinetics of field-induced phase separation of a magnetic colloid that will be reported in Chapter 3 by using aqueous solutions of 10 nm-sized citrate-coated IONPs placed into a thin microfluidic channel.

(b) Once the magnetic self-assemblies (presumably elongated micron-sized aggregates) are formed, will they be able to rotate continuously and generate recirculation flows in the blocked blood vessels? To answer (at least conceptually) this question, we will try, in Chapter 4, to find a magnetic field configuration that allows an easy generation of recirculation flows in a closed microfluidic channel mimicking a blocked blood vessel. The experimental velocity profiles of the generated flow within the colloid of citrate coated IONP will be analysed through particle image velocimetry (PIV).

(c) Once the recirculation in a blocked vessel is established, will it be sufficiently intense to rapidly deliver the thrombolytic drug towards the clot and dissolve it much faster than the lysis rate provided by diffusion-limited drug transport without recirculation? At this point, in a short time-lapse available for this task, we could not handle the physicochemical compatibility of actual fibrine clots with our citrate coated IONPs. However, we will try a proof of the concept in Chapter 5 using calcium alginate microbeads placed at the extremity of a microfluidic channel. We aim to observe to what extent the magnetically actuated recirculation flow will enhance the convective transport of the dissolution agent – trisodium citrate – and accelerate the calcium alginate dissolution.

Resuming the above points, the **global objective of the thesis work** is to develop a microfluidic *in vitro* model mimicking magnetically actuated blood clot dissolution and allowing rigorous experimental monitoring of several physical phenomena taking place along the process.

The obtained experimental correlations will, whenever possible, be completed by theoretical modelling to ensure a deeper insight into the topic and bring a necessary physical background for the future development of the target application.

We will proceed in Chapter 2 to a detailed description of the used magnetic colloid and experimental setups and protocols used to achieve the above-formulated goals.

Chapter 2. Materials and Methods

This chapter will first describe the synthesis and characterisation of the magnetic iron oxide colloid used throughout the manuscript [Sec. 2.1]. Then, in Sec. 2.2, we will describe the fabrication and characterisation of calcium alginate microbeads used in Chapter 5 as a model medium for experimental simulation of blood clot dissolution. After that, in Sec. 2.3, we will present an experimental setup used (after appropriate adaptations) in all experimental studies of the present manuscript. Finally, the experimental protocols and image processing procedures are provided in Sec. 2.4 and 2.5, respectively.

2.1 Magnetic colloid

2.1.1 Synthesis and working solution preparation

The magnetic colloid (ferrofluid) composed of maghemite nanoparticles dispersed in a dilute aqueous solution of trisodium citrate has been graciously provided by Dr A. Bee and Dr D. Talbot from the PHENIX laboratory in Paris. Briefly, the maghemite IONPs were synthesised using the co-precipitation of iron salts in an alkaline medium [Massart (1981)] followed by oxidation of obtained magnetite to maghemite using iron nitrate reagent [Talbot et al. (2021)], Nanoparticles were stabilised against irreversible aggregation by adsorption of trisodium citrate allowing electrosteric repulsion between nanoparticles at neutral pH and at initial relatively low ionic strength (~0.05M) [Dubois et al. (1999); Roger et al. (2006)]. The parent ferrofluid was stable against colloidal aggregation for a few years.

For all experiments in the present manuscript, the parent ferrofluid was diluted in Milli-Q water with the addition of 0.35 mol/L of sodium chloride (NaCl) salt and an appropriate amount of hydrochloric acid (HCl) to reach the pH≈5.5 and the nanoparticle volume fraction $\varphi_0 = 1.6 \times 10^{-3}$ (0.16 vol.%). The mixture was stirred for 1h using an orbital shaker. The salt addition decreased the characteristic thickness of the electric double layer (Debye screening length) on the nanoparticle surface. In contrast, adding the acid decreased the surface electric charge thanks to partial deprotonation of the carboxylate groups of adsorbed citrate ions. This protocol allowed partial screening of electrostatic interactions between nanoparticles, promoting slight colloidal agglomeration necessary to induce reversible phase separation in the presence of magnetic fields.

In experiments with the visualisation of recirculation flows (Chapter 4), flow tracers were added to the magnetic colloid. Concretely, 10 µL of an aqueous solution of polystyrene beads (Polybead® microspheres from PolyScience, USA; diameter 5µm, weight concentration 2.7%)

were added to 5 mL of the magnetic colloid with φ_p =0.16% vol. It was checked that this addition did not influence the colloidal stability of magnetic nanoparticles. The resulting colloid-tracer mixture showed similar behaviours under a magnetic field compared to the colloid without tracers.

In the experiments for the dissolution of alginate beads, we used the same dilute magnetic colloid without tracers. We supplemented a trisodium citrate aqueous solution for faster calcium alginate bead dissolution. It was compared to the slow dissolution rates observed in the original dilute magnetic colloid with an initial trisodium citrate concentration of about 8 mmol/L, as quantified through potentiometric titration [Talbot et al. (2021)]. The magnetic colloid was prepared by vigorous mixing (1 min on a vortex mixer at a rotation speed of 1600 rpm) of different ingredients respecting the IONP volume fraction φ_p =0.16% vol, as in previous experiments and the final trisodium citrate concentration equal to 158 mmol/L, found empirically to ensure the alginate bead dissolution time compatible with reasonable duration (about 5-10 min) of the magnetic field application avoiding overheating of the coils. In punctual experiments, we used the dilute magnetic colloid (at φ_p =0.16% vol, pH=5.5) of uncoated magnetic nanoparticles without dissolved sodium citrate to check the dissolvability of the beads by the sole mechanical action of recirculation flow without a dissolving agent.

We warrant the reader that citrate-stabilised magnetic colloid is far from the one that can be used for the blood clot lysis application. However, for the final application, the nanoparticles will be designed in such a way that, once injected into the blood, they will form some small primary agglomerates (likely through blood protein adsorption binding neighbouring particles), which will facilitate their self-assembly into larger elongated aggregates in the presence of the applied magnetic field[3]. A slight colloidal destabilisation of citrate coated IONPs in the present manuscript allows enhanced self-assembly under an applied magnetic field[4] . It is believed to somehow mimic the future colloid's physical behaviour under applied rotating magnetic fields.

[3] A PhD thesis on the development of such a biocompatible colloid is starting at the hosting team at UCA

[4] The concept of the field-induced phase separation enhanced through colloidal attractive interparticle forces is being extensively developed in frames of the Axlepios Biomedical R&D project with another PhD thesis in progress [Queiros Campos et al. (2021a); Queiros Campos et al. (2021b)]

2.1.2 Characterisation

The hydrodynamic size distribution and electrophoretic mobility (or zeta-potential) of nanoparticles in the diluted colloid were determined by dynamic light scattering (DLS) and laser Doppler velocimetry using Zeta Sizer Nano ZS (Malvern Instruments, UK). The obtained intensity size distribution (i.e. the fraction of the intensity of the light scattered by particles of a given size range as a function of the particle size) is shown in Fig. 2.1 for different times t elapsed since the dilution of the colloid, with $t = 1$ h corresponding to the moment immediately after the orbital shaking. For the sake of comparison, we add a size distribution curve measured on the dilute colloid ($\varphi_0 = 1.6 \times 10^{-3}$) without salt/acid addition (pH≈7.6) – see dashed black curve in Fig.2.1. This curve presents a single peak at $d_H \approx 21$ nm that does not evolve with time showing perfect colloidal stability. The size distribution with salt/acid addition at $t = 1$ h is within the measurement error equivalent to the size distribution without salt/acid addition. However, at $t = 2, 3, 4$ h, a secondary peak at $d_H \approx 120 - 140$ nm appears, and its height increases with time. During the height of the primary peak at $d_H \approx 20$ nm decreases, pointing to progressive agglomeration of nanoparticles caused by the partial screening of electrostatic repulsion.

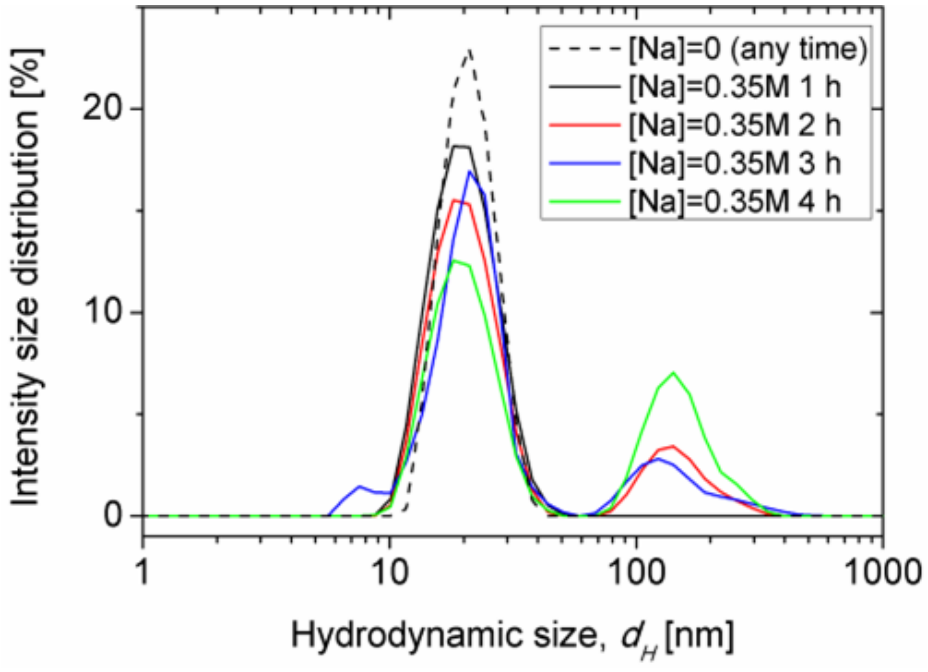

Figure 2.1: The intensity distribution of hydrodynamic nanoparticle size measured by DLS

The electrophoretic mobility measurements are summarised in Table 2.1 and show that (a) in all the cases, the zeta potential remains negative, pointing out to negative surface charge coming from carboxylate surface groups; (b) it is lower in absolute value for the colloid with

salt/acid addition ($\sim -20\,mV$) than without addition ($\sim -50\,mV$) because of lower protonation degree of carboxylate groups at lower pH; (c) it shows some increase (in absolute value) with the time likely because of long protonation equilibrium processes.

To check possible electrostatic screening, the Debye screening length, κ^{-1}, is evaluated under the assumption of symmetric 1-1 electrolyte with the total molar concentration of sodium ions equal to the sum of the concentration of added NaCl salt and initial concentration of sodium counterions measured by Inductive Coupled Plasma – Optical Emission Spectrometry (ICP-OES): $[Na]_{tot}=[NaCl]+[Na]_{in}$ =0.350 +0.025=0.375 (mol/L). Using the well-known expression for κ^{-1} [see, for instance, Van De Ven (1989)], we get $\kappa^{-1} \approx 0.5 \pm 0.1$ nm with salt addition and $\kappa^{-1} \approx 2.0 \pm 0.1$ without salt/acid addition. We see a four-fold decrease of the Debye screening length with the salt addition, which decreases colloidal stability against van der Waals dispersion forces. However, steric repulsion due to adsorbed citrate layers avoids fast irreversible aggregation. The samples prepared with salt/acid addition do not precipitate for at least a few months despite some agglomeration of nanoparticles revealed by DLS [Fig. 2.1]. The results of the above physicochemical characterisations are summarised in Table 2.1 for different elapsed times.

Table 2.1: Physico-chemical characterizations of samples without ([Na]=0) and with ([Na]=0.35M) salt/acid addition

Sample	Elapsed time, h	pH	Zeta potential (mV)	Debye length (nm)
[Na]=0	0 – 1 year	7.60±0.05	-49.5±3.0	2.0±0.1
[Na]=0.35M	1	5.50±0.05	-18.8±2.2	0.5±0.1
	2	5.50±0.05	-23.4±1.0	0.5±0.1
	3	5.55±0.05	-25.3±1.7	0.5±0.1
	4	5.55±0.05	-29.6±1.7	0.5±0.1

Magnetisation measurements have been performed on the parent ferrofluid at room temperature using a Vibrating Sample Magnetometry (VSM 4500 from EG&G Princeton Applied Research, USA). These measurements allowed finding the magnetisation saturation $M_S \approx 310 \pm 10\ k\mathrm{A/m}$ of nanoparticles relevant for maghemite composition with spin canting effects and the size distribution of their iron oxide cores fitted to log-normal distribution:

$$f_m(d_m) = \frac{1}{\sqrt{2\pi}\sigma_m d_m} \exp\left(- \frac{\left(\ln\left(\frac{d_m}{\langle d_m \rangle}\right) + \frac{\sigma_m^2}{2} \right)^2}{2\sigma_m^2} \right), \quad (2.1)$$

with the relative distribution width $\sigma_m = 0.36$, and the average diameter of the iron oxide cores (referred to as "magnetic" diameter) $\langle d_m \rangle = 8.1$ nm. The "magnetic" nanoparticle size $\langle d_m \rangle = 8.1$ nm is about 2.5 times less than the hydrodynamic size $d_H \approx 21$ nm (at the primary peak) likely because of slight agglomeration even in the absence of salt/acid addition.

In Chapter 3, we will need the 3rd, the 6th and the 9th moments of the nanoparticle size distribution. In general, the j^{th} moment is given by

$$\langle d_m^j \rangle = \langle d_m \rangle^j \exp\left(\frac{1}{2}(j-1)j\sigma_m^2\right), \quad (2.2)$$

which gives $\langle d_m^3 \rangle = (9.2 \text{ nm})^3, \langle d_m^6 \rangle = (11.2 \text{ nm})^6, \langle d_m^9 \rangle = (13.6 \text{ nm})^9$.

2.2 Alginate beads

In experiments with polymeric beads dissolution (Sec. 2.4.3, Chapter 5), we need to fabricate calcium alginate microbeads of a diameter approximately equal to 1 mm to fit them in the width of a microfluidic channel (whose fabrication is detailed in Sec. 2.3.2). For this purpose; we prepare an aqueous solution of sodium alginate of molecular weight 120 000-160 000 g/mol at a weight fraction of 1% wt. This solution is then placed into a plastic syringe and is expulsed through a needle of a diameter of 0.26 mm into a beaker filled with a 0.5 mol/L calcium chloride solution using a syringe pump (PHD Ultra Harvard Apparatus, USA) at a constant volume flow rate of 45 $\mu L.s^{-1}$as schematically shown in Fig. 2.2. This flow rate has been found empirically to create drops of a sodium alginate solution of the desired diameter. Falling drops react with the calcium chloride bath by displacing sodium ions with calcium ones. This creates electrostatic links between carboxylate groups of neighbouring alginate chains and provokes a physical cross-linking of the alginate chains, the final product referred to as calcium alginate. Simply speaking, drops of a liquid sodium alginate solution "solidify" during their free fall in the calcium chloride bath and form the beads of calcium alginate hydrogel.

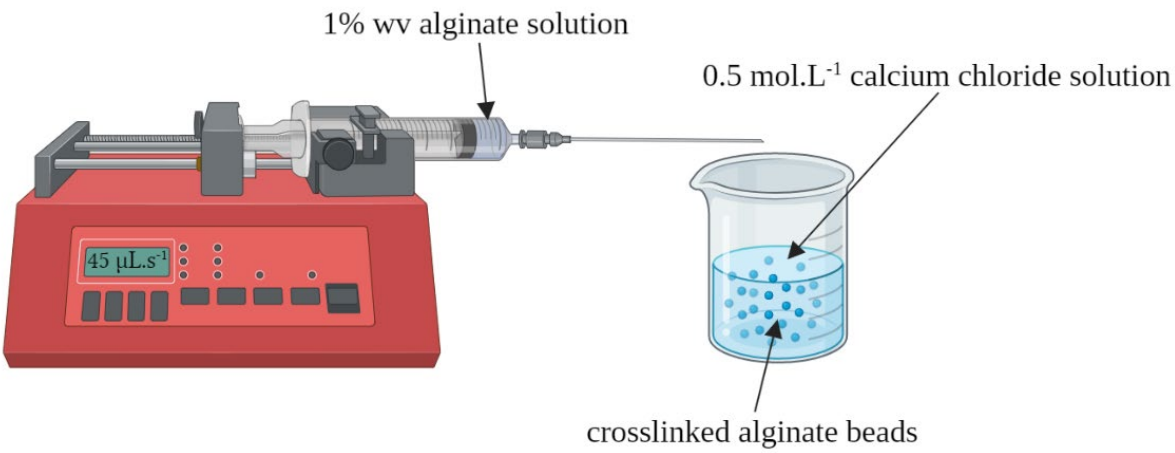

Figure 2.2: Automated setup for the preparation of alginate beads using a syringe pump

Injection of 10 mL of the sodium alginate solution allows the formation of numerous microbeads left in the calcium chloride bath for 24 h at 8°C and then sieved to select the beads in the size interval 850 – 900 mm. These beads are then stored in MilliQ water solution at 8°C before their use in bead dissolution experiments.

2.3 Experimental setup

In all experiments reported in Chapters 3, 4 and 5, we used the same experimental setup, shown in Fig. 2.3, which, whenever relevant, was re-adapted for each new experiment. The setup consists of the following main elements: (a) two pairs of Helmholtz coils allowing the generation of rotating magnetic fields; (b) a microfluidic channel filled with a magnetic colloid and placed on Plexiglass support in the middle between the coils, and (c) InfiniTube™ Standard Video/Machine Vision Microscope (Infinity, USA) equipped with Infinity IF-4 objective and attached to a complementary metal oxide semiconductor (CMOS) detector camera PL-B742U (PixelLink, Ottawa, ON, Canada); the microscope tube with a camera were placed above the microfluidic channel (d) LED illuminator equipped with a rheostat placed below the microfluidic channel. The elements (a) and (b) will be described in more detail in Sec. 2.3.1 and 2.3.2, while the experimental protocols will be described in Sec. 2.4.

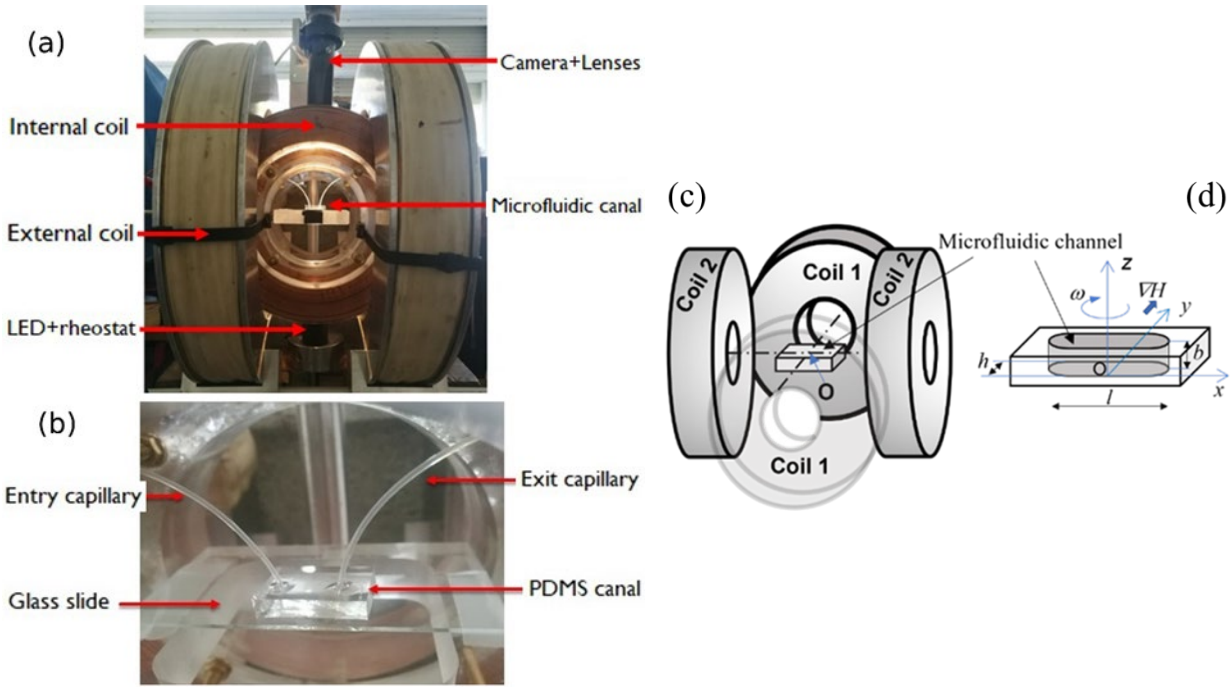

Figure 2.3: Experimental setup presented in a photographic view (a) and sketched view (c). A magnified view showing a microfluidic channel placed in the centre of two pairs of coils is shown in (b). A sketch of the microfluidic channel is shown in (d).

2.3.1 Electromagnetic circuit

The electromagnetic circuit consisted of two pairs of Helmholtz coils, as shown in Fig. 2.3 (a) and (c). The two external coils of the 1st pair are perpendicular to two internal coils of the 2nd pair.

In experiments with the kinetics of field-induced separation (Chapter 3), we generated a homogeneous (at the scale of a few cm in the central region between coils) rotating magnetic field using all the four coils shown in Fig. 2.3 (a) and (c). For this purpose, the AC sinusoidal voltage of the desired frequency in the range $\nu = 5 - 25$ Hz is generated by two audio channels of the motherboard of a personal computer controlled by a homemade MATLAB code. Both signals are amplified with the help of the Macro-Tech 5002VZ sound amplifier (Crown Audio, USA) and are then injected into two coil pairs. The amplitude, amplification and phase lag of both voltage signals are carefully adjusted to get magnetic fields generated by each pair of coils having the same amplitude $H_0 = 9$ kA/m and the phase lag of $\pi/2$. As mentioned above, this allows the generation of a homogeneous (on the length scale of the microfluidic channel) circularly polarised rotating magnetic field of an amplitude H_0 and an angular frequency $\omega = 2\pi\nu$.

In experiments with recirculation flows (Chapter 4) and polymer bead dissolution (Chapter 5), we disconnected the front coil 1 and used only three coils, as shown for clarity in Fig.2.4.

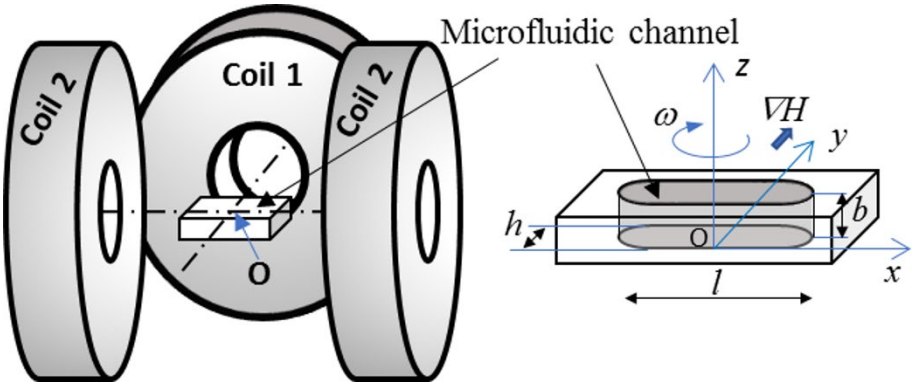

Figure 2.4: Geometry of the experimental system for generating macroscopic recirculation flows. On the right, an enlarged view of the microfluidic channel with the definition of several physical parameters is shown.

The three-coil system allowed us to generate in the xy plain a circularly polarised rotating but the heterogeneous magnetic field in the vicinity of the centre *O*. This was possible by applying sinusoidal alternating electric current (AC) to each coil with a $\pi/2$ phase lag between the coil 1 and a pair of coils 2 at an appropriately chosen amplitudes. The resulting magnetic field distribution $\boldsymbol{H}_1$ and $\boldsymbol{H}_2$ of coil 1 and the pair of coils 2 reads:

$$\begin{cases} H_{1x} = H_{0x}(x,y)\, cos(\,\omega t);\; H_{1y} = H_{0y}(x,y)\, cos(\,\omega t) \\ H_{2x} = H_0\, sin(\,\omega t);\; H_{2y} = 0 \end{cases} \tag{2.3}$$

where t is the time, ω is the angular frequency of the generated field, $H_{0x}(x,y)$, $H_{0y}(x,y)$ are respectively the x and y components of the space-dependent amplitude of the field generated by coil 1 and H_0 is the amplitude of a homogeneous (within a few centimetres central region) magnetic fields generated by the coils 2. A circular field polarisation is achieved in a few millimetres central region (covering the whole microfluidic channel) if the amplitude of the field produced by the 1st coil respects the following condition: $H_{0x}(0,0) = 0; H_{0y}(0,0) = H_0$. On the other hand, the generated magnetic field is heterogeneous and, as will be shown in Chapter 4, exerts to our paramagnetic aggregates a magnetic force proportional to the gradient of the field squared $\nabla(H^2)$. An analysis based on Maxwell magnetostatic equations shows that, in the central region, the gradient $\nabla(H^2)$, and consequently, the magnetic force has the dominant component oriented along the y axis. In contrast, the x and z components are negligible at all points of the microfluidic channel, thanks to the fact that the channel dimensions are at least two orders of magnitude smaller than the dimensions of coils and spacing between them. The

expressions for the instantaneous value of $\nabla(H^2)$ and the value of the field gradient averaged throughout the field rotation reads:

$$\nabla(H^2)_{x=y\approx 0} = \left(\frac{\partial {H_{0y}}^2}{\partial y}\right)_{x=y=0} \cos^2(\omega t)\, \boldsymbol{e}_y, \tag{2.4a}$$

$$\langle \nabla(H^2)_{x=y\approx 0} \rangle = \frac{1}{2}\left(\frac{\partial {H_{0y}}^2}{\partial y}\right)_{x=y=0} \boldsymbol{e}_y, \tag{2.4b}$$

where $\boldsymbol{e}_y$ is the unit vector along the y-axis. Quantitatively, the generated magnetic field had an average amplitude $H_0 = 6.4$ kA/m, frequency 5 Hz corresponding to the angular frequency $\omega = 2\pi \times 5$ Hz ≈ 31.4 rad/s and the time-averaged gradient $\left|\nabla(H^2)_{x=y\approx 0}\right| = 7.5\text{x}10^8$ A^2/m^3.

2.3.2 Microfluidic channel

The microfluidic channel used in experiments with the kinetics of phase separation (Chapter 3) and recirculation flows (Chapter 4) was fabricated by glueing a poly dimethyl siloxane (PDMS) lid having a rectangular cavity to a microscope glass slide. The photographic and sketch views of the channel are shown in figures 2.3b, d and Fig. 2.4. At the same time, the main fabrication steps are summarised in Fig. 2.5. The PDMS lid was fabricated by soft photolithography as described in detail in Ezzaier et al. (2018). The channel dimensions along x, y and z directions (introduced in Fig. 2.4) are denoted by l, h and b, respectively. The dimensions of the channels used in different experiments (Chapters 3-5) were slightly different, summarised in Table 2.2. Flexible tubes of an internal/external diameter equal to 0.5/1 mm were introduced to both extremities of the channels to form the inlet and the outlet necessary for the filling with a magnetic colloid and washing with deionised water

.

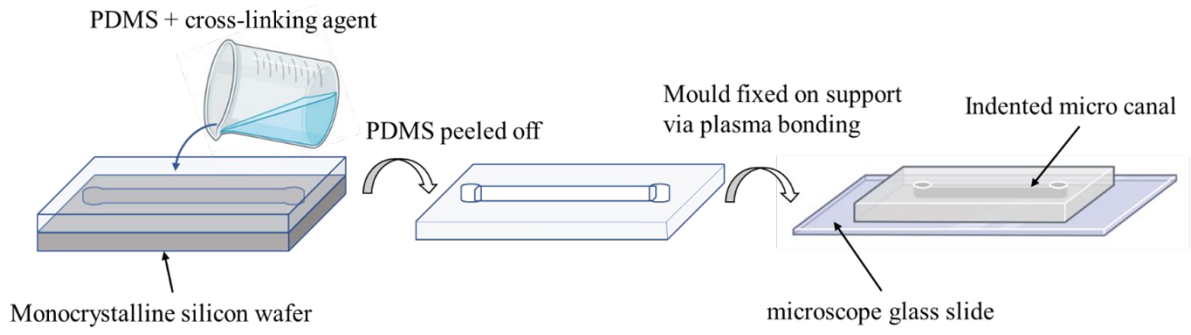

Figure 2.5: Microfluidic canal creation process

A microfluidic channel used in experiments with the polymer bead dissolution (Chapter 5) was very similar to the one previously described [Figs. 2.3b and d], except for the three following points: (a) a thin PDMS flat substrate (fabricated by spin coating and deposited on the top of a glass slide) was used; (b) the PDMS lid (having rectangular cavity) was not glued to the substrate but clipped to it; (c) the connecting tubing was not introduced to the channel extremities. Instead of glueing, clipping allowed the channel to be correctly filled with a magnetic colloid that encountered the alginate bead (cf. Sec. 2.4).

Table 2.2: Dimensions of the microfluidic channels used in different experiments.

Experiment	Length l (μm)	Width h (μm)	Depth b (μm)
Chapter 3	10000±50	2000±20	200±5 or 50±5
Chapter 4	2000±20	550±10	232±5
Chapter 5	10000±200	1000±20	300±5

2.4 Experimental protocols

In this Section, we describe the experimental protocols separately for each experiment reported in the subsequent Chapters 3, 4 and 5.

2.4.1 Kinetics of field-induced phase separation

All experiments were done with diluted colloid treated by salt/acid addition, having the particle volume fraction $\varphi_0 = 1.6 \times 10^{-3}$, as specified in Sec. 2.1.1. After filling, the microfluidic channel was placed in the middle between two coil pairs and the rotating magnetic field of the desired frequency was applied in the horizontal plane. The magnetic field application rapidly initiated the phase separation process and manifested through the appearance of needle-like nanoparticle aggregates synchronously rotating with the magnetic field. The process was visualised with the help of the infinity optical system and recorded by a CMOS camera (cf. beginning of Sec. 2.3, Fig. 2.3a). The snapshots of the phase separating colloid were recorded each 0.25 s – a time interval small enough to follow the kinetics of aggregation after the swift initial nucleation stage. Videos at a frame rate (in fps) equal to one-fourth of the given excitation frequency ν were also taken in some cases.

The stack of the snapshots was analysed by specially developed MATLAB code, allowing determining the length and width distribution of the aggregates at each moment along with the

integral characteristics, such as the number of aggregates per observation window, allowing evaluation of the number of aggregates n per unit suspension volume, their average length $\langle L \rangle$, width $\langle d \rangle$, aspect ratio $\langle r \rangle = \langle L/d \rangle$, or volume $\langle V \rangle$, while the fraction of the suspension volume occupied by the aggregates was evaluated as $\Phi = n\langle V \rangle$. The image treatment procedure is detailed in Sec. 2.5.1.

In addition to it, the amplitude of the threshold magnetic field H_0 and the threshold nanoparticle volume fraction φ' below which the field-induced agglomeration does not take place was measured by filling the microfluidic channel with the diluted colloid (treated with salt/acid addition) at different volume fractions φ, applying increasing values of the magnetic field intensity over 20 min and observing whether the needle-like aggregates of a minimal length about 1μm appear or not. The experimental dependencies $H_0(\varphi')$ were then analysed for different field frequencies allowing determining the initial supersaturation Δ_0 – the crucial parameter intervening in the theoretical model developed in Chapter 3.

Since colloidal agglomeration (due to partial screening of electrostatic interactions between nanoparticles) could interfere with the field-induced aggregation, the sample history and duration of experiments are important issues for the present system. Each time, the experiments started one hour after the end of the orbital shaking of the sample. One experimental run lasted for 20 min, after which the channel was washed and filled with a fresh sample, but the whole experimental series lasted no longer than one hour. Thus, the experiments fitted to the interval $2\ \text{h} \leq t \leq 3\ \text{h}$ of the time elapsed from the moment of the dilution of the parent ferrofluid (including the orbital shaking stage lasting for 1h). According to DLS measurements [Fig. 2.1], the secondary size distribution peak promotes efficient field-induced aggregation, but it does not evolve significantly during this time interval. We expect, therefore, that the timescale of colloidal agglomeration (~ a few h) is much longer than the timescale of the field-induced aggregation (~ a few min). This allows us to safely neglect the change of the suspension dispersion state during field-induced phase separation.

2.4.2 Field-induced recirculation flow

In these experiments, we used a mixture of dilute magnetic colloid at IONP volume fraction $\varphi_0 = 1.6 \times 10^{-3}$ mixed with polystyrene microbeads used as flow tracers, as described in Sec. 2.1.1. Once the colloid-tracer mixture was injected into the microfluidic channel, the flexible tubes were removed, and the channel extremities were closed with glass caps. The channel was then placed onto rigid support in the centre O of a three-coils system with the channel's longitudinal axis aligned with the axis of symmetry of a pair of coils 2, as shown in Fig. 2.4.

Once the rotating non-uniform magnetic field with a gradient along the y-axis [Fig. 2.4, cf. Eq. 2.2 and Sec. 2.3.1] was on; the generated recirculation flows were visualised from the top by the infinity optical system and recorded by a CMOS camera (cf. beginning of Sec. 2.3, Fig. 2.3a). The snapshots were recorded at a frame rate of 6.67 s^{-1} for 300 s elapsed from the moment of the field application. The experiments were conducted six times to check the reproducibility.

The obtained image stack was processed using the PIVlab tool [Thielicke and Sonntag (2021)] run on the MATLAB software and customised for our problematics (pre-processing and analysis). In general, this tool uses the principles of particle image velocimetry (PIV) to analyse the velocity profiles in the observed fluid. Standard PIV experiments are usually realised in obscure conditions with local illumination by a laser sheet, which excites fluorescent or diffractive tracers. The change of tracer positions in the flowing fluid is analysed by finding the spatial correlation between different parts of two consequent frames, allowing one to find the displacement field and, afterwards, the fluid's velocity field [Raffel et al. (2018)]. In our case, we conducted experiments under global illumination from both daylight, and a LED source placed about 10 cm below the channel. As tracers, we used non-fluorescent polystyrene beads that were small enough and had a relatively poor optical contrast to be distinctly seen through our microscope but still enough to create some "texture" in the images. Displacement and deformation of this texture were analysed by the PIVlab tool in the same way as the motion of an ensemble of fluorescent tracers. A few calibration experiments allowed us to validate the correctness of the velocity determination using these tracers. The velocity field determination and the averaging procedure are detailed in Sec. 2.5.2. The PIV analysis mentioned above does not allow distinguishing the aggregate motion from the suspending fluid motion. Thus, another image processing procedure was developed based on the Fiji image calculator to track the motion of aggregates as well as to determine their size and concentration distributions, as described in detail in Sec. 2.5.3.

2.4.3 Field-enhanced polymer bead dissolution

In these experiments, we used the following items: (a) dilute magnetic colloid at IONP volume fraction $\varphi_0 = 1.6 \times 10^{-3}$ with added trisodium citrate at 158 mmol/L, as described in Sec. 2.1.1; (b) calcium alginate microbeads of diameter close to 1000 μm, as described in Sec. 2.2, and (c) clipped microfluidic channel described in Sec. 2.3.2. We opened the channel and placed a calcium alginate bead inside around the centre of its rectangular cavity. The cavity was then gently filled with a magnetic colloid by a syringe and closed (or clipped) by manually pressing the PDMS substrate to the PDMS lid. As already stated in Sec. 2.2, the alginate beads had a diameter approximately equal to the channel width h=1000 μm but are about 3-times larger than the channel depth b=300 μm [cf. Table 2.2]. Thus, the bead was squeezed in the z channel direction during channel clipping and dilatated in the x direction. Being filled with an aqueous ionic medium at 98% wt water concentration, we believe that the total volume of the bead was conserved after the squeezing and, what is more important, the squeezed bead separated the channel into two compartments with no easy filtration from the left to the right compartment and vice versa (Fig 2.6). Furthermore, this simple filling-up procedure ensured that the magnetic colloid was brought to contact with the alginate bead without bubbles at the bead/liquid interface. Also, since no external pressure gradients are applied to the channel, a simple clipping ensures proper sealing.

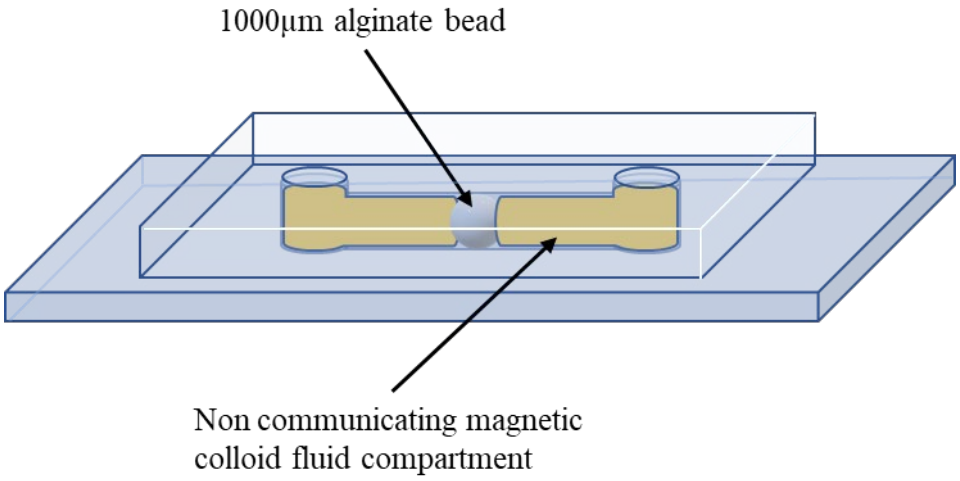

Figure 2.6: Schematic of the alginate bead positioning inside the microfluidic channel.

After filling and closing, the channel was introduced into the centre of the three-coil system [Fig. 2.4], the non-uniform rotating magnetic field of an amplitude of 6.4 kA/m and frequency of 5 Hz with a gradient along the y-axis [Fig. 2.4, cf. Eq. (2.2) and Sec. 2.3.1] was generated. The value of the gradient is the same as in experiments with the flow recirculation:

$\left|\nabla(H^2)_{x=y\approx 0}\right| = 7.5\text{x}10^8$ A^2/m^3 [Sec. 2.4.2]. This generated the recirculation flow of the magnetic colloid and, consequently, the convective mass transport of the trisodium citrate towards the alginate bead. The process of the bead dissolution was visualised by the infinity optical system and recorded by the CMOS camera [cf. Fig. 2.3b, beginning of Sec. 2.3] at the rate of 1 image/s and at an exposure time of 5 ms to get a net image of rotating aggregates. Collected snapshots were then processed by Image J software allowing calculation of the change of the microbead area with time (a signature of the bead dissolution in the case of applied magnetic field) or its dilatation (in the absence of field), as detailed in Sec. 2.5.4.

2.5 Image processing

In this Section, we detail all image processing procedures used to quantify the recorded observations of different experiments, reported in Chapters 3, 4 and 5.

2.5.1 induced phase separation

The snapshots collected after recording the field-induced aggregation process were processed as follows. The first step was to get image stacks after correcting the illumination. The shading image was estimated as the temporal maximum of the time-lapse stack. Then, to correct illumination jittering, we extract a normalised absorbance stack $A(x, y, t) = [B - I(x, y, t)]/B$, where $I(x, y, t)$ is the image intensity after correcting the inhomogeneity due to dust particles and illumination, and B is the most frequent illumination intensity. We then apply thresholding, morphological closing and removing small objects sequentially to get individual aggregates. For each aggregate, we get its absorbance, length, and width for a given moment. The histogram of the aggregate length distribution is finally constructed using a built-in MATLAB function. Notice that the arrangement of all aggregates in the single horizontal plane significantly simplified the image processing. To check the correctness of the data processing by the MATLAB code, some results were checked with the Fiji software by "manual" measurements over a series of aggregates for each analysed snapshot. All experiments were repeated 4 times, the integral aggregation characteristics were averaged over 5 measurements, and the standard deviation was evaluated for each moment.

2.5.2 Determination of the velocity field of recirculation flow through the PIVlab tool

The determination of the velocity field (briefly described in Sec. 2.4.2) was split into the following steps:

1. We determined that the time at which the aggregate size distribution reached its plateau and the generated flow reached the steady state occurred at the time $t \approx 100$ s elapsed from the moment of the magnetic field application. Thus, the first images corresponding to $t < 100$ s were excluded from the analyses because we seek for the steady state velocity profiles. The rest of the images were submitted to the following three steps:

2. Pre-processing. The images were loaded into a pre-processing MATLAB script, which pivoted them to align the image of the channel front wall (lower wall in the snapshots) along a horizontal line and subtract the mean of the stack over time (removing inhomogeneity due to the sample and the microscope illumination). To facilitate visualisation, the image grayscale is inverted. The purpose was to contrast the aggregates and the polystyrene tracers that appeared white on a completely black background. [Fig. 2.7]. Since the frame rate was 4/3 times the frequency of the aggregate rotation, the aggregates appeared with two orthogonal orientations periodically changing between two frames. It was necessary to separate each pair and impair snapshot into two different stacks within which the aggregates kept the same orientation. Thus, we obtained two stacks of monochromatic images with orthogonal aggregate orientations. Such a separation allowed us to check the possible influence of the aggregate orientation on the overall velocity profile.

3. PIV processing. Each sub-stack was loaded into the PIVlab script. The region of interest (ROI) focused on the observed channel was drawn. Then the PIV analysis was parametrised as follows: Fast Fourier Transform (FFT) window deformation algorithm; 64 pixels interrogation area for the first iteration (pass) and 32-pixel areas for the second pass; Gauss 2x3-point interpolation for subpixel x and y positions of the correlation function peak. Once the images were analysed, x and y velocity components were thresholded by the algorithm allowing one to exclude the outliers. Thus, the velocity components were bounded from above by the values $v_x = \pm 10$ px/frame and $v_y = \pm 5$ px/frame.

4. Post-processing. The data obtained from the PIVlab script were imported to another script, which first converted the velocities v_x, v_y and positions x, y into physical units (μm/s and μm, respectively). Then, we focused on the longitudinal velocity profile $v_x(x, y, t)$ and proceeded to the averaging over the observation time T: $\langle v_x(x, y)\rangle_T = T^{-1}\int_0^T v_x(x, y, t)dt$,

over the ROI length l: $\langle v_x(y,t)\rangle_l = l^{-1}\int_0^l v_x(x,y,t)dx$ or over both these magnitudes: $\langle v_x(y)\rangle_{l,T} = (Tl)^{-1}\int_0^T\int_0^l v_x(x,y,t)dx\,dt$. The integration was performed using discrete calculus separately for each of the two stacks (with two orthogonal aggregate orientations) and each of five temporal sequences. The obtained averaged velocity profile $\langle v_x(y)\rangle_{l,T}$ was further averaged over two stacks and different experimental runs.

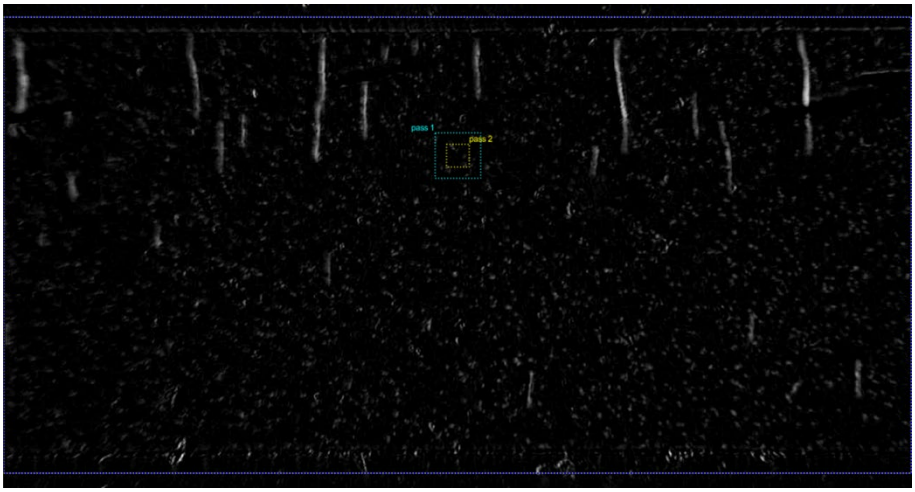

Figure 2.7: A snapshot of the microfluidic channel after grayscale inversion. Small coloured rectangles correspond to interrogation area selection. The long white strands are the aggregates, and the white dots are the polystyrene tracers.

2.5.3 Tracking of aggregate motion, size and concentration in recirculation flow experiments

Each of the two image stacks (with two orthogonal aggregate orientations) was obtained during the PIV pre-processing step [Sec. 2.5.2] was separately loaded into the Fiji image calculator. Then, each aggregate (appearing as a white rod – cf. Fig. 2.7) was labelled, while its geometrical centre (described by x_c, y_c -coordinates), length L and depth d were determined through fitting the intensity profile along its major and minor axes by a gaussian function, as described in detail in Supporting Information of our recent paper [Queiros Campos et al. (2021b)]. Collecting the data from all the snapshots of different stacks and temporal sequences, histograms of the aggregate lengths L were constructed. To get the aggregate concentration profile $\Phi(y)$ across the channel dimension y [cf. Fig. 2.4 for the axis definition], the y_c-positions of the aggregate centres were sorted to N equal intervals, $\Delta y_i = [(i-1)h/N, ih/N], i = 1..N$ and the sum of the aggregate volumes whose centres enter the given interval was calculated, assuming their ellipsoidal shape: $(\Sigma V_a)_i = (\Sigma(\pi L d^2/6))_i, y_c \in \Delta y_i$. The aggregate volume fraction in a given

interval was assessed by dividing this sum by the volume of the channel slice $V_i = \Delta y_i bl = hbl/N$ corresponding to the given interval: $\Phi(\Delta y_i) = (\Sigma V_a)_i / V_i$And the interval in the argument of Φ was replaced by its medium value $y_i = (i - 1/2)h/N$. Finally, the concentration profile $\Phi(y_i)$ All the analysed snapshots were averaged over two stacks and six different experimental runs. The $\Phi(y_i)$ data were obtained at $N = 20$. The average aggregate volume fraction across the whole channel was calculated as the sum of volumes of all aggregate in the given snapshot divided by the visualised channel volume, $\Phi_0 = \Sigma V_a/(hbl)$, the ratio being averaged over all the snapshots. It was also checked that the particle conservation condition, $\Phi_0 = (1/N)\sum_{i=1}^{N} \Phi(\Delta y_i)$, was satisfied.

To get the velocities of the aggregate displacement along the channel x axis, each image stack corresponding to two orthogonal aggregate orientations was sectioned into five smaller sub-stacks containing 40 images. Then, x_c-positions of the labelled aggregates were tracked within each sub-stack. The obtained $x_c(t)$-dependencies were globally linear for the time interval of the considered sub-stacks, with irregular deviations from linearity caused by hydrodynamic interactions with neighbouring aggregates. The $x_c(t)$, a linear function then fitted dependencies $x_c(t) = v_a t$ with a slope v_a corresponding to the x -component of the aggregate average speed. The v_a-values were collected for different stacks and temporal sequences corresponding to the steady recirculation flow and were analysed as a function of the aggregate length L and the geometrical position (y coordinate) in the channel.

2.5.4 Tracking of the polymer bead dissolution

The snapshots collected after recording the alginate bead dissolution were processed as follows. We have measured the microbead surface in the xy plane of the microfluidic channel [cf. Fig. 2.4 for axes definition] for each snapshot using the Image-J image calculator by "manual" determination of the microbead contour. The measurements were subject to the errors related to a diffuse character of the contour, so an error of the border position $\Delta\delta$ was determined for each snapshot and the error of the surface determination was then evaluated as $\Delta S = \Pi\Delta\delta$, where Π is the measured microbead perimeter. To quantify the importance of the bead dissolution, we introduce the relative bead surface as the surface at time *t* divided by the initial surface S_0 at $t = 0$, namely

$$s_n(t) = \frac{S(t)}{S_0}. \tag{2.5}$$

Thus, the bead dissolution is quantified through a decrease of the relative surface with time

Chapter 3. Self-assembly of the magnetic colloid under a rotating magnetic field

In this Chapter we are aimed to answer the first series of questions related to the target biomedical application and formulated in Sec. 1.3: Once the IONP is delivered in the vicinity of the blood clot, how efficient and how fast will be their self-assembly under rotating magnetic fields? The self-assembly timescale, how will it be compared to the duration of a typical surgical intervention? These questions impose a detailed study of the kinetics of field-induced self-assembly or phase separation of a magnetic colloid under low-frequency rotating magnetic fields. The applied field is expected to promote elongated aggregates synchronously rotating with the field. In experiments, we use a slightly destabilized aqueous suspension of citrated IONP (described in Sec. 2.1.1) and follow the aggregation process by simple optical visualization (as detailed in Sec. 2.3.1). Firstly, in Sec. 3.1, we report the results of these visual observations. Then, in Sec. 3.2, we develop a theoretical model allowing prediction of the aggregate size distribution and some integral characteristics (average size, number and volume fraction of aggregates). Finally, in Sec. 3.3, we compare experimental results on the aggregate size distribution and integral characteristics with the model predictions. Conclusions of these studies are resumed in Sec. 3.4, while Appendixes giving more details on the calculations are provided in Sec. 3.5.

3.1 Overview of observation results

The optical images of the microstructure of the diluted magnetic colloid (after treatment with salt/acid) were placed in a flat horizontal microfluidic channel of a depth of $h = 200$ μm, at a nanoparticle volume fraction $\varphi_0 = 1.6 \times 10^{-3}$, subjected to a homogeneous magnetic field rotating in the horizontal plane and having the amplitude $H_0 = 9$ kA/m are shown in Fig. 3.1 for four different frequencies (including 0 Hz – permanent field) and four different moments of elapsed time t. As seen from this figure, upon the magnetic field application, initially homogeneous magnetic colloid at $t = 0$ (first row in Fig. 3.1) is subjected to a phase separation manifested through the appearance of needle-like micron-sized aggregates composed of a large number of nanoparticles. We have not managed to conduct reliable measurements in the permanent magnetic field ($\nu = 0$) because, a few seconds after magnetic field application, the aggregates settled onto the bottom of the channel. Once settled, the aggregates were immobilized at the bottom and stopped to grow. Despite settling, the aggregates kept their needle-like shape, as seen in the left column of Fig. 3.1.

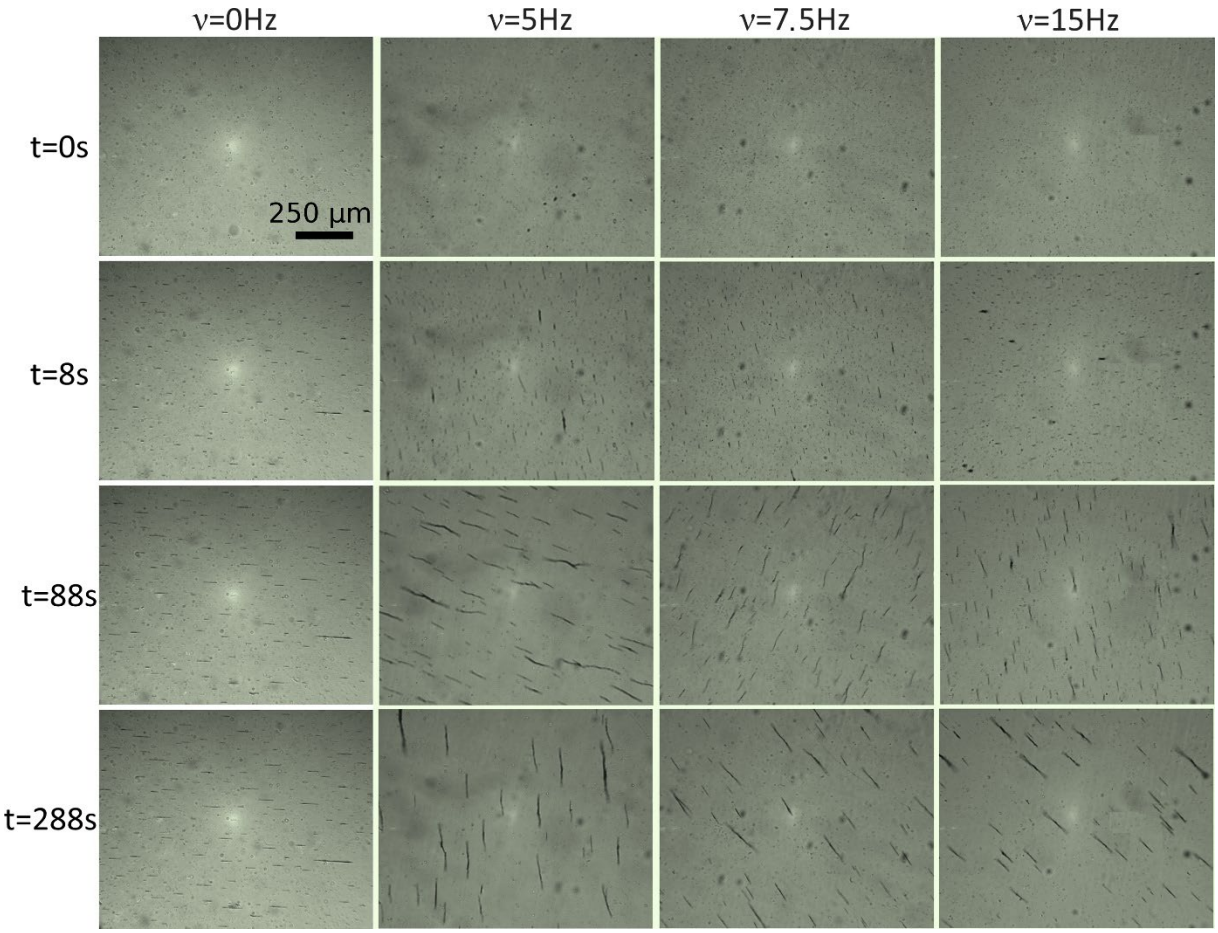

Figure 3.1: Snapshots of field-induced aggregates under permanent and rotating magnetic fields. Rows correspond to the elapsed time (from top to bottom) $t = 0, 8, 88$ and 288 s. Columns correspond to the field frequencies $\nu = 0, 5, 7.5,$ and 15 Hz. In the case of the permanent applied magnetic field (left column), the field is oriented horizontally. In the case of the rotating field (three right columns), the aggregates synchronously rotate with the field in the clockwise direction.

In the rotating field (three right columns in Fig.3.1), the aggregates rotate with the field in a clockwise direction without any visible settling. To check the rotational frequency of the aggregates, we have conducted a few supplementary short-time experiments using a high-speed camera. The rotational frequency of the aggregates coincides with the excitation frequency of the applied rotating magnetic field, the aggerate rotation is synchronous with the field in agreement with the low Mason number limit, as it will be shown in Sec. 3.2.1 [Eq. (3.1)]. At relatively short, elapsed times ($t \gtrsim 5$ s), the major part of the aggregates migrates vertically within the channel depth to a single horizontal plane situated approximately in the middle between two horizontal channel walls. Such effect has already been observed by Stikuts et al. (2020) for magnetic colloids qualitatively similar to our one and has been interpreted in terms of hydrodynamic interactions with walls hindering gravitational settling.

Notice that in all the snapshots of Fig. 3.1, we observe micron-sized spherical particles whose location does not change with time. These are dust particles that probably come from

the syringe joint and inevitably enter the microfluidic channel when it is reused several times for different experimental runs. Washing of the channel does not allow complete removal of these particles. Despite this drawback of our experimental system, we have never observed any distinguishable interaction between the dust particles deposited on the channel bottom and the magnetic aggregates rotating at the middle plane of the channel. Furthermore, the repeatability of experiments is confirmed for different states of the channel surface.

From the thermodynamic perspective, the aggregates are ascribed to the concentrated phase with the average particle volume fraction inside them evaluated to be $\varphi'' = 0.32 \pm 0.03$ [Sec. 3.5, Appendix 3-A], while the medium surrounding the aggregates is ascribed to the dilute phase with the average particle volume fraction φ decreasing with time starting from its initial value $\varphi_0 = 1.6 \times 10^{-3}$. These aggregates become visible at times as short as $t = 8$ s (second row of Fig. 3.1), and even at $t = 1$ s pointing out fast kinetics of nucleation. The aggregate size progressively increases with time (3rd and 4th rows in Fig. 3.1) thanks to coalescence between them (which is explicitly observed in the recorded videos and confirmed by the visual decrease of the number of observed aggregates per observation window) combined with absorption of individual nanoparticles from dilute phase (which is implicitly observed as the aggregate growth between two coalescence events). At elapsed times $t \gtrsim 100$ s, the coalescence of two aggregates is often accompanied by their fragmentation into three or four shorter parts. This fragmentation seems to limit the aggregate average size which seems to no longer increase at $t \gtrsim 200$ s. Coalescence and a few fragmentation events are also observed in recorded videos[5]. As opposed to the study of Stikuts et al. (2020), we do not observe the regular crystalline structure of monodisperse (in length) rotating aggregates at long times. The aggregate thickness in our case remains almost constant but the length is rather polydisperse (as analysed in Sec. 3.2.7) which likely hinders any order. The observations are qualitatively similar for all studied field frequencies in the range $5 \leq \nu \leq 25$ Hz (compare three right columns in Fig. 3.1). Fragmentation events are more frequent at higher frequency implying a decrease of the aggregate size with the frequency. The exact time dependence of the aggregate size will be analysed in Sec. 3.2.6. Notice that blurry tips of the aggregates in the two bottom rows of Fig. 3.1 result from the relatively long exposure time of the low-speed CMOS camera. If the field is rapidly switched off, the aggregates stop spinning, and we detect a sharp shape of their tips

[5] See two movies posted in Supplementary Materials of the paper [Raboisson-Michel al. J. Chem. Phys. 153(15), 154902 (2020)]

before the aggregates start to dissolve in the dilute phase under Brownian diffusion of nanoparticles.

Based on these primary observations, in Section 3.2, we will propose a theoretical model allowing the qualitative and quantitative description of the observed dynamics and kinetics.

3.2 Theory

3.2.1 General framework

Let us consider initially homogeneous suspension of superparamagnetic nanoparticles or nanoclusters (composed of superparamagnetic nanoparticles) dispersed in a Newtonian liquid of a viscosity η_0 at a volume fraction φ_0 and sandwiched between two horizontal planes separated by a relatively small distance of h (=200 μm in our experiments). In the absence of the applied magnetic field, the suspension is supposed to be stable against aggregation. The homogeneous and circularly polarized rotating magnetic field of an amplitude H_0 and angular frequency ω is applied at the moment $t = 0$. Above some critical values of H_0 and φ_0, magnetic attractive interactions between nanoparticles may induce a phase separation manifested through the appearance of needle-like aggregates, which in the low-frequency limit keep their straight shape assimilated to a prolate ellipsoid of the major and minor semi-axes denoted by a and b, respectively, and rotating synchronously with the magnetic field [Sandre et al. (1999)]. The aggregates will certainly have unequal sizes but most of them usually have a high aspect ratio $r_a = a/b \gg 1$ and are supposed to respect a linear magnetization law with a constant magnetic susceptibility χ at typical magnetic fields H_0~10 kA/m. Experiments show that at short times after the magnetic field application, all the aggregates move towards the same horizontal plane where they perform collective rotation, as pointed out in Sec. 3.1. An ensemble of rotating aggregates is schematically shown in Fig. 3.2a.

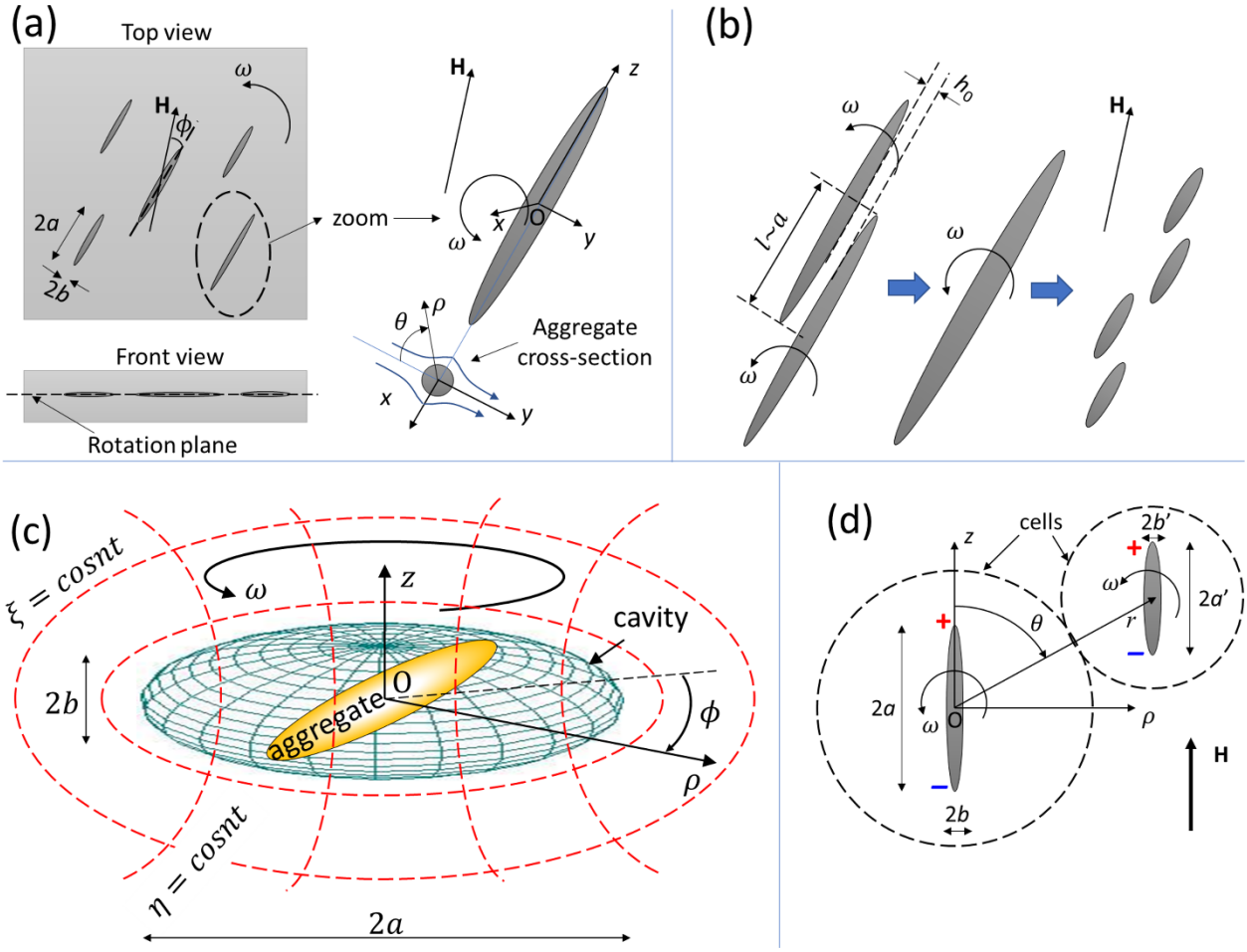

Figure 3.2: Problem geometry. The ensemble of ellipsoidal aggregates involved in counterclockwise rotation by a rotating magnetic field is shown in (a). The aggregates make a weak angle $\phi \ll 1$ with the instantaneous direction of the applied field **H** (top view) and all of them rotate in a single horizontal plane between the channel walls (front view). A magnified view of a single aggregate is illustrated on the right of (a), showing a relative motion of the suspending liquid relative to the aggregate and allowing the nanoparticle convective flux calculation. A possible fragmentation scenario with the transient coalescence of two aggregates followed by splitting into several parts is depicted in (b). The cavity model allowing the aggregate growth rate evaluation is schematized in (c). The aggregates rotate inside an oblate ellipsoidal cavity swept by the aggregate rotational motion; the nanoparticle transport towards the aggregates is realized in two steps: (i) diffusion from infinity towards the cavity and (ii) convective diffusion from the cavity to the aggregate across the diffusion boundary layer. The cell model used to evaluate the coagulation kernel is depicted in (d). The effective magnetic attraction between neighbouring aggregates is treated as the interaction between equivalent "+" and "–" charges placed on the aggregate tips.

In the inertialess limit, typically holding in the low-frequency range, the phase lag ϕ between the instantaneous orientation of the major axis of the aggregates and the magnetic field vector is given by the equilibrium between hydrodynamic and magnetic torques by the following expression, adapted from [Sandre et al. (1999)]:

$$\sin(2\phi) = Ma \approx \frac{8r_a^2\eta_0\omega(2+\chi)}{3(\ln(2r_a)-1/2)\mu_0 H_0^2\chi^2}, \tag{3.1}$$

where $\mu_0 = 4\pi \times 10^{-7}$H/m is the magnetic permeability of vacuum, and Ma is the Mason number defined as a characteristic ratio of the hydrodynamic-to-magnetic torque. Equation(3.1)

shows that the aggregates can synchronously rotate with the field only at $Ma \leq 1$. Furthermore, we consider the low Mason number limit, $Ma \approx 2\phi \ll 1$, respected in our experiments, for which possible effects of the phase lag ϕ on the aggregate magnetization and the supersaturation Δ can be neglected.

On the scale of the whole colloid, the evolution of aggregates is described by the distribution function $F(V, t)$ over the aggregate volumes V. The phase separation process is expected to be initiated by the nucleation, followed by the aggregate growth through absorption of individual nanoparticles, the aggregate coalescence under attractive dipolar interactions and possible fragmentation induced by hydrodynamic interactions or direct collisions between aggregates. It would be extremely difficult to handle simultaneously all these phenomena, but certain simplifications are hopefully possible. First, experiments show that the nucleation occurs at very short timescales and micron-sized aggregates appear at the times on the order of one second or less upon the magnetic field application [Ezzaier et al. (2017)]. This allows the consideration of the nucleation process as infinitely fast compared to all the other stages of aggregation. We manage to evaluate the average size and the aspect ratio of the critical nuclei used as an initial condition for the subsequent aggregation stages. Secondly, the possible fragmentation of aggregates at the later stage is considered implicitly through the limitation of the aggregate growth and the coalescence rates vanishing as the aggregates' average volume $\langle V \rangle$ achieves its maximal value dictated by the interplay between magnetic and hydrodynamic interactions. At such conditions, the aggregate size distribution function $F\ (V, t)$ must respect the population balance equation, in which the aggregate growth and the coalescence are explicitly considered, while the nucleation and fragmentation terms are omitted. This equation is similar to the one used in the condensation-driven coagulation model [Hassan and Hassan (2008)]:

$$\frac{\partial F(V,t)}{\partial t} + \frac{\partial}{\partial V}\left(\dot{V} \cdot F(V,t)\right) = \frac{1}{2}\int_0^V K(V', V - V')F(V - V', t)F(V', t)dV' - F(V,t)\int_0^\infty K(V, V')F(V', t)dV', \quad (3.2)$$

with the distribution function normalized to the number of aggregates per unit volume, or shortly, number density $n(t)$:

$$\int_0^\infty F(V,t)dV = n(t). \quad (3.3)$$

The second term on the left-hand side of Eq. (3.2) corresponds to the aggregate growth mechanism with the growth rate $\dot{V} \equiv dV/dt$ and the two terms of the right-hand side

correspond to the coalescence of aggregates with the coagulation kernel $K(V, V')$, which depends on attractive magnetic interactions between them. Diffusive term related to thermal fluctuations of the nanoparticle flux towards the aggregates is omitted – a conventional approximation in the theory of condensation valid for aggregate sizes larger than the size of the critical nuclei [Lifschitz and Pitajewski (1983)]. Notice that in the absence of coalescence terms, Equation (3.2) reduces to the classical Liouville equation often used for condensation phase transitions [Landau and Lifshitz (1980)], while in the absence of the convective (aggregate growth) term, Equation (3.2) reduces to classical Smoluchowski equation used for irreversible aggregation in colloidal systems [Levič (1962)].

3.2.2 Size of the critical nuclei

In the colloid composed of polydisperse nanoparticles, it is likely that the nuclei, composed of some smaller nanoparticles, appear on the surface of larger nanoparticles, giving rise to heterogeneous nucleation, as opposed to the homogeneous nucleation when the nuclei appear in the bulk of the colloid. According to the classical nucleation theory, only nuclei larger than some critical sizes can cross the nucleation barrier and continuously grow [Lifschitz and Pitajewski (1983)]. Assuming the critical nuclei to be much larger than their condensation centres (most significant nanoparticles in the suspension), the critical nuclei volume V_c is shown to be nearly the same as in the case of the homogeneous nucleation and is determined at the local maximum of the minimal work of nucleus formation ΔG [Kalikmanov (2013)]:

$$\left(\frac{\partial \Delta G}{\partial V}\right)_{V=V_c} = 0. \tag{3.4}$$

Following Zubarev and Ivanov (1997), we assume that in the presence of an external magnetic field, the nuclei of a given volume V have a shape of a prolate ellipsoid of an aspect ratio r_a, for which case the minimal work ΔG reads:

$$\Delta G = -N\Delta\mu + \sigma S = -\frac{\varphi''}{V_m} V k_B T \ln\frac{\varphi_0}{\varphi'} + \sigma V^{2/3} s(r_a), \tag{3.5}$$

where N is the number of individual nanoparticles of an average volume V_m constituting the nucleus; S and σ are nucleus surface area and surface tension, respectively; $\Delta\mu$ is the difference of chemical potentials of nanoparticles far from the nucleus and at its surface; $k_B T \approx 4.1 \times 10^{-21}$ J is the thermal agitation energy at room temperature; φ_0 is the initial nanoparticle volume fraction before the phase separation; φ' and φ'' are equilibrium nanoparticle volume fractions in the dilute phase (in the vicinity of the nucleus) and the concentrated phase (inside

the nucleus). The expression for the dimensionless surface area $s(r_a)$ for an elongated nucleus is provided in [Eq. (3.B1c)]. Substituting Eq. (3.5) into Eq. (3.4), we get the relationship between the volume and aspect ratio of the critical nucleus, while the length of the critical nuclei is related to its volume and aspect ratio by the obvious geometrical expression:

$$V_c = \left[\frac{2\sigma s(r_c)V_m}{3\varphi'' k_B T \ln(\varphi_0/\varphi')}\right]^3 \propto \left(\frac{\sigma}{k_B T}\right)^3 \langle d_m^9 \rangle, \tag{3.6a}$$

$$L_c = 2\left[\frac{3V_c r_c}{4\pi}\right]^{1/3}. \tag{3.6b}$$

The surface tension of the critical nuclei is taken to be the same as the surface tension of the supercritical aggregates. It depends on the amplitude H_0 of the applied magnetic field and its value was retrieved by fitting the experimental shape of the supercritical aggregates to the shape obtained theoretically by minimization of the aggregate free energy. Energy minimization provides an expression [Eq. (3.B4)] for the aggregate (nucleus) volume as a function of the aspect ratio. Equalizing right-hand parts of Eqs. (3.6a) and (3.B4) upon replacing r_a by r_c, we arrive at a transcendental equation for the aspect ratio r_c of the critical nuclei, which is solved numerically. The volume V_c and length L_c of the critical nuclei are then evaluated by injecting the numerical value of r_c into Eqs. (3.6a) and (3.6b), respectively. The unknown equilibrium volume fractions φ' and φ'' are retrieved from experiments on the aggregation threshold and the aggregate translational motion under applied magnetic field gradient. Finally notice that, according to Eq. (3.6a), $V_c \propto (\sigma V_m/k_B T)^3 \propto (\sigma/k_B T)^3 d_m^9$, where d_m is the diameter of individual nanoparticles constituting the nuclei. In the present case of polydisperse magnetic colloid, it seems reasonable to take a 9th moment of the particle size distribution $\langle d_m^9 \rangle$ [Eq. (2.2)] for evaluation of V_c, putting $V_m^3 = (\pi/6)^3 \langle d_m^9 \rangle$ in Eq. (3.6a).

In deriving Eq. (3.6a), we supposed that the phase equilibrium on the aggregate surface is not affected by the flow generated by the aggregate rotation such that the critical nuclei size is found to be independent of the field frequency. This strong hypothesis will be carefully inspected and confirmed in Sec. 3.3.1 in conjunction with an experimental phase diagram. The results on the critical nuclei size will be analysed in Sec. 3.3.2.

3.2.3 Maximal average aggregate volume

Now we move to the opposite limit of the phase separation process when rotating aggregates become so long that they are subject to hydrodynamic interactions with neighbouring aggregates. From the first glance, the average aggregate length can be limited by geometric constraints, i.e., when the circles described by extremities of rotating aggregates start

overlapping, in which case $n_s L_{max}^2 \sim 1$, with n_s – the number of aggregates per unit surface of the plane of their rotation. In experiments, L_{max} is usually much less than the value predicted by geometric arguments.

On the other hand, an aggregate can be rapidly fragmented into two parts, if at some moment, the hydrodynamic force F_h acting on the aggregate surface (in the hydrodynamic field created by the rotation of neighbouring aggregates) becomes tensile and overcomes the surface tension force F_s (acting as a compressive force tending to minimize the aggregate surface), as Zubarev et al. (2014) supposed for magnetorheological suspensions under shear. The characteristic ratio of these forces reads: $F_h/F_s = (\eta_0 \omega a^2)/(\sigma b)$ and is evaluated to be of the order of $F_h/F_s \sim 10^{-2} - 10^{-1}$ in our experimental conditions. Precise calculation shows that the maximal aggregate length overcomes by two orders of magnitude the maximal length stemming from geometrical considerations. Therefore, we must exclude this mechanism from consideration.

Alternatively, the aggregates can fragment upon a direct collision between each other. Strictly speaking, direct mechanical contacts are avoided by short-range lubrication interactions if the gap h_0 separating two approaching surfaces is more significant than typical surface roughness, which in the case of particle aggregates is on the order of magnitude of the average nanoparticle diameter $\langle d_p \rangle$ stemming from dynamic light scattering measurements. Collision dynamics of elongated aggregates is expected to be a quite complicated phenomenon involving non-trivial transient shapes, capillary waves and surface instabilities resulting in different outcomes, such as bouncing, coalescence, stretching or reflective separation (fragmentation), reported for droplet collisions [Qian and Law (1997)]. Detailed study of these dynamics is out of the scope of the present work. However, we can anticipate that more extended aggregates colliding at higher relative speeds ($\sim \omega a$) will be less stable to fragmentation than shorter ones by analogy with long liquid filaments forming during coalescence of two spherical drops and breaking up at high speeds because of surface instabilities. In our experiments, we observe that the collision between two long enough aggregates often produces coalescence on a very short timescale followed by fragmentation of the new aggerate into three of four parts. Furthermore, short-range hydrodynamic repulsion between aggregates during their collision certainly slows down their rotation and is expected to increase the phase lag ϕ between their major axis and the field. If the aggregates are long enough, the phase lag could overcome the critical value $\phi = \pi/4$, above which synchronous rotation of two colliding aggregates is no longer possible, as mentioned below Eq. (3.1). Asynchronous rotation of the pair of colliding aggregates

progressively increases the phase lag ϕ and when it achieves the value $\phi = \pi/2$, the aggregate magnetization takes its minimal value ($\sim 2H_0$ as opposed to $\sim \chi H_0$ at $\phi = 0$, with $\chi \gg 1$) for which the cohesive strength and surface tension of aggregates are expected to be minimal. This probably increases the probability of fragmentation. The fragmentation process is schematically presented in Fig. 3.2b.

For quantitative evaluation of the maximal aggregate size, we assume that during a collision, short-range lubrication interaction dominates over the hydrodynamic drag on rotating aggregates. We put therefore the rate of energy dissipation, w_{diss} through lubrication between laterally colliding aggregates equal to the power, w_m injected into the aggregate by the rotating magnetic field. The rate of dissipation w_{diss} is evaluated using the results of Christensen (1980) for two laterally approaching cylinders, while the power w_m is a product of the magnetic torque Γ_m [expression provided in Kuzhir et al. (2009)] taken at the transition between synchronous and asynchronous regimes ($\phi = \pi/4$) by the angular speed ω of aggregates equal to the angular frequency of the field:

$$w_{diss} \approx \frac{3}{4}\pi\eta_0 a^2 l\omega^2 \left(\frac{b}{h_0}\right)^{3/2}, \tag{3.7a}$$

$$w_m = \Gamma_m\omega = \frac{1}{2}\mu_0 H_0^2 \frac{\chi^2}{\chi+2}\sin(2\phi)\, V\omega = \frac{2}{3}\pi\mu_0 H_0^2 \frac{\chi^2}{\chi+2} ab^2\omega, \tag{3.7b}$$

where $l \sim a$ is the longitudinal overlap between two colliding aggregates [Fig. 3.2b], taken to be on the order of the aggregate semi-length a. Equating right-hand parts of Eqs. (3.7a) and (3.7b), we arrive at the expression for the maximal average aggregate aspect ratio:

$$r_{max} \approx \left(\frac{8}{9}\frac{\chi^2}{\chi+2}\frac{\mu_0 H_0^2}{\eta_0\omega}\right)^{1/2}\left(\frac{h_0}{b}\right)^{3/4}, \tag{3.8}$$

where the gap between two aggregates can be considered as an adjustable parameter of the order of one or a few nanoparticles' hydrodynamic diameters: $h_0 \sim \langle d_p \rangle$. In this formulation, the maximal aspect ratio is only defined by the collision between two isolated aggregates. It is expected to be defined by the interplay of coalescence and fragmentation events and their frequency. It could thus depend on the volume fraction Φ of aggregates in the suspension. However, the volume fraction Φ in our model and experiments shows only a moderate change with the field frequency ω and, within the range of our experimental parameters, we consider r_{max} to be independent of Φ. The maximal average aggregate length and volume are then found as

$$L_{max} = 2br_{max}, \tag{3.9a}$$

$$V_{max} = \frac{4}{3}\pi b^3 r_{max}. \tag{3.9b}$$

The two remaining unknowns in Eqs. (3.8) and (3.9), the aggregate half-thickness b is found to be nearly independent of the aggregate volume and is determined in Appendix 3-B, while the aggregate magnetic susceptibility χ is found in Appendix 3-A from the experiments on the translational motion of aggregates in the gradient magnetic field. The results of Eq. (3.9a) are compared with experiments in Sec. 3.3.2.

3.2.4 Aggregate growth rate

Once the critical nuclei appear, they continuously grow due to the absorption of individual nanoparticles from the dilute phase surrounding them. The transport of individual nanoparticles towards the aggregates arises thanks to three possible mechanisms as follows: (a) diffusion due to the difference of nanoparticle volume fraction far from the aggregates (φ) and in the vicinity of their surface (φ'), referred to as supersaturation $\Delta = \varphi - \varphi'$; (b) migration due to magnetic attraction of nanoparticles to the aggregate, referred to as magnetophoresis; and (c) convection when the rotating aggregate "collects" nanoparticles from the macroscopically quiescent dilute phase; in the reference frame rotating with the aggregate, the nanoparticles are convected towards the aggregate by the flow of the suspending liquid generated by the aggregate rotation. Analysis shows that in the considered high aspect ratio limit, $r_a \gg 1$, the magnetic field distribution around the aggregates is nearly homogeneous, except for the regions near the aggregate tips, and the magnetophoretic flux gives an insignificant contribution (logarithmic with the magnetic field intensity) to the aggregate growth rate for the considered range of dipolar coupling parameters $\lambda_d = m_p^2/(4\pi\mu_0 k_B T d_p^3) \sim 1 - 10$, where m_p is the nanoparticle magnetic moment [Ezzaier et al. (2017)]. Thus, the magnetophoretic flux can be safely neglected. Convective flux is compared to the diffusive flux through the Péclet number, defined for rotating aggregates with a linear velocity of its tip $\sim\omega a$, as follows:

$$Pe = \frac{2b\omega a}{D_p}, \tag{3.10}$$

where $D_p = 3\pi\eta_0 d_p/(k_B T)$ is the Brownian diffusivity of individual nanoparticles. The Péclet number takes the values $Pe \sim 10^2 - 10^3$ in our experimental conditions showing that the convective transport dominates over the diffusive one, except for a thin diffusive boundary layer close to the aggregate surface where the suspending liquid velocity takes small values in the reference frame of the aggregate due to non-slip hydrodynamic boundary condition. Under

such conditions, we can apply Levič's boundary layer approach developed for ion or small particle deposition onto the surface of large particles [Levič (1962)].

In the frames of this approach, we are looking for the volume flux J_V of nanoparticles towards the aggregate, which is related to the aggregate growth rate $\dot{V}$ through the following obvious expression:

$$J_V = \varphi'' \dot{V}, \tag{3.11}$$

with the known nanoparticle volume fraction inside the aggregates $\varphi'' \gg \varphi'$ defined in experiments (Appendix 3-A). The problem geometry is schematically presented on the magnified view of a single aggregate on the right of Fig. 3.2a.

Let us introduce the Cartesian reference frame *Oxyz* rigidly attached to the aggregate with the origin *O* placed into the aggregate geometric centre and *z*–axis oriented along the major aggregate axis. The aggregate rotates with an angular frequency ω around the *x*-axis. Analysis shows that for a long aggregate, $r_a \gg 1$, in the vicinity of the aggregate surface, the longitudinal *z* component of the velocity is much smaller than the transverse *x* and *y* components. At such conditions, the nanoparticle capture by unit aggregate length can be approximated as a convective diffusion of particles towards a cylinder placed into a homogeneous flow field with the fluid velocity at infinity equal to $u_\infty = \omega z$ at a given axial position *z*, and with the volume flux j_V per unite aggregate length given by the following expression [Adamczyk and Van De Ven (1981)]:

$$j_V = c A_f^{1/3} D_p Pe_z^{1/3} \Delta, \tag{3.12a}$$

$$A_f \approx \frac{1}{2(\ln(2r_a) - 1/2)} \frac{\hat{r}^2}{\hat{r}^2 + \hat{z}^2 / r_a^2}, \tag{3.12b}$$

where $c \approx 3.644$; A_f is the hydrodynamic coefficient derived in Appendix 3-C and coming from the velocity field in the vicinity of the rotating aggregate; $Pe_z = Pe \cdot \hat{r}\hat{z}$ is the local Péclet number at a given position *z*, related to the global Péclet number Pe given by Eq. (3.10); $\hat{r} = r/b$ and $\hat{z} = z/a$ are dimensionless radial and axial coordinates of the aggregate surface related through

$$\hat{r}^2 + \hat{z}^2 = 1.$$

The volume flux J_V is obtained by integration of the linear flux density j_V over the aggregate length:

$$J_V = 2a\int_0^1 j_V d\hat{z} = \frac{k}{(\ln(2r_a)-1/2)^{1/3}} D_p a Pe^{1/3}\Delta, \quad (3.13)$$

with $k \approx 1.931$.

The particle volume flux evaluated by Eq. (3.13) is likely overestimated because of the following reason. When the aggregate rotates under an applied rotating magnetic field, it absorbs some part of neighbouring single nanoparticles. At each new period of its rotation, the aggregate can encounter fewer and fewer nanoparticles. Thus, the convective flux can be substantially reduced by a few spins after the beginning of the rotation. The particle transport in this situation can be evaluated using the following simple model. During its rotation, the aggregate sweeps a volume (hereinafter called a cavity) having a shape of an oblate ellipsoid formed by the revolution of the outer border of the aggregate's boundary layer, as shown schematically in Fig. 3.2c. Neglecting boundary layer thickness, the cavity has two major semi-axes equal to the aggregate half-length a and the minor semi-axis equal to the aggregate half-thickness b.

We suppose that inside the cavity the particle transport is convection-diffusive and respects the boundary layer approach [Eq. (3.13)], with the only difference that the average nanoparticle volume fraction inside the cavity (excluding the aggregate with its boundary layer) takes some unknown value φ_c, intermediate between the volume fractions in the vicinity of the aggregate surface (φ') and at the infinity from the cavity (φ), so that $\varphi' < \varphi_c < \varphi$. We further suppose that the nanoparticles outside the cavity enter inside the cavity by diffusion thanks to the concentration difference $\varphi - \varphi_c$. The diffusive volume flux J_{V1} towards the cavity is given by the following expression, developed in Appendix 3-D:

$$J_{V1} = 8D_p a(\varphi - \varphi_c), \quad (3.14)$$

while the convection-diffusive flux J_{V2} towards the aggregates inside the cavity is given by Eq. (3.13), in which the supersaturation Δ has to be replaced by $(\varphi_c - \varphi')$. In the conventional approximation of quasi-stationary particle transport, both fluxes J_{V1} and J_{V2} are the same. Eliminating φ_c, we arrive at the following expression for the volume particle flux, which accounts for both the emptying of the cavity through particle absorption by the rotating aggregate and the filling of the cavity by particle diffusion towards the cavity:

$$J_V = J_{V1} = J_{V2} = \left[\frac{8(\ln(2r_a)-1/2)^{1/3}}{kPe^{1/3}} + 1\right]^{-1} 8D_p a\Delta. \quad (3.15)$$

This last equation shows that at the Péclet number limit $Pe^{1/3} \gg 8(\ln(2r_a) - 1/2)^{1/3}/k \gg 1$ corresponding to high enough excitation frequency ω, the particle flux reduces to Eq. (3.14) where $(\varphi - \varphi_c)$ must be replaced by Δ. The particle transport is dominated by diffusion towards the cavity because the aggregates rotate fast enough and rapidly empty the cavity such that the volume fraction φ_c in the cavity approaches the equilibrium value φ'. In the limit $1 \ll Pe^{1/3} \ll 8(\ln(2r_a) - 1/2)^{1/3}/k$, corresponding to lower frequencies ω, the particle flux reduces to Eq. (3.13). The transport is dominated by convective diffusion towards the aggregate, while the cavity has enough time to be filled by nanoparticles from outside during the aggregate rotation period. In our experimental conditions, we are an intermediate situation, so the complete expression (3.15) for the particle flux has to be used. To get the aggregate growth rate $\dot{V}$ as a function of the aggregate volume V only, we have to express its geometrical characteristics a, b and $r_a = a/b$ through V. This is done in Appendix 3-B by minimization of free energy of a single aggregate of a given volume V with respect to its aspect ratio. As mentioned in Sec. 3.1, in our experimental conditions, the aggregate half-thickness b appears to be nearly independent of the volume [Eq. (3-B6)] and approximate expressions for $a(V, b)$, and $r_a(V, b)$ can be easily obtained from the aggregate volume $V = 4\pi ab^2/3$:

$$a = \frac{3V}{4\pi b^2}, \qquad r_a = \frac{3V}{4\pi b^3}. \tag{3.16}$$

Combining Eqs. (3.10), (3.11), (3.15), (3.16) and neglecting logarithmic variation of the aspect ratio setting it equal to the maximal value [Eq. (3.8)], $r_a \approx r_{max}$, we arrive at the following expression for the aggregate growth rate:

$$\dot{V} \approx \left[\frac{\alpha}{(V/V_{max})^{1/3}} + 1\right]^{-1} \frac{6D_p V}{\varphi'' \pi b^2}\Delta, \tag{3.17a}$$

$$\alpha = \frac{8(\ln(2r_{max}) - 1/2)^{1/3}}{kPe_{max}^{1/3}}, \qquad Pe_{max} = \frac{3V_{max}\omega}{2\pi D_p b} \tag{3.17b}$$

where Pe_{max} is the Péclet number for the aggregates of the maximal volume given by the combination of Eqs. (3.8), (3.9b).

As the aggregates absorb nanoparticles from the surrounding dilute phase, the particle volume fraction in the dilute phase, and consequently, the supersaturation Δ progressively decreases with time. The supersaturation can be expressed through the average aggregate volume $\langle V \rangle$ using the particle volume conservation condition $\varphi(1 - \Phi) + \varphi''\Phi = \varphi_0$, where Φ is the volume fraction of aggregates defined as the ratio of the volume occupied by aggregates to the volume of the whole suspension. At low concentrations of the colloid, $\varphi_0 \ll 1$ and at a

typical internal volume fraction of aggregates $\varphi''\sim 0.3$ [cf. Appendix 3-A], the strong inequality $\Phi \ll 1$ holds. With this in mind, and considering that $\Phi = n\langle V\rangle$, we get the following approximate expression for the supersaturation:

$$\Delta = \varphi - \varphi' = \Delta_0 - \varphi'' n\langle V\rangle, \tag{3.18}$$

where $\Delta_0 = \varphi_0 - \varphi'$ is the initial supersaturation and n is the number of aggregates per unit volume (number density).

Equation (3.18) shows that, in absence of hydrodynamic interactions and coalescence or fragmentation events (implying constant number density $n = const$), the aggregates grow until their average volume achieves the maximal value $V_{eq} = \Delta_0/(\varphi'' n)$ when the system tends to thermodynamic equilibrium and the supersaturation tends to zero. In these conditions, the supersaturation can be written as: $\Delta = \Delta_0\left(1 - \langle V\rangle/V_{eq}\right)$. In reality, because of hydrodynamic interactions and collisions between rotating aggregates, they fragment, and their growth is limited by the maximal average volume $V_{max} < V_{eq}$. This means that at the end of the phase separation under rotating fields, the supersaturation will not achieve zero value. However, the aggregate growth (due to remaining supersaturation $\Delta \neq 0$ and possible coalescence) is expected to be counterbalanced by the fragmentation of aggregates. The simplest way to account for fragmentation is to require a zero growth rate $\dot{V}$ as the average volume $\langle V\rangle$ achieves its maximal value V_{max}. It can be done by replacing V_{eq} by V_{max} in the expression for Δ, which after replacement in Eq. (3.17a) gives the final expression for the aggregate growth rate:

$$\dot{V} \approx \left[\frac{\alpha}{(V/V_{max})^{1/3}} + 1\right]^{-1} \frac{6D_p V}{\varphi'' \pi b^2} \Delta_0 \left(1 - \frac{\langle V\rangle}{V_{max}}\right), \tag{3.19}$$

which depends on the magnetic field frequency ω intervening into the constant α [Eq. (3.17b)] and the maximal average volume V_{max} [Eqs. (3.8), (3.9b)], as well as on the magnetic field amplitude H_0 intervening into V_{max} and initial supersaturation Δ_0.

3.2.5 Coagulation kernel

The aggregates of a supercritical volume, $V > V_c$ can also coalesce thanks to attractive dipolar interactions at the same time as they grow by absorption of individual nanoparticles. The coalescence rate is expressed through the so-called coagulation kernel $K(V, V')$, which in general depends on volumes V and V' of two merging aggregates and is related to the magnetophoretic flux $J_{V'\to V}$ of all the aggregates V' towards a target aggregate V by the following expression:

$$J_{V\prime\to V} = K(V,V')n_{V\prime}, \tag{3.20}$$

where $n_{V\prime} = F(V',t)dV'$ is the number density of aggregates V'in the suspension.

This flux is evaluated in Appendix 3-E based on the cell model [Fig. 3.2d], and explicit expression [Eqs. 3-E4] for the coagulation kernel is provided. Analysis shows that in the considered ranges of the aggregate aspect ratios ($r_a = 5 - 50$) and size ratios ($V/V' \approx r_a/r_a{}' = 1/10 - 10$), as well as at a moderate increase of the volume fraction Φ of the aggregates with the time [Sec. 3.3.3, Fig. 3.6], the coagulation kernel varies maximum by $\sim \pm 20\%$ with respect to some average value. Such variations are rather inessential as compared to those observed in various coagulation processes such as shear-induced coagulation, branched polymerization, etc. [Aldous (1999)]. It is, therefore, reasonable to consider the coagulation kernel to be constant: $K(V,V) \approx const \equiv K_0$, where K_0 is hereinafter referred to as coagulation constant. For definiteness, we take the value of K_0 at the aggregate aspect ratio equal to half of its maximal average value imposed by hydrodynamics [Eq. (3.8)] and at the aggregate volume fraction Φ equal to the known initial value Φ_0. Thus, K_0 is calculated by Eqs. (3-E4) in which the aspect ratio is set to $r_a = r_a' = r_{max}/2$ and Φ is replaced by Φ_0.

Aggregate coalescence with constant coagulation kernel is expected to lead to indefinite aggregate growth. However, fragmentation induced by hydrodynamic interactions must limit this growth to the maximal average volume evaluated by Eqs. (3.8), (3.9b). The simplest way to handle this problem without introducing fragmentation kernels is to impose a progressive decrease of the coagulation constant with an increasing average aggregate volume $\langle V \rangle$ until $K = 0$ at $\langle V \rangle \to V_{max}$. Among different possibilities, this can be done by multiplying the coagulation constant by $1 - \langle V \rangle / V_{max}$. The expression for the modified coagulation constant depending on time and implicitly accounting for fragmentation reads:

$$K(t) = K_0 \left(1 - \frac{\langle V \rangle}{V_{max}}\right). \tag{3.21}$$

In summary, the coagulation kernel $K(V,V')$ in the population balance equation [Eq. (3.2)] must be replaced by the time-dependent coagulation constant $K(t)$ which, according to Eq. (3-E4a) scales as $K(t) \sim \mu_0 \chi^2 H_0^2 b^2 h/\eta_0$.

3.2.6 Integral characteristics

Having defined the aggregate growth rate and the coagulation kernel, we can proceed with the solution of the population balance equation [Eq. (3.2)], which can be rewritten in the following dimensionless form:

$$\frac{\partial\psi(v,\tau)}{\partial\tau} + (1-\langle v\rangle)\frac{\partial}{\partial v}[g(v)\psi(v,\tau)] = \frac{1}{2}\kappa_0(1-\langle v\rangle)\int_0^v \psi(v-v',\tau)\psi(v',\tau)dv' - \kappa_0(1-\langle v\rangle)\psi(v,\tau)\int_0^\infty \psi(v',\tau)dv', \tag{3.22a}$$

$$g(v) = \left[\alpha v^{-4/3} + v^{-1}\right]^{-1}, \tag{3.22b}$$

introducing the following dimensionless quantities: $v = V/V_{max}$ and $\langle v\rangle = \langle V\rangle/V_{max}$ for the aggregate volume, $\psi(v,\tau) = (V_{max}^2/\Phi_0)F(V,t)$ for the size distribution function, $\tau = t/t_d$ for the time and $\kappa_0 = t_d/t_c$ for the ratio of the diffusion and coalescence timescales given by the following expressions:

$$t_d = \frac{\pi b^2\varphi''}{6D_p\Delta_0}, \qquad t_c = \frac{V_{max}}{K_0\Phi_0}. \tag{3.23}$$

The parameter κ_0 allows switching between aggregate growth mechanisms at $\kappa_0 \to 0$ and coalescence mechanism at $\kappa_0 \to \infty$, while both mechanisms coexist at intermediate values $\kappa_0 = O(1)$ relevant for our experiments. The analytical solution of Eq. (3-22a) does not exist for the function $g(v)$ given by Eq. (3-22b). However, at the values $\alpha \leq 1$, relevant for our experiments, within the maximal error of 6%, the function $g(v)$ can be replaced by its linearized form:

$$g(v) \approx \frac{v}{1+\alpha} \equiv \beta v, \tag{3.24}$$

with $\beta = 1/(1+\alpha)$ and α given by Eq. (3-17b) as a function of the Péclet number. Using Eq. (3-24), and introducing a change of variables $(1-\langle v\rangle)d\tau \equiv d\Theta$, the population balance equation takes the following approximate form:

$$\frac{\partial\psi(v,\Theta)}{\partial\Theta} + \beta\frac{\partial}{\partial v}[v\,\psi(v,\Theta)] = \frac{1}{2}\kappa_0\int_0^v \psi(v-v',\Theta)\psi(v',\Theta)dv' - \kappa_0\psi(v,\Theta)\int_0^\infty \psi(v',\Theta)dv'. \tag{3.25}$$

This equation has a similar mathematical structure that the one of dropwise condensation [Cueille and Sire (1997)], except for the dimensionless time τ replaced in our case by the variable Θ, which measures the dimensionless time in a compressed timescale allowing for limitation of the aggregate growth. Multiplying Eq. (3.25) by $v^j, j = 0,1$ and integrating over

v, taking into account that $v^j\psi \to 0$ at $v \to \infty$, we get two independent ordinary differential equations for the 0th and the 1st moments $M_j(\Theta) = \int_0^\infty \psi(v,\Theta)v^j dv$ $(j = 0,1)$ of the size distribution function $\psi(v,\Theta)$, as follows:

$$\frac{dM_0}{d\Theta} = -\frac{1}{2}\kappa_0 M_0^2, \qquad \frac{dM_1}{d\Theta} = \beta M_1. \tag{3.26}$$

The solution of these equations at appropriate initial conditions allows finding the integral characteristics of phase separation, i.e., the aggregate number density n, the volume fraction of aggregates Φ and the dimensionless aggregate average volume $\langle v\rangle$ as a function of the reduced dimensionless time Θ:

$$\frac{n(\Theta)}{n_0} = v_0 M_0(\Theta) = \left[1 + \frac{\kappa_0\Theta}{2v_0}\right]^{-1}, \tag{3.27a}$$

$$\frac{\Phi(\Theta)}{\Phi_0} = M_1(\Theta) = e^{\beta\Theta}, \tag{3.27b}$$

$$\langle v\rangle(\Theta) = \frac{M_1(\Theta)}{M_0(\Theta)} = v_0 e^{\beta\Theta}\left[1 + \frac{\kappa_0\Theta}{2v_0}\right], \tag{3.27c}$$

where n_0, Φ_0 and v_0 are initial values of the number density, volume fraction of aggregates and dimensionless average volume, respectively. The initial volume can be evaluated as the dimensionless average volume of critical nuclei: $v_0 = V_c/V_{max}$ [Eqs. (3.6a), (3.9b)]. One of the two parameters, n_0 or Φ_0 is supposed to be known from experiments and the remaining parameter is found through the relationship $n_0 = \Phi_0/v_0$. Finally, the dimensionless time τ is obtained from the reduced time Θ, using Eq. (3.27c):

$$d\tau = \frac{d\Theta}{1-\langle v\rangle} \Rightarrow \tau(\Theta) = \int_0^\Theta \frac{d\Theta'}{1 - v_0 e^{\beta\Theta'}[1+\kappa_0\Theta'/(2v_0)]}, \tag{3.28}$$

where the integral is evaluated numerically.

Since the dimensionless average volume is limited from above by $\langle v\rangle = 1$ (corresponding to $\langle V\rangle = V_{max}$), the reduced time cannot overcome a maximal value Θ_{max} coming from the solution of the following transcendental equation:

$$v_0 e^{\beta\Theta_{max}}\left[1 + \frac{\kappa_0\Theta_{max}}{2v_0}\right] = 1. \tag{3.29}$$

In summary, time dependencies of the integral characteristics of field-induced phase separation are evaluated in parametric form with the help of Eqs. (3.27) and (3.29), using the reduced time Θ as a parameter and varying its value from 0 to Θ_{max}. These dependencies will

be compared with experimental ones. Notice that, under-considered approximation $g(v) \propto v$ [Eq. (3.24)], equivalent to the linear aggregate growth rate, $\dot{V} \propto V\Delta$, the integral characteristics depend only on the initial dimensionless average volume v_0 but are fully independent of the shape of the initial size distribution $\psi(v,0)$. This has allowed us to find them without solving the population balance equation (3.25).

3.2.7 Size distribution

The size distribution function $\psi(v,\Theta)$ can be obtained by solution of Eq. (3.25) at some known initial size distribution $\psi(v,0) \equiv \psi_0(v)$. Following Cueille and Sire (1997) and Hassan and Hassan (2008), applying the Laplace transform to the distribution function, $\Psi(p,\Theta) = \mathcal{L}[\psi(v,\Theta)] = \int_0^\infty e^{-pv}\psi(v,\Theta)dv$ (with p being a complex frequency parameter), the integral-differential equation (3.25) is transformed into the following partial differential equation for $\Psi(p,\Theta)$:

$$\frac{\partial\Psi(p,\Theta)}{\partial\Theta} - \beta p\frac{\partial\Psi(p,\Theta)}{\partial p} = \frac{1}{2}\kappa_0\Psi^2(p,\Theta) - \kappa_0\Psi(0,\Theta)\Psi(p,\Theta), \quad \Psi(0,\Theta) = M_0(\Theta), \quad (3.30)$$

whose analytical solution, obtained by the method of characteristics, reads:

$$\Psi(p,\Theta) = \frac{(1-\vartheta)^2\Psi_0(p,\Theta)}{1-v_0\vartheta\Psi_0(p,\Theta)},\ \Psi_0(p,\Theta) = \int_0^\infty e^{-pv\exp(\beta\Theta)}\psi_0(v)dv,\ \vartheta = \frac{\kappa_0\Theta/(2v_0)}{1+\kappa_0\Theta/(2v_0)}. \quad (3.31)$$

For comparison with experiments, it is more convenient to introduce the dimensionless distribution function $f(v,\Theta)$ with its 0th and 1st moments defined as follows:

$$f(v,\Theta) \equiv \frac{\psi(v,\Theta)}{M_0(\Theta)}, \qquad \int_0^\infty f(v,\Theta)dv = 1, \quad \int_0^\infty f(v,\Theta)vdv = \langle v\rangle. \qquad (3.32)$$

Combining Eqs. (3.31) and (3.32), we arrive at the following expression for the size distribution function $f(v,\Theta)$ evaluated at a given initial distribution $f(v,0) \equiv f_0(v)$:

$$f(v,\Theta) = \mathcal{L}^{-1}\left[\frac{(1-\vartheta)\Xi_0(p,\Theta)}{1-\vartheta\,\Xi_0(p,\Theta)}\right], \qquad \Xi_0(p,\Theta) = \int_0^\infty e^{-pv\exp(\beta\Theta)}f_0(v)dv, \qquad (3.33)$$

where $\mathcal{L}^{-1}[X]$ stands for the inverse Laplace transform of X, which in case of an arbitrary initial size distribution $f_0(v)$ has to be evaluated numerically. However, explicit analytical expression can be provided for some physically relevant cases.

With a large size limit, $e^{-\beta\Theta}v/v_0 \gg 1$, the frequency domain can be safely restricted to the p-values respecting strong inequality $pv_0e^{\beta\Theta} \ll 1$ allowing the approximate expansion, $e^{-pv\exp(\beta\Theta)} \approx 1 - pv\exp(\beta\Theta)$, and leading to the following expression for $f(v,\Theta)$:

$$f(v,\Theta) \approx \frac{1}{v_0}\left[1+\frac{\kappa_0\Theta}{2v_0}\right]^{-1}\exp\left[-\beta\Theta-\frac{e^{-\beta\Theta}v/v_0}{1+\kappa_0\Theta/(2v_0)}\right],\ \text{at}\ \frac{e^{-\beta\Theta}v}{v_0}\gg 1. \tag{3.34}$$

In the large size and long-time limits, the last equation reduces to:

$$f(v,\Theta) \approx \frac{2}{\kappa_0\Theta}\exp\left[-\beta\Theta-\frac{2e^{-\beta\Theta}v}{\kappa_0\Theta}\right],\ \text{at}\ \frac{e^{-\beta\Theta}v}{v_0}\gg 1,\ \ \frac{\kappa_0\Theta}{2v_0}\gg 1, \tag{3.35}$$

showing that the distribution function no longer depends neither on the initial size distribution nor on the initial average volume v_0, as typically encountered in classical coagulation problems [Aldous (1999)]. Furthermore, in absence of the aggregate growth between coalescence events, $\beta = 0$, $\Theta = \tau$, the equation (3.34) reduces to the well-known solution of the Smoluchowski equation with the constant kernel, which is conventionally written as follows [Aldous (1999)]: $\psi(v,\tau) = M_0(\tau)f(v,\tau) \approx [2/\tau']^2\exp[-2v/\tau'],\ \text{at}\ v/v_0 \gg 1,\ \ \tau'/(2v_0) \gg 1\,,\quad \text{with}\quad \tau' = \kappa_0\tau$.

The asymptotic solutions [Eqs. (3.34) and (3.35)] typically provide valuable information on the size distribution shape in the broad volume interval predicting a continuous decrease of the distribution function $f(v,\Theta)$ with increasing dimensionless volume v. However, they lose the details of the size distribution shape at small volumes, such as an initial increase of $f(v,\Theta)$ with v. These details can be captured with the exact solution [Eq. (3.33)]. For the special case of the initial size distribution

$$f_0(v) = \frac{1}{m!}\left(\frac{m+1}{v_0}\right)^{m+1} v^m e^{-\frac{(m+1)v}{v_0}}, m \in \mathbb{N}_0, \tag{3.36}$$

relevant for our experiments at the appropriately chosen value of m, the distribution function [Eq. (3.33)] is explicitly expressed through v, Θ, as follows:

$$f(v,\Theta) = \frac{1-\vartheta}{v_0 e^{\beta\Theta}\vartheta}\sum_{j=1}^{m+1}\left[\left(1+\frac{v_0 e^{\beta\Theta}}{m+1}p_j\right)e^{p_j v}\right], \tag{3.37a}$$

$$1-\vartheta+\sum_{j=1}^{m+1}\left[C_{m+1}^{j}\left(\frac{v_0 e^{\beta\Theta}}{m+1}\right)^{j}p_j\right] = 0, \tag{3.37b}$$

where p_j are $(m+1)$ complex roots of the polynomial equation (3.37b), evaluated analytically at $m \le 3$ or numerically at $m \ge 4$; C_{m+1}^{j} are binomial coefficients, and the coefficient ϑ is expressed through the reduced time Θ by the last expression in Eq. (3.31). Notice that Eq. (3.37) reduces to Eq. (3.34) for $m = 0$, i.e. for the exponential initial distribution $f_0(v) = v_0^{-1}e^{-v/v_0}$.

Finally, note that the time (τ) dependence of the size distribution is obtained in parametric form, $[f(v,\Theta),\tau(\Theta)]$ using one of the equations (3.33), (3.34), (3.35) or (3.37a) for $f(v,\Theta)$ and Eq. (3.28) for $\tau(\Theta)$ by varying the parameter Θ in the range $\Theta \in [0,\Theta_{max}]$, with Θ_{max} given by the numerical solution of Eq. (3.29). The obtained theoretical size distribution will be compared to the experimental one in Sec. 3.3.4.

3.3 Quantitative results and discussion

In this Section, we present the results of quantitative characteristics of the field-induced phase separation obtained through experimental measurements (detailed in Sec. 2.4.1) and theoretical modelling (presented in Sec. 3.2). We start with a detailed inspection of the threshold of field-induced phase separation through the experimental $H_0 - \varphi$ phase diagram [Sec. 3.3.1]. Then we report the aggregates' minimal and maximal average size [Sec. 3.3.2], the integral characteristics of the phase separation [Sec. 3.3.3], and the aggregate size distribution [Sec. 3.3.4]; most of these experimental characteristics will be compared to predictions of our model.

3.3.1 Phase diagram and initial supersaturation

The amplitude of the threshold magnetic field H_0 of the phase separation was measured as a function of nanoparticle volume fraction φ' at different frequencies of the magnetic field, including $\nu = 0$ (permanent field). Notice that gravitational settling in the permanent field is slow enough for small initial aggregates and does not hinder the determination of the aggregation threshold. It has been found that within the experimental errors, the field frequency does not affect the $H_0(\varphi')$-dependency in the range $0 \leq \nu \leq 25$ Hz. Thus, the experimental $H_0(\varphi')$-dependency is plotted in Fig. 3.3 for the permanent magnetic field only. The error bars correspond to the standard deviation determined from a series of three equivalent measurements. The $H_0(\varphi')$ dependency follows common trends typically observed for permanent fields [Buyevich and Ivanov (1992), Ezzaier et al. (2017)].

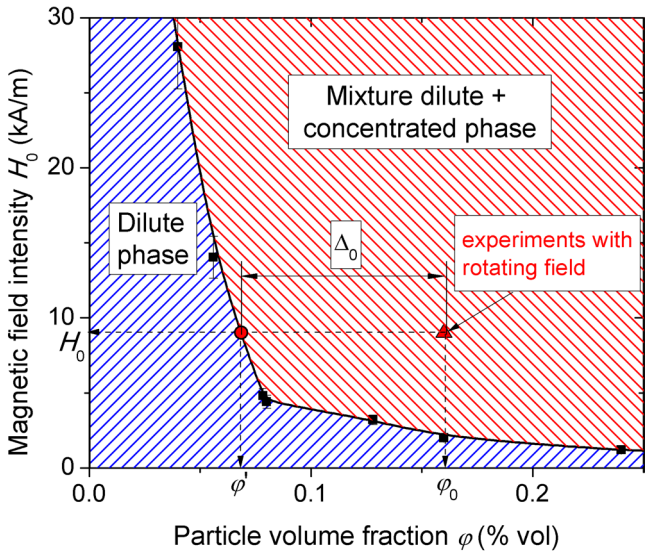

Figure 3.3: $H_0 - \varphi$ phase diagram of the diluted magnetic colloid treated by salt/acid addition in the permanent magnetic field. The phase diagram appears to be the same (within experimental error bars) in the rotating field in the frequency range $5 \leq \nu \leq 25\ Hz$.

First, the phase separation threshold is shifted to lower magnetic fields with increasing volume fraction φ'. This is understood in terms of increasing dipolar interactions between nanoparticles, as the average distance between them decreases with increasing volume fraction. Second, the $H_0(\varphi')$-curve separates the $H_0 - \varphi$ space into two regions, as follows: (a) the dilute phase region on the left, represented by a blue hatch in Fig. 3.3, where the applied field cannot induce the phase separation, and (b) the mixture of the dilute and concentrated phases on the right represented by a red hatch with the phase separation manifested through the appearance of needle-like aggregates (concentrated phase) surrounded by a suspension of individual non-aggregated nanoparticles (dilute phase). In this context, the $H_0 - \varphi$ space can be considered as a phase diagram and $H_0(\varphi')$-curve – as the left binodal curve since the considered phase separation is nothing but the binodal decomposition of the magnetic colloid under the applied field. The second binodal curve $H_0(\varphi'')$ marking the transition between the concentrated bulk phase and the mixture of both phases is not easily accessible in experiments and thus not plotted in Fig. 3.3. Tedious experiments on hydrodynamic mobility of aggregates under magnetic field gradient allowed the determination of the volume fraction $\varphi'' = 0.32 \pm 0.03$ in the concentrated phase for the single value of the magnetic field amplitude $H_0 = 9\ \mathrm{kA/m}$ [Appendix 3-A]. Third, the phase diagram allows experimental evaluation of the suspension's initial supersaturation Δ_0 as the difference between the nanoparticle volume fraction $\varphi_0 = 1.6 \times 10^{-3}$ in the suspension and the volume fraction φ' at the aggregation threshold. For the magnetic field amplitude $H_0 = 9\ \mathrm{kA/m}$ used in all kinetic experiments, we find $\varphi' \approx 7 \times 10^{-4}$ and $\Delta_0 = \varphi_0 - \varphi' \approx 9 \times 10^{-4}$. The initial supersaturation is graphically represented in Fig. 3.3

by a horizontal segment relating to the point (φ', H_0) on the binodal curve with the point (φ_0, H_0) representing the initial state of our suspension at the beginning of the phase separation. Recall that the binodal curve does not depend on the field frequency, therefore, the value $\Delta_0 \approx 9 \times 10^{-4}$ found for the permanent field remains valid for rotating fields in the frequency range $0 \leq \nu \leq 25$ Hz.

The independence of the phase separation threshold of the frequency likely indicates that the phase equilibrium on the surface of aggregates between the dilute (outside the aggregates) and the concentrated (inside the aggregates) phases is not altered by aggregate rotation, at least in the considered frequency range. At all experimental frequencies, the aggregates have a high enough aspect ratio, $r_a > 5$ and very small phase lag, $\phi \sim 0.1°$, between their main axis and the field direction, as evaluated by Eq. (3.1). Under such conditions, the demagnetizing effects (arising due to refraction of the field lines on the aggregate surface) can be safely neglected. Thus, the distribution of the instantaneous magnetic field on the surface of the aggregates is supposed to be unaltered by the aggregate rotation and cannot change the phase equilibrium. On the other hand, the aggregate rotation generates the hydrodynamic pressure, p_H, evaluated in Appendix 3-C [Eq. 3-C9]. It can in principle change the phase equilibrium on the aggregate surface if it becomes comparable with either osmotic pressure, $p_{osm} = n' k_B T$, of nanoparticles in the dilute phase (at their number density n') or with the capillary pressure $p_{cap} \approx \sigma_0 / b$ due to the aggregate surface tension σ_0. The capillary pressure is found to dominate over the osmotic one, and the characteristic ratio of hydrodynamic-to-capillary pressures reads:

$$\frac{p_H}{p_{cap}} \sim \frac{\eta_0 \omega r_a b}{\sigma_0 \left(\ln(2r_a) - 1/2\right)} \sim \frac{\eta \omega L_{max}}{\sigma_0 \left(2 \ln(2r_{max}) - 1\right)}. \qquad (3.38)$$

Taking $\eta_0 \approx 10^{-3}$ Pa × s for water, $\sigma_0 \approx 1.5 \times 10^{-4}$ N/m [Appendix 3-B] and experimental values of L_{max} and r_{max} for each angular frequency ω, we evaluate $p_H / p_{cap} \lesssim 7.5 \times 10^{-3}$ in the frequency range, $5 \leq \nu \leq 25$ Hz, with, of course $p_H / p_{cap} = 0$ in the permanent field ($\nu = 0$). Thus, the hydrodynamic pressure is negligible regarding the capillary one and is not expected to affect the phase equilibrium. Finally, the aggregate half-thickness b is found to be nearly constant with the frequency, such that the capillary pressure is expected to be roughly independent of ω and likely cannot change phase equilibrium at different frequencies. In summary, we have eliminated possible effects of demagnetizing field, hydrodynamic and capillary pressures on the change of the phase separation threshold with the frequency ω of aggregate rotation, in agreement with experiments.

3.3.2 Minimal and maximal aggregate size

Above the phase separation threshold, once the magnetic field is applied, the micron-sized needle-like aggregates appear on a timescale of ~1 s, much shorter than the timescale of the whole phase separation process (~10^2 s). This initial fast kinetics is attributed to the fast nucleation stage that is not accessible in our experiments. One can consider that the aggregate growth/coalescence stages start with some initial (minimal) average aggregate size corresponding (at the first approximation) to the average size of critical nuclei, evaluated in Sec. 3.2.2. Experimentally, the minimal aggregate size can be found from extrapolation of the experimental aggregate length versus time curves (as shown below on Fig. 3.5) to the ordinate axis. In experiments, we get $L_{min} = 17 \pm 5$ μm – a value that compares relatively well with the theoretical evaluation by [Eqs. (3.6a), (3.6b)], $L_{min} = L_c \approx 12$ μm, obtained at the considered parameters $\varphi_0 = 1.6 \times 10^{-3}$ (initial nanoparticle volume fraction), $\Delta_0 = 9 \times 10^{-4}$ (initial supersaturation – cf. Sec. 3.3.1), $H_0 = 9$ kA/m (magnetic field amplitude) and $\langle d_m^9 \rangle = (13.6\ \text{nm})^9$ (the 9th moment of the size distribution of individual nanoparticles – cf. Eq. (2.2)). Notice that the size d_m of individual nanoparticles (revealed from magnetization measurements – Sec. 2.1.2) seems to be more relevant for the evaluation of the work of nucleus formation (and consequently critical nuclei size) than the hydrodynamic size d_p revealed by DLS. Within experimental errors, experimental values of L_{min} appear to be independent of the field frequency within the range $0 \le \nu \le 25$ Hz, in agreement with the fact that the phase equilibrium on the aggregate (nucleus) surface is almost non-affected by the aggregate rotation, as discussed in detail in Sec. 3.3.1. Notice that, as in the case of the phase separation threshold, gravitational settling in the permanent magnetic field ($\nu = 0$) is slow enough concerning the nucleation stage and still allows experimental determination of the minimal aggregate size.

At long times ($t \gtrsim 200$ s), the aggregate size is limited by fragmentation events coming from hydrodynamic interactions between aggregates. The experimental dependency of the maximal average aggregate length L_{max} on the field frequency, ν is shown in Fig. 3.4 for the considered parameters $\varphi_0 = 1.6 \times 10^{-3}$ and $H_0 = 9$ kA/m. The experimental data have been fitted by Eqs. (3.8), (3.9a) with the adjustable parameter value of the lateral gap between aggregates set to $h_0 = 60$ nm, thus being equal to about three nanoparticle hydrodynamic diameters $\langle d_p \rangle \approx 21$ nm [Fig. 2.1], which is consistent with the proposed model [Sec. 3.2.3].

The following values of other parameters were used in calculations: $\eta_0 \approx 10^{-3}$ Pa × s, $b \approx 2.5$ μm [Appendix 3-B], $\chi \approx 22 \pm 5$ [Appendix 3-A]. The result of the fit is presented by

a solid curve in Fig. 3.4. Both the theory and the experiments show a relatively strong decrease in L_{max} with ν that is explained by the fact that two colliding aggregates can transiently coalesce and then split into several parts due to surface instabilities whose probability increases with the increasing relative speed of collision (cf. details of this possible scenario in Sec. 3.2.3). This phenomenon is typically observed in experiments. Two long colliding aggregates seem to merge for a short time and fragment into three-to-four parts[6]. Short timescale dynamics of fragmentation are inaccessible for our slow-speed recording equipment and are out of the scope of our study. The most important parameter stemming from this dynamics is the maximal aggregate size. Our simple energy balance approach developed in Sec. 3.2.3 allows a semiquantitative agreement with experiments on the maximal aggregate length, as seen in Fig. 3.4, without the need for a detailed study of fragmentation that can be envisaged in future. Quantitatively, the maximal average aggregate length varies in the range of 30-80 μm in the considered frequency range, while the aggregate thickness remains almost constant and approximately equal to 5 μm. The aggregate thickness will be discussed in more detail in the next Sec. 3.3.3.

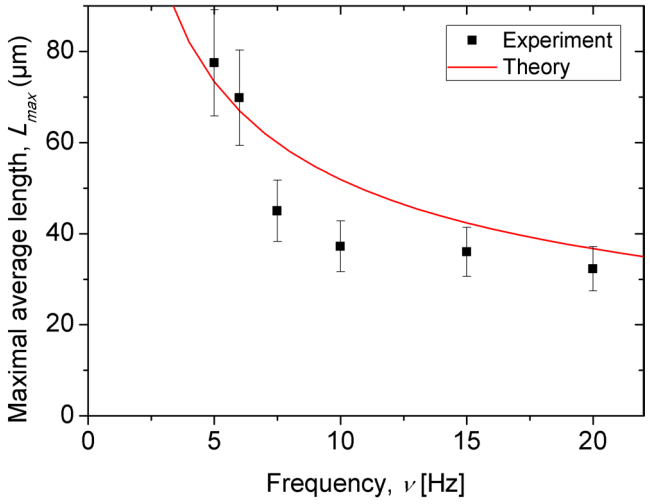

Figure 3.4: The experimental and theoretical dependency of the maximal average aggregate length on the field frequency. The value of the adjustable parameter for the theoretical dependency [Eqs. (3.8), (3.9a)] is set to $h_0 =$ 60 nm.

Finally, a few supplementary measurements at different channel depths show that the aggregate average maximal length [Fig. 3.4] and the phase diagram [Fig. 3.3] remain independent of the channel depth in the studied range of $50 \leq h \leq 200$ μm.

[6] see video-b.mp4 file in Supplemental Materials of the paper [Raboisson-Michel al. J. Chem. Phys. 153(15), 154902 (2020)]

3.3.3 Integral characteristics

Once the lower and upper limits for the aggregate size are found, we can inspect in detail the size evolution with time. The experimental dependencies of the average aggregate length $\langle L \rangle$ on elapsed time t are shown in Fig. 3.5a for the field frequency $\nu = 5$ Hz and five different experimental runs. The inset presents the data at an increased time scale. This graph shows a relatively large dispersion of data between different experiments at identical parameters, which is probably related to limited colloidal stability of the diluted magnetic colloid after salt/acid treatment and surface impurities of the microfluidic channel caused by imperfect washing of the channel between different runs. Despite such imperfect reproducibility, we have secured our data by error bars arising from standard deviation on five experimental sets for each frequency.

The experimental and theoretical $\langle L \rangle(t)$ dependencies obtained as an average on five identical measurements are shown in Fig. 3.5b for $\varphi_0 = 1.6 \times 10^{-3}$ and $H_0 = 9$ kA/m and at different magnetic field frequencies ν. Notice that in the case of the permanent magnetic field ($\nu = 0$), the gravitational settling of aggregates does not allow obtaining reliable data at times $t \gtrsim 60$ s because the settled aggregates are immobilized at the channel bottom and their further growth seems to be stopped after settling. For this reason, the average aggregate length in the permanent field (crossed black triangles in Fig. 3.5b) appears to be smaller than that in the rotating field at $\nu = 5$ Hz. We would expect an opposite tendency if the gravitational settling were absent in the permanent field. Thus, the data of Fig. 3.5b at $\nu = 0$ should be handled with care. The theoretical curves at $\nu = 10, 15$ and 20 Hz are close to each other and only the theoretical curve for $\nu = 15$ Hz is shown in Fig. 3.5b.

The theoretical dependencies (solid lines) are calculated for the rotating field in a parametric form by varying the Θ parameter, respecting the following steps: (a) the average dimensionless volume $\langle v \rangle(\Theta)$ and time $\tau(\Theta)$ are evaluated using Eqs. (3.27c), (3.28); (b) the dimensional time is evaluated as $t = t_d \tau$ with the diffusion timescale t_d given by Eq. (3.23); (c) at approximately constant aggregate semi-thickness $b \approx const$, the equality $\langle v \rangle = \langle V \rangle / V_{max} \approx \langle L \rangle / L_{max}$ allows us to evaluate the average aggregate length as $\langle L \rangle \approx L_{max} \langle v \rangle$. The following values of the physical parameters intervening in different calculation steps were used: the depth of the microfluidic channel $h = 200$ μm; the average nanoparticle diameter $d_p = 21$ nm was taken from the primary peak of the hydrodynamic size distribution [Fig. 2.1] – a value more relevant for the evaluation of nanoparticle Brownian diffusivity and diffusion

timescale [Eq. (3.23)] than the size of metal oxide cores of individual nanoparticles; the initial supersaturation $\Delta_0 = 9 \times 10^{-4}$ found from the experimental phase diagram [Sec. 3.3.1, Fig. 3.3]; initial volume fraction of aggregates in the colloid $\Phi_0 = 3 \times 10^{-5}$ found from experimental snapshots at elapsed time $t = 1$ s by image processing; the aggregate half-thickness $b \approx 2.5$ μm [Appendix 3-B], magnetic susceptibility $\chi \approx 22 \pm 5$ and internal volume fraction $\varphi'' = 0.32 \pm 0.03$ [Appendix 3-A]; the minimal average aggregate length $L_{min} = L_c \approx 12$ nm corresponding to the critical nuclei size evaluated in Sec. 3.3.2; the maximal average aggregate length L_{max} can in principle be evaluated theoretically by Eqs. (3.8), (3.9a) but to provide better correspondence with experiments, we take experimental values of L_{max}, shown by points in Fig. 3.4; finally, the initial average dimensional volume is evaluated as $v_0 = V_c/V_{max} \approx L_c/L_{max}$.

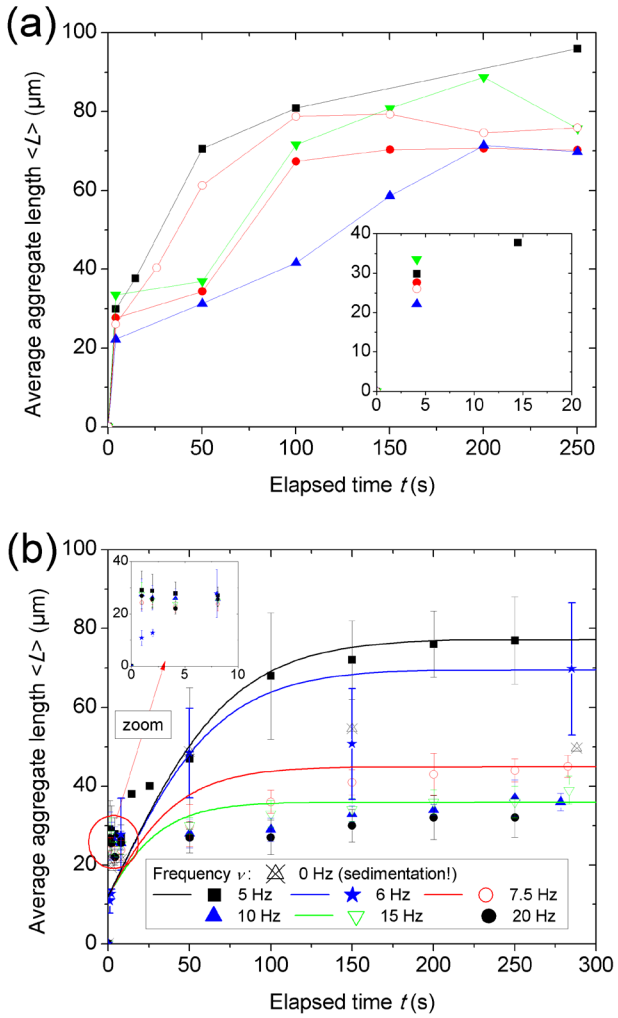

Figure 3.5: The experimental time dependencies of the average aggregate length for five independent measurements at the frequency $\nu = 5$ Hz (a). The lines in (a) are guides for the eye. The experimental and theoretical time dependencies of the average aggregate length (b), each experimental curve being a medium of five independent measurements and error bars calculated as standard deviation. The points in (b) correspond to experiments and solid lines – to the theory. The insets in (a) and (b) present the data at an increased time scale.

As is seen in Fig. 3.5b, the average aggregate length progressively increases with the elapsed time from the minimal value $L_{min} = 17 \pm 5$ μm and achieves a plateau at long times $t \gtrsim 200$ s. The value L_{max} at the plateau decreases with increasing frequency in agreement with Fig. 3.4. This plateau is ascribed to the equilibrium between the aggregate fragmentation rate and the effective aggregate growth rate including coalescence and absorption of nanoparticles by aggregates between coalescence events. This balance is believed to lead to saturation of the aggregate size. Our model seems to fit relatively well with the experimental data, except for short times $t \lesssim 25$ s where experiments predict a faster increase of the aggregate size with time, as shown on the inset of Fig. 3.5b. This disagreement likely comes from approximations of the aggregate growth rate $\dot{V} \propto (1 - \langle v \rangle)$ [Eq. (3.19)] and coalescence constant $K = K_0(1 - \langle v \rangle)$ [Eq. (3.21)], introduced to cancel the aggregate growth at $\langle v \rangle \to 1$ or $\langle V \rangle \to V_{max}$ without introducing fragmentation terms into the population balance equation [Eq. (3.2)]. In reality, this approximation is expected to underestimate the quantities $\dot{V}$ and K at short times (well before the fragmentation starts), thus, predicting slower aggregate growth than that observed in experiments. Despite this disagreement at short times our model for integral characteristics has the advantage to be free of any adjustable parameter; all physical quantities have been evaluated either experimentally or theoretically as specified above.

Recall that our model involves both aggregate growth (by convective diffusion of nanoparticles) and aggregate coalescence mechanisms through the population balance equation [Eqs. (3.2) and (3.25)]. The key parameter describing the transition between both mechanisms is the ratio of diffusion-to coalescence timescales, $\kappa_0 = t_d/t_c$, whose value varies in the range 1.3-3.5 within the experimental frequency range $5 \leq \nu \leq 25$ Hz. This indicates that both mechanisms appear at quite similar timescales, $t_d \sim t_c \sim 15 - 60\ s$ in a rotating magnetic field, with coalescence being even somewhat faster than aggregate growth, as opposed to what is observed in the permanent magnetic field [Ezzaier et al. (2017)]. Faster coalescence in the rotating field could come from larger average dipolar interaction between rotating aggregates, as compared to non-rotating aggregates in the permanent magnetic field. The analysis shows, that in the point dipole approach, the ratio of the coalescence constants in rotating and permanent fields scales as $K_0^{rot}/K_0^{perm} \sim (h/b)^{5/2} r_a^{-3/2} \sim 10^3$ in agreement with faster coalescence in rotating fields.

Another important parameter is the constant $\beta = 1/(1 + \alpha) = 1/(1 + 8(\ln(2r_{max}) - 1/2)^{1/3} Pe_{max}^{-1/3}/k)$ [cf. Eq. (3.17b)] governing the physics of the aggregate growth, with $k \approx$

1.931. As follows from the analysis of Sec. 3.2.4, the values $\beta \approx 1$ correspond to the dominant diffusive transport of nanoparticles towards the cavity swept by the aggregate rotation, for which the aggregate growth timescale is given by the diffusion time t_d [Eq. (3.23)]. On the opposite limit, $\beta \approx 1/\alpha = kPe_{max}^{1/3}/(8(\ln(2r_{max}) - 1/2)^{1/3}) \ll 1$ with still high Péclet numbers $Pe_{max} \gg 1$, the particle transport towards the aggregates is dominated by the convective diffusion through a thin diffusive boundary layer, and the characteristic aggregate growth timescale becomes $t_{conv} = t_d/\beta \approx 8(\ln(2r_{max}) - 1/2)^{1/3} Pe_{max}^{-1/3} t_d/k$ and decreases with the field frequency as $t_{conv} \propto \omega^{-1/3}$. In our experimental case, the constant β varies in a narrow range $\beta = 0.53 - 0.62$ at the frequencies $5 \leq \nu \leq 25$ Hz indicating that both mechanisms of the aggregate growth are comparable and cannot be considered separately.

Regarding the aggregate thickness, $2b$, experiments show that, within the experimental errors, it depends on neither the aggregate volume V, nor aspect ratio r_a, nor magnetic field frequency and is equal to $2b \approx 5$ μm, in quantitative agreement with the evaluation conducted in Appendix 3-B. This result is in stark disagreement with previous theoretical models [Zubarev and Ivanov (1997); Ezzaier et al. (2017)] predicting $2b \propto V^{2/7} \propto r_a^2$. The difference arises in the details of energy minimization. In the present model, we take into account possible variation of the surface energy with the aggregate magnetization, which allows better agreement with experiments on the aggregate shape and shows that the aggregate thickness behaviour varies from $2b \approx const$ at $12\chi \gg r_a^2 \gg 1$ to the conventional behaviour $2b \propto V^{2/7} \propto r_a^2$ at $r_a^2 \gg 12\chi \gg 1$ [see Appendix 3-B].

To further inspect predictions of our model, the experimental and theoretical time dependencies of ratios $\Phi(t)/\Phi_0$ and $n(t)/n_0$ of volume fractions and number densities of aggregates are shown in Fig. 3.6 for the magnetic field frequency $\nu = 7.5$ Hz and at $\varphi_0 = 1.6 \times 10^{-3}$ and $H_0 = 9$ kA/m. These dependencies have a similar shape at other frequencies. The experimental dependencies were obtained by averaging over five identical measurements and the error bars correspond to the standard deviation evaluated on the set of five measurements. Theoretical dependencies were calculated in parametric form using Eqs. (3.27a), (3.27b) and (3.28), using the same set of physical parameters as for the evaluation of the aggregate average length. Both the experiments and the model show: (a) an increase in the volume fraction of aggregates $\Phi(t)$ with time corresponding to the aggregate growth by absorption of nanoparticles from the dilute phase; and (b) a decrease in the aggregate number density $n(t)$ with time pointing out to coalescence of aggregates. The variation of both

magnitudes occurs on the same timescale, t~60 s, followed by saturation at longer times. This saturation corresponds to the limitation of the aggregate size to its maximal average value through fragmentation events. Our model predicts the following expressions for the plateau values of $n(t\to\infty)/n_0 = n_{min}/n_0$ and $\Phi(t\to\infty)/\Phi_0 = \Phi_{max}/\Phi_0$ obtained from Eqs. (3.27a), (3.27b):

$$\frac{n_{min}}{n_0} = \left[1 + \frac{\kappa_0 \Theta_{max}}{2v_0}\right]^{-1}, \qquad \frac{\Phi_{max}}{\Phi_0} = e^{\beta\Theta_{max}}, \tag{3.39}$$

where Θ_{max} is found from the solution of the transcendental equation (3.29).

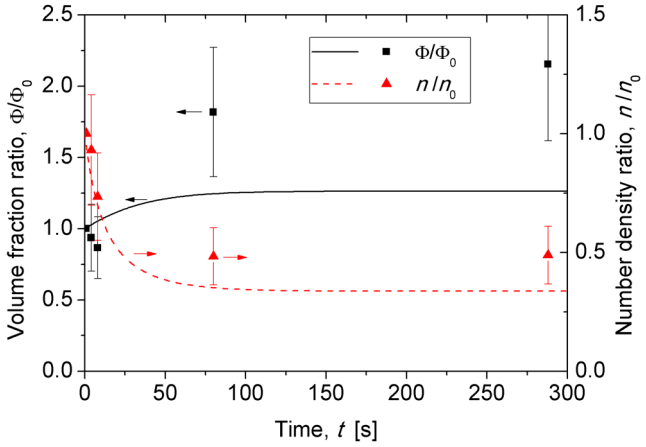

Figure 3.6: Theoretical and experimental time dependencies of the ratios $\Phi(t)/\Phi_0$ (left ordinate axis) and $n(t)/n_0$ (right ordinate axis) of volume fractions and number densities of aggregates at the field frequency $\nu = 7.5\ Hz$. Symbols correspond to experiments and solid lines – to the theory.

Quantitatively, our model predicts a more important variation of the aggregate number density $n(t)$ and a weaker variation of the volume fraction of aggregates $\Phi(t)$ than those observed in experiments, even though large experimental errors could partially cover this difference. The discrepancy likely comes from the approximations $\dot{V} \propto (1 - \langle v\rangle)$ [Eq. (3.19)] and $K = K_0(1 - \langle v\rangle)$ [Eq. (3.21)] which probably underpredicts the plateau values of Φ_{max} and n_{min} given by Eq. (3.39). It is worth noticing that experimental ($\Phi_{max} \approx 6.6\times10^{-5}$) and theoretical ($\Phi_{max} \approx 3.8\times10^{-5}$) values of the maximal concentration are two orders of magnitude smaller than the value $\Phi_{max} = \Delta_0/\varphi'' \approx 3\times10^{-3}$ corresponding to the thermodynamic equilibrium between dilute and concentrated phases. This conclusion holds within the whole experimental frequency range of $5 \le \nu \le 25$ Hz and clearly shows that the phase separation stops well before achieving thermodynamic equilibrium because of hydrodynamics interactions leading to fragmentation of aggregates. Our model qualitatively captures this physics and predicts a correct order of magnitude of the plateau values Φ_{max}/Φ_0 and n_{min}/n_0.

3.3.4 Size distribution

Once the integral characteristics of the phase separation are analysed, we can proceed with the aggregate size distribution. Experimental and theoretical distribution functions $f(v)$ of the dimensionless volume v are plotted in Figs. 3.7a-d for different moments of time t, at the field frequency $\nu = 5$ Hz and at $\varphi_0 = 1.6 \times 10^{-3}$ and $H_0 = 9$ kA/m. These dependencies have a similar shape to other frequencies. Experimental dependencies were constructed by the image processing procedure [Sec. 2.5.1] and the data in Fig. 3.7 present the average over five independent measurements with the error bars standing for standard deviation over the set of these five measurements. Notice that the measured length distribution $f(L/L_{max})$ is equivalent to the distribution $f(v)$ over dimensionless volumes presented in Fig. 3.7, provided that $v = V/V_{max} \approx L/L_{max}$ at nearly constant aggregate thickness $2b \approx const$ [see Sec. 3.3.3, Appendix 3-B].

Experiments reveal a relatively narrow but finite-width size distribution of aggregates at the elapsed time $t = 1$ s [Fig. 3.7a]. This aggregate size distribution is characterized by a similar dimensionless average volume, $\langle v \rangle \approx v_0$ as one of the critical nuclei $v_0 \approx L_{min}/L_{max} \approx 0.16$ with the critical nuclei length $L_{min} = L_c \approx 12$ μm evaluated in Sec. 3.3.2. This allows us to suppose that the aggregate size distribution at short timescales, $t \sim 1$ s, corresponds to the size distribution of the critical nuclei at the end of the fast heterogeneous nucleation stage. This initial size distribution likely arises as a result of a polydispersity of the condensation centres (primary agglomerates ascribed to the secondary peak of the hydrodynamic size distribution [Fig. 2.1]) combined with complex kinetics of nucleation. As already mentioned, we do not have experimental access to the fast nucleation stage and its precise modelling is out of the scope of the present paper. Thus, the initial size distribution of aggregates at short times, $t = 1$ s, is fitted to the empirical function $f_0(v)$ [Eq. (3.36)] with $v_0 \approx 0.16$ and the parameter m describing the distribution width is set to $m = 6$. The fit is presented by a solid curve in Fig. 3.7a. This empirical initial size distribution $f_0(v)$ is then used to calculate the theoretical aggregate size distribution $f(v)$ at different moments of time $t > 1$ s using Eq. (3.37). The theoretical size distributions at $t = 8,\ 80$ and 288 s are presented by solid curves in Figs. 3.7b, c and d. Evaluations of $f(v)$ by a long-time/large volume limit [Eq. (3.35)] are added as dashed curves for the sake of comparison. All the calculations have been done for the same set of physical parameters used for evaluations of the integral characteristics [Sec. 3.3.3]. To get the distribution function at a fixed elapsed time, $t = t_d\tau$, we first evaluate the reduced time Θ corresponding to the desired value of t and then evaluate $f(v, \Theta)$ using Eq. (3.35) or Eq. (3.37).

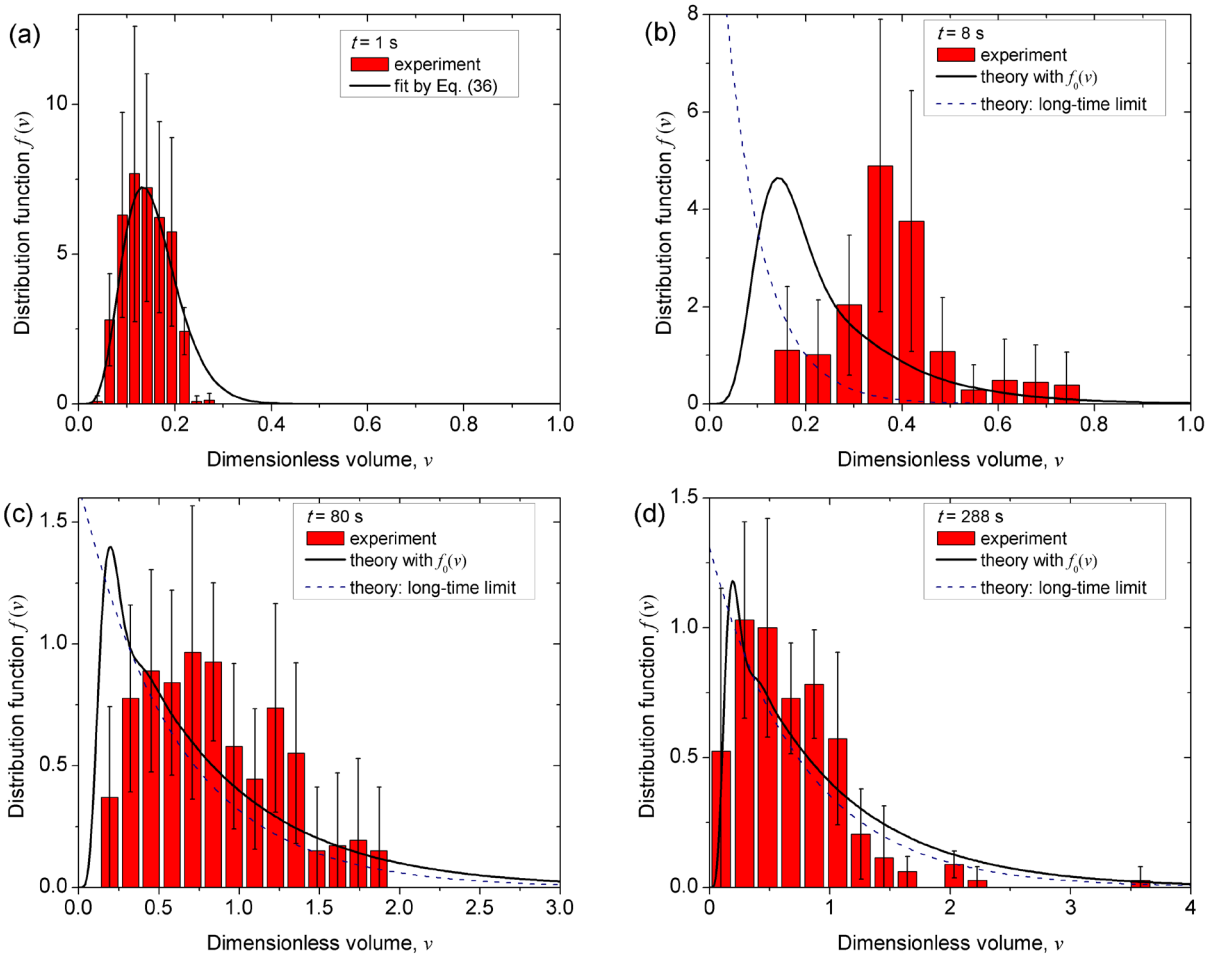

Figure 3.7: Experimental and theoretical distribution of the aggregate dimensionless volumes for the frequency $\nu = 5\ Hz$ and at different elapsed times: $t = 1\ s$ (a); 8 s (b); 80 s (c) and 288 s (d). The column-like histogram corresponds to experimental data obtained by averaging over five individual measurements. The solid curve in (a) corresponds to the fit of the experimental size distribution $f_0(v)$ by Eq. (3.36) at a short time $t = 1\ s$. The curves in (b), (c), and (d) stand for predictions of the model taking into account the initial size distribution $f_0(v)$ [solid curves, Eq. (3.37)] and the model in a long time/large volume limit [dashed curves, Eq. (3.35)].

Figures 3.7b-d show that the experimental size distribution spreads over the volume axis during the time. Such a spread is qualitatively reproduced by our model and is mostly related to the coalescence of unequal-sized aggregates broadening the size population, as typically observed in the classical Smoluchowski limit [Aldous (1999)]. However, the model does not capture the significant shift of the distribution peak to larger volumes, especially at $t = 8$ s, even though the average dimensionless volumes $\langle v \rangle$ given by experimental and theoretical distributions are quite similar, as inferred from Fig. 3.5b. Such a shift is typically reproduced by the model considering only the aggregate growth mechanism ignoring the coalescence[7]. This allows us to suppose that the relative contribution of coalescence in the present model is overestimated especially at short times, possibly due to approximations $\dot{V} \propto (1 - \langle v \rangle)$ [Eq.

[7] Details of this model are presented in the auxiliary paper of the present work [Kuzhir et al. Math. Meth. Appl. Sci. 44(16), 12088-12100 (2021)]

(3.19)] and $K = K_0(1 - \langle v \rangle)$ [Eq. (3.21)]. However, at the present set of physical parameters, the coalescence-free approximation gives an extremely sharp and narrow size distribution not reproducing all the present experimental data. It is worth noticing that the long time/large volume limit [Eq. (3.35)], conventionally used in coagulation problems [Levič (1962); Aldous (1999)], provides predictions close to the exact calculation by Eq. (3.37) at times $t \geq 80$ s [Figs. 3.7c, d], except for small dimensionless volumes, $v \lesssim 0.5$, being unable to reproduce the initial increase of the distribution function. Recall that, in a long time/large volume limit, the aggregate size distribution no longer depends on neither the shape nor the average volume v_0 of the initial size distribution, which is a pertinent feature of the considered coagulation-condensation process. However, in our particular case, the long-time limit is strictly speaking not achieved even at infinite times. This is because this limit has been formulated for the compressed dimensionless timescale, Θ, achieving finite values $\Theta_{max} \approx 0.3 - 0.8$ at $t \to \infty$, such that $\kappa_0 \Theta/(2v_0) \approx 1.4 - 3.4$ violating the "long time" condition, $\kappa_0 \Theta/(2v_0) \gg 1$. This is the reason for which the exact agreement between the exact calculations [Eq. (3.37)] and the long-time limit [Eq. (3.35)] is never observed at infinite times, even though the difference is relatively small. Physically, the compressed timescale Θ allows a limitation of the size of rotating aggregates at $t \to \infty$ (introduced through approximations $\dot{V} \propto (1 - \langle v \rangle)$ and $K = K_0(1 - \langle v \rangle)$), unlike the case of classical irreversible coagulation [Levič (1962); Aldous (1999)] or condensation-driven coagulation [Hassan and Hassan (2008)] when the aggregates grow indefinitely within the limits dictated by material balance. In our case, the final aggregate size distribution at $t \to \infty$ can be evaluated by Eq. (3.35) or Eq. (3.37) upon setting $\Theta = \Theta_{max}$, with Θ_{max} found from the solution of the transcendental equation (3.29).

3.4 Conclusions

This Chapter reports experimental and theoretical studies of the phase separation of a colloidal suspension of magnetic nanoparticles (IONP) under a circularly polarized rotating magnetic field in the frequency range $5 \leq \nu \leq 25$ Hz allowing synchronous rotation of field-induced aggregates. In experiments, we use dilute aqueous suspensions of citrate-coated iron oxide nanoparticles slightly destabilized by increasing ionic strength and decreasing the suspension pH, which allows the appearance of primary agglomerates of typical hydrodynamic size ~150 nm. They are expected to play the role of condensation centres for fast heterogeneous nucleation of nanoparticles in the presence of external magnetic fields. Beyond the first nucleation stage, occurring at a timescale less than 1 s, the experimental observations can be summarized as follows:

1. Like in a permanent magnetic field, the field-induced phase separation in the rotating field is manifested through the appearance of needle-like dense particle aggregates whose size progressively increases with time via aggregate growth and coalescence mechanisms. Two fundamental differences are that the aggregate growth could be enhanced through the convection of nanoparticles relatively to rotating aggregates, and the maximal aggregate size is limited by the fragmentation arising as a result of their hydrodynamic interactions/collisions.
2. The average aggregate length evolves between the lower limit probably dictated by the critical nuclei size and the upper limit dictated by the collision-induced fragmentation. The critical nuclei size and the aggregation threshold $H(\varphi')$ appear to be nearly independent of the rotational frequency of aggregates, $5 \leq \nu \leq 25$ Hz. On the contrary, the maximal aggregate size decreases with the frequency approximately as $L_{max} \propto \nu^{-1/2}$. Most of the aggregates perform a collective rotation in the same horizontal plane between the lower and the upper bounding walls.
3. The aggregate growth and the coalescence occur at similar timescales, $t_d \sim t_c \sim 1$ min, weakly dependent on the field frequency within the considered range $5 \leq \nu \leq 25$ Hz. This implies that the aggregate concentration Φ in the suspension continuously grows with time and the aggregate number density n decreases with time, both showing a plateau at long times when the average size achieves its maximal value.
4. The experimental aggregate size distribution is found to significantly spread with time always keeping a non-negligible fraction of small aggregates, which is reminiscent of classical coagulation [Levič (1962); Aldous (1999)] or condensation-driven aggregation [Hassan and Hassan (2008)] processes. The fundamental difference is that in our case, we achieve a steady state with a finite size distribution, while classical coagulation leads to infinite aggregate growth.

The aforementioned experimental features are correctly reproduced by the developed theoretical models. In particular, the kinetics of aggregation beyond the nucleation stage is described by the population balance equation (3.2), simultaneously including the aggregate growth and coalescence mechanisms, while the critical nuclei size is used as the initial condition. The aggregate growth rate $\dot{V}$ is evaluated through the cavity model coupled with a diffusive boundary layer approach. The coalescence kernel is evaluated through the cell model, and the constant kernel approximation, $K(V, V') \approx const = K_0$ is shown to approximately hold for our experimental conditions. The aggregate fragmentation is implicitly taken into account by allowing the aggregate growth rate and the coalescence constant decrease with increasing

average volume as $\dot{V} \propto (1 - \langle v \rangle)$ and $K = K_0(1 - \langle v \rangle)$. All these approximations along with the linearization of the aggregate growth rate, $\dot{V} \propto V$, allow the analytical solution of the population balance equation, which gives satisfactory quantitative agreement with experiments on the average aggregate length $\langle L \rangle$ without any adjustable parameter and qualitatively reproduces the shape and the time behaviour of the experimental length distribution function. Qualitatively, the frequency of the magnetic field affects the phase separation through (a) the maximal aggregate size $L_{max} \propto \nu^{-1/2}$ (also confirmed by our theory) and (b) the convection-diffusion timescale $t_{conv} = t_d(1 + 8(\ln(2r_{max}) - 1/2)^{1/3} Pe_{max}^{-1/3}/k)$ depending on the Péclet number, $Pe_{max} \propto \nu$. The effect (b) appears to be small in the considered frequency range.

From the practical perspective, we show that the timescale of the field-induced self-assembly is about 1 min, as can be inferred from Fig. 3.5. This timescale is much smaller than the duration of the medical intervention, evaluated to be a minimum of 30 min for the blood clot lysis application using this novel technology, briefly introduced in Preface and Sec. 1.1.3. This gives us a hope that after their rapid formation, the aggregates will be able to generate the recirculation flow and enhance the drug transport to the blood clot through a blocked vessel. These points are checked in the subsequent Chapters on the example of aqueous magnetic colloids and alginate beads. At this point, it is worth noticing that the formation of field-induced aggregates is completely reversible depending on the presence of the field. This decreases the risk of blood vessel blockage by micron-sized aggregates which are easily dissociated into individual nanoparticles (or their nanosized primary agglomerates) either upon turning off the field or through hydrodynamic rupture forces destroying the aggregates when they are blocking a flow through the blood vessels.

3.5 Appendixes

Appendix 3-A. Aggregate magnetic susceptibility χ and internal volume fraction φ''

Semi-empirical evaluation of the magnitudes χ and φ'' is performed by measuring the velocity of the aggregate migration under a magnetic field gradient and fitting it to a theoretical relationship developed below. These experiments are impossible in permanent magnetic fields because of the gravitational settling of aggregates. However, in rotating fields, settling has never been observed (very likely due to hydrodynamic interactions with walls), and this allows evaluation of χ and φ'' in the conditions close to those realized in phase separation experiments. To realize a circularly polarized rotating magnetic field with a non-zero gradient, we used the 3-coil configuration shown in Fig. 2.4 and explained in Sec. 2.3.1. The amplitude and the

frequency of the field in the vicinity of the geometric centre of the system were adjusted to $H_0 = 9$ kA/m and $\nu = 5$ Hz. As mentioned in Sec. 2.3.1, the three-coil configuration allowed obtaining the magnetic force on superparamagnetic aggregates with the dominant component $F_{m,y}$ oriented along the y-axis of symmetry of the internal coils.

The microfluidic channel was placed in the centre of the system and oriented along the y-axis. The channel was filled with a dilute magnetic colloid subjected to salt/acid treatment at a nanoparticle volume fraction $\varphi_0 = 1.6 \times 10^{-3}$. The applied rotating field made the aggregates rotate synchronously with the field and migrate along the y-axis. We have not observed any substantial deviation in the trajectory of the aggregate centres from the y direction. The aggregate motion was recorded by the CMOS camera and the linear velocity v_y of their centres was measured using the Fiji image calculator using a procedure close to that described in Sec. 2.5.3. For data treatment, we have chosen a series of ten aggregates respecting the following criteria: (a) large enough to avoid visible aggregate growth for the time-lapse necessary for the velocity determination; (b) situated far enough from other aggregates and lateral walls to minimize possible hydrodynamic interactions. Let us now relate the measured aggregate velocity v_y to its magnetic susceptibility χ under the assumption of linear magnetization reasonable for relatively small applied magnetic field $H_0 = 9$ kA/m.

Since the aggregates are mostly symmetrical bodies (having a needle-like shape), their rotational and translational motion is uncoupled [Happel and Brenner (1983)]. As in the kinetic model, the aggregate shape is supposed to be a prolate ellipsoid with the major and minor semi-axes a and b and the aspect ratio $r_a = a/b$. It is also shown that in experimental conditions the phase lag between the orientations of aggregate and field is negligible, so the aggregates are supposed to be always aligned with the instantaneous direction of the field. On average (over the rotation period), the aggregates do not move across the channel, while the instantaneous velocity along the channel (y axis) is

$$v_y(\theta) = \tilde{b}_{yy} F_{m,y} = \left(\tilde{b}_{\parallel} \cos\theta + \tilde{b}_{\perp} \sin\theta\right) \frac{1}{2} \mu_0 \frac{\chi}{1+N\chi} \frac{\partial H_{0y}^2}{\partial y} V \cos^2\theta \,, \tag{3-A1a}$$

$$N = \frac{1}{2r_a^2 (1-r_a^{-2})^{3/2}} \left[\ln \frac{1+(1-r_a^{-2})^{1/2}}{1-(1-r_a^{-2})^{1/2}} - 2(1-r_a^{-2})^{1/2} \right], \tag{3-A1b}$$

$$\tilde{b}_{\parallel} = \frac{1}{\eta_0 f_{\parallel} a},\ \tilde{b}_{\perp} = \frac{1}{\eta_0 f_{\perp} a},\ f_{\parallel} = \frac{16\pi}{r_a^2 (2\beta' + \alpha_{\parallel})},\ f_{\perp} = \frac{16\pi}{2r_a^2 \beta' + \alpha_{\perp}},\ \alpha_{\parallel} = \frac{2(\beta' r_a^2 - 1)}{r_a^2 - 1},\ \alpha_{\perp} = \frac{r_a^2 (1-\beta')}{r_a^2 - 1},\ \beta' = \frac{\operatorname{acosh} r_a}{r_a (r_a^2 - 1)^{1/2}} \tag{3-A1c}$$

where H_{0y} is the y-component amplitude of the oscillating magnetic field generated by the single connected internal coil; N is the aggregate demagnetization factor [Landau and Lifshitz (1980)], $\theta = \omega t$ is the angle between the aggregate and the y axis at a given moment of time t, $\tilde{b}_{yy}$ is the diagonal component of the aggregate mobility tensor along the y axis of the channel, and $\tilde{b}_{\parallel}, \tilde{b}_{\perp}$ - the components parallel to the major and minor aggregate axes, respectively [Brenner (1974)]; other physical quantities are defined in the main text of the Chapter. Assuming homogeneous aggregate rotation, the y-component of the aggregate speed averaged over the rotation period (after some transformations) reads:

$$\langle v_y \rangle = \frac{1}{2\pi}\int_0^{2\pi} v_y(\theta)d\theta = \frac{\pi}{48}\mu_0 \frac{\chi}{1+N\chi}\frac{\partial H_{0y}^2}{\partial y}\frac{(2b)^2}{\eta_0}\left(\frac{3}{f_{\parallel}}+\frac{1}{f_{\perp}}\right), \qquad \text{(3-A2)}$$

where the coefficients N, $f_{\parallel}$ and $f_{\perp}$ are related to the aggregate aspect ratio r_a by Eqs. (3-A1b), (3-A1c). The aggregate thickness $2b$ and aspect ratio r_a are determined by direct size measurement on each aggregate, the value $\partial H_{0y}^2/\partial y \approx 1.5 \times 10^9$ A^2/m^3 is found by magnetic field measurements coupled with the simulation of the field distribution, and $\eta_0 \approx 10^{-3}$ Pa×s is the suspending liquid (water) viscosity.

The aggregate magnetic susceptibility χ is determined by fitting experimental values of $\langle v_y \rangle$ to Eq. (3-A2). For the series of ten measurements, we get $\chi = 22 \pm 5$. This value is consistent with the one $\chi \approx 24$ evaluated experimentally by Bacri et al. (1994) in experiments with elongation of the magnetic droplet.

The nanoparticle volume fraction φ'' inside the aggregates can be retrieved from the χ value using some statistical mechanics model of the ferrofluid microstructure. First, we presume that when the primary agglomerates (~20-100 nm, cf. Fig. 2.1) form bulk needle-like aggregates under an applied magnetic field, the individual nanoparticles (~8 nm) reorganize inside these bulk aggregates and form a dense phase but not compulsorily a close packing. Second, individual nanoparticles have a relatively narrow size distribution, as revealed by magnetization measurements. At these two conditions, a modified MMF2 model of Szalai et al. (2015), developed for concentrated (up to 40%vol) monodisperse colloid seems to be an adequate candidature for our case. According to this model, the aggregate magnetic susceptibility is

$$\chi = \chi_L\left[1+\frac{1}{3}\chi_L+\frac{1}{144}\chi_L^2 f_L(\varphi'')\right], \chi_L = 8\varphi''\lambda_d, \quad \lambda_d = \frac{\pi\mu_0 M_S^2}{144k_BT}\frac{\langle d_m^6\rangle}{\langle d_m^3\rangle}, \qquad \text{(3-A3)}$$

$f_L(\varphi'') = 17\frac{1-0.93952\rho+0.36714\rho^2}{1-0.92398\rho+0.23323\rho^2} - 16$, $\rho = \frac{6\varphi''}{\pi}$.

Here, χ_L is the Langevin magnetic susceptibility (in the absence of interactions between particles), λ_d is the dipolar coupling parameter, $M_S \approx 3.1 \times 10^5$ A/m – saturation magnetization of nanoparticles, retrieved from magnetization measurements, $\langle d_m^3 \rangle$ and $\langle d_m^6 \rangle$ are the moments of the log-normal size distribution function [Eq. (2.1)], whose values are given below Eq. (2.2).

Solving the transcendental equation (3-A3) with respect to φ'', we get the following value of the nanoparticle volume fraction inside the aggregates: $\varphi'' = 0.32 \pm 0.03$. This value is consistent with the one ($\varphi'' \approx 0.3$) evaluated experimentally by Sandre et al. (1999). Notice that for the most precise evaluations of χ and φ'' we used exact expressions for the demagnetization factor [Eq. (3-A1b)] and hydrodynamic mobility [Eq. (3-A1c)] instead of approximate expressions at a high aspect ratio limit adopted in the kinetic model.

Appendix 3-B. Aggregate shape and surface tension

Our kinetic model requires explicit relationships between the aggregate aspect ratio, thickness, length, and volume. It is commonly admitted that these relationships come from the condition of the free energy minimum Blums et [al. (1996); Zubarev and Ivanov (1997)]; which applies even in rotating fields of relatively low frequency when the hydrodynamics modifies only slightly the local thermodynamic equilibrium of aggregates. As in the kinetic model, the aggregate shape is supposed to be a prolate ellipsoid with the major and minor semi-axes a and b and the aspect ratio $r_a = a/b$. Under considered linear magnetization approximation, the free energy for such aggregate reads:

$$\mathcal{F} = -\frac{1}{2}\mu_0 M_a H_0 V + \sigma S, \qquad \text{(3-B1a)}$$

$$M_a = \frac{\chi H_0}{1+N\chi}, \qquad \text{(3-B1b)}$$

$$S = V^{2/3} s, \quad s = 2\pi \left(\frac{3}{4\pi}\right)^{2/3} r_a^{-2/3} \left(1 + \frac{r_a \operatorname{asin}(1-r_a^{-2})^{1/2}}{(1-r_a^{-2})^{1/2}}\right), \qquad \text{(3-B1c)}$$

where σ and S are the aggregate surface tension and surface area, respectively; M_a and χ is the aggregate magnetization and magnetic susceptibility, respectively; the aggregate demagnetization factor N is given by Eq. (3-A1b) as a function of the aggregate aspect ratio r_a.

The surface tension σ is usually an unknown parameter, but it can be obtained by fitting the experimental aggregate shape to the modelled one. In our case where attractive van der Waals interaction between nanoparticles could play an important role, it is reasonable to suppose that the surface tension has one term depending on magnetization and the second constant term appearing due to non-magnetic colloidal interactions between nanoparticles:

$$\sigma = \sigma_0 + \mu_0 M_a^2 \delta, \tag{3-B2}$$

where δ is the characteristic thickness of the transition surface layer, which is typically on the order of the average size $\langle d_m \rangle$ of individual magnetic nanoparticles. The energy minimization with respect to the aggregate aspect ratio r_a at a fixed aggregate volume V and external magnetic field amplitude H_0 gives the following expression:

$$\left(\frac{\partial \mathcal{F}}{\partial r_a}\right)_{V,H_0=const} = \frac{1}{2}\mu_0 M_a^2 V \frac{dN}{dr_a} + \sigma V^{2/3}\frac{ds}{dr_a} - 2\mu_0 M_a^2 V^{\frac{2}{3}}\delta \frac{\chi}{1+N\chi}\frac{dN}{dr_a}s = 0, \tag{3-B3}$$

where the last term comes from the derivative of the surface tension [Eq. (3-B2)] (or rather its term depending on magnetization) with respect to the aspect ratio; this term is usually not considered in the models [Blums et al. (1996); Zubarev and Ivanov (1997)]. Solving Eq. (3-B3) with respect to V, using Eqs. (3-B1b) and (3-B2), one obtains the following relationship between the aggregate volume and aspect ratio:

$$V = (2\delta)^3 \left[-\frac{dN/dr_a}{ds/dr_a}\left(1 + \frac{\sigma_0}{\mu_0 H_0^2 \delta}\left(\frac{1+N\chi}{\chi}\right)^2\right) + 2s\frac{\chi}{1+N\chi}\right]^3, \tag{3-B4}$$

with N and s given by Eqs. (3-A1b) and (3-B1c) as functions of r_a. In the high aspect ratio limit, relevant for the present study, the last equation reduces to

$$V = \begin{cases} \frac{\pi^4\delta^3}{48}\left[\frac{r_a^{7/3}}{\ln(2r_a)-3/2}\left(1+\frac{\sigma_0}{\mu_0\chi^2 H_0^2\delta}\right) + 12\chi r_a^{1/3}\right]^3, \text{ at } r_a^2 \sim 12\chi \gg 1, \\ \frac{\pi^4}{48}\left(1+\frac{\sigma_0}{\mu_0\chi^2 H_0^2\delta}\right)^3 \frac{r_a^7}{(\ln(2r_a)-3/2)^3}, \text{ at } r_a^2 \gg 12\chi \text{ and } r_a^2 \gg 1, \\ 36\pi^4\chi^3\delta^3 r_a, \text{ at } 12\chi \gg r_a^2 \gg 1 \end{cases} \tag{3-B5}$$

The two unknown parameters, the 1st term σ_0 of the aggregate surface tension and the surface layer thickness δ are determined by fitting experimental $V(r_a)$ dependencies to the theoretical dependencies [Eqs. (3-B4) or (3-B5)]. This fit is shown in Fig. 3.8 for several series of experimental data. The figure shows that, because of some dispersion of data, it is quite difficult to observe the effect of the magnetic field amplitude H_0 and frequency ν on experimental $V(r_a)$ dependencies. The theory [Eq. (3-B4)] also predicts only a slight shift of the $V(r_a)$-dependency

with the change in magnetic field amplitude H_0 – see the black solid and blue dashed curves for $H_0 = 9$ and 6 kA/m, respectively. The best fit by Eq. (3-B4) is obtained for the following values of the adjustable parameters: $\delta = 12$ nm and $\sigma_0 = 1.5 \times 10^{-4}$ N/m. As expected, the first value is close to the average nanoparticle diameter $\langle d_m \rangle = 8.1$ nm while the second one is two orders of magnitude larger than the one ($\sigma_0 = 2.8 \times 10^{-6}$ N/m) found by Bacri et al. (1994).

Notice that the classical model [Zubarev and Ivanov (1997)], neglects the variation of the surface tension with r_a (last term in brackets of Eq. (3-B4)), corresponds to the limit $r_a^2 \gg 12\chi$ of our model. This limit provides the behaviour $V \propto r_a^7$, that is reproduced by the second expression in Eq. (3-B5) of the high aspect ratio limit of our model. It is found that the classical model is not able to fit even approximately the experimental data in Fig. 3.8. On the other hand, at not too high aspect ratios $r_a \lesssim 10$, relevant for our experiments, we are in the opposite limit $12\chi \gg r_a^2 \gg 1$, for which the aggregate volume is predicted to be roughly linear with aspect ratio, $V \propto r_a$, as inferred from the third expression of Eq. (3-B5). The theoretical $V(r_a)$ dependency corresponding to this limit is shown by a dotted red line in Fig. 3.8. For the sake of comparison, we have used the same value $\delta = 12$ nm of the transition layer thickness for this dependency. This simple linear law seems to agree with experimental data only at aspect ratios $r_a \lesssim 8$. However, this approximation gives a good agreement on the aggregate half-thickness b that does not change with the magnetic field amplitude and frequency both in experiments and in theory. In the considered limit $12\chi \gg r_a^2 \gg 1$, the b value is easily obtained from the third expression of Eq. (3-B5) using the obvious geometrical relationship $V = 4\pi b^3 r_a/3$:

$$b \approx 3\pi\chi\delta \approx const. \qquad \text{(3-B6)}$$

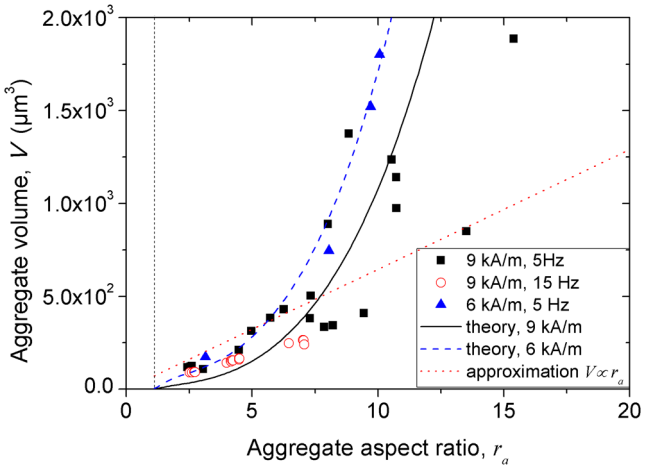

Figure 3.8: Experimental dependencies (symbols) of the aggregate volume on its aspect ratio. The solid black and the dashed blue curves correspond to the fit of experimental data by Eq. (3-B4) with the adjustable parameters $\delta = 12$ nm and $\sigma_0 = 1.5 \times 10^{-4}$ N/m. The dotted red line corresponds to the prediction of the limit $12\chi \gg r_a^2 \gg 1$ [third expression in Eq. (3-B5)] at $\delta = 12$ nm. The vertical dashed line corresponds to the aspect ratio $r_a = 1$.

The evaluation gives $b \approx 2.5\ \mu m$ at $\delta = 12$ nm and $\chi \approx 22$ in perfect agreement with experiments. In summary, the present model of the aggregate shape/surface tension allows a correct agreement with experiments and fits between two limiting behaviours: $V \propto r_a$, $b \approx const, a \propto r_a \propto V$ at $r_a^2 \ll 12\chi$ and $V \propto r_a^7, b \propto r_a^2 \propto V^{2/7}, a \propto r_a^3 \propto V^{3/7}$ at $r_a^2 \gg 12\chi$, with the second limit being commonly admitted in literature [Zubarev and Ivanov (1997); Ezzaier et al. (2017)].

Appendix 3-C. Hydrodynamic coefficient A_f and hydrodynamic pressure.

Within the thin diffusive boundary layer around the aggregate, the velocity field in the reference frame of the aggregate [Fig. 3.2] is supposed to take a functional form as in the case of the creeping flow past a cylinder. In polar coordinates (ρ, θ) introduced in Fig. 3.2a, it reads [Adamczyk and Van De Ven (1981)]:

$$v_\theta = 4A_f u_\infty \frac{\rho - r}{r} \sin\theta, \qquad v_\rho = -2A_f u_\infty \left(\frac{\rho - r}{r}\right)^2 \cos\theta, \qquad (3\text{-C1})$$

where r is the radial coordinate of the aggregate surface at an axial position z, and the velocity at the infinity is set to $u_\infty = \omega z$. The hydrodynamic coefficient A_f in the present case, a rotating ellipsoidal aggregate is expected to be different from that for the flow past an infinite cylinder. The value of A_f for a given axial position z can be easily obtained by comparing the shear rate near the aggregate surface

$$\frac{\partial v_\theta}{\partial \rho} = 4A_f \frac{\omega z}{r} \sin\theta \qquad (3\text{-C2})$$

given by the velocity field (3-C1) with the shear rate occurring on the surface of rotating ellipsoidal aggregate, for which the velocity field is given by the Jeffery solution [Jeffery (1922)]. After some transformations, the expressions for the transverse velocity components in the cartesian reference frame of the aggregate read:

$$v_x = -\frac{4xyz\Pi\varepsilon}{(b^2+\lambda)^3(a^2+\lambda)^{3/2}}[(b^2+\lambda)a^2-(a^2+\lambda)b^2],$$

$$v_y = \omega z - 2z\varepsilon(\gamma a^2+\beta b^2) - \frac{4y^2z\Pi\varepsilon}{(b^2+\lambda)^3(a^2+\lambda)^{3/2}}[(b^2+\lambda)a^2-(a^2+\lambda)b^2],$$

$$\Pi(\lambda) = \left[\frac{x^2+y^2}{(b^2+\lambda)^2}+\frac{z^2}{(a^2+\lambda)^2}\right]^{-1}, \qquad \varepsilon = \frac{\omega}{2(b^2\beta_0+a^2\gamma_0)}, \tag{3-C3}$$

$$\beta(\lambda) = \int_\lambda^\infty \frac{d\lambda}{(b^2+\lambda)^2(a^2+\lambda)^{1/2}}, \gamma(\lambda) = \int_\lambda^\infty \frac{d\lambda}{(b^2+\lambda)(a^2+\lambda)^{3/2}},$$

$$\beta_0 = \beta(0) = b^{-3}\left[\frac{r_a}{r_a^2-1} - \frac{\operatorname{acosh} r_a}{(r_a^2-1)^{3/2}}\right], \ \gamma_0 = \gamma(0) = -2b^{-3}\left[\frac{1}{r_a(r_a^2-1)} - \frac{\operatorname{acosh} r_a}{(r_a^2-1)^{3/2}}\right],$$

with the ellipsoidal coordinate λ being related to the cartesian coordinates by

$$\frac{x^2+y^2}{b^2+\lambda}+\frac{z^2}{a^2+\lambda} = 1.$$

Notice that β in Eq. (3-C3) has not to be confounded with the constant β used in the population balance equation [Eq. (3.25)]. Expanding both velocity components into series around $\lambda = 0$ and keeping only the linear term on λ, we get the following expressions for the fluid velocity in the vicinity of the aggregate surface:

$$v_x = \frac{4(b^2-a^2)xyz\Pi_0\varepsilon}{b^6a^3}\lambda, \ v_y = \frac{4z\varepsilon}{b^2a}\lambda + \frac{4(b^2-a^2)y^2z\Pi_0\varepsilon}{b^6a^3}\lambda, \ \Pi_0 = \Pi(0) = \left(\frac{x^2+y^2}{b^4}+\frac{z^2}{a^4}\right)^{-1} \tag{3-C4}$$

The shear rate on the ellipsoid surface ($\lambda = 0$) is evaluated as follows:

$$\left(\frac{\partial v_\theta}{\partial\rho}\right)_{\lambda=0} = -\left(\frac{\partial v_x}{\partial\rho}\right)_{\lambda=0}\cos\theta + \left(\frac{\partial v_y}{\partial\rho}\right)_{\lambda=0}\sin\theta = \frac{8\Pi_0\varepsilon}{b^4a}rz\sin\theta, \tag{3-C5}$$

where we have used the following relationships:

$$x = -\rho\sin\theta, \ y = -\rho\cos\theta, x^2+y^2 = \rho^2, \qquad \left(\frac{\partial\lambda}{\partial\rho}\right)_{\lambda=0} = \frac{2\Pi_0\rho}{b^2}.$$

With a high aspect ratio limit, $r_a \gg 1$, the equation (3-C5) reduces to

$$\left(\frac{\partial v_\theta}{\partial \rho}\right)_{\lambda=0} \approx \frac{2}{\ln(2r_a)-1/2}\frac{\omega z}{r}\frac{\hat{r}^2}{\hat{r}^2+\hat{z}^2/r_a^2}\sin\theta, \qquad \text{(3-C6)}$$

with $\hat{r} = r/b$ and $\hat{z} = z/a$ being the dimensionless coordinates of the aggregate surface. Equalizing the right-hand parts of Eqs. (3-C2) and (3-C6), we arrive at Eq. (3.12b) for the hydrodynamic coefficient A_f.

Let us now evaluate the hydrodynamic pressure on the surface of ellipsoidal aggregate spinning in a quiescent suspending liquid at angular frequency ω [Fig. 3.2a]. According to Jeffery (1922), at any point of the suspending fluid the hydrodynamic pressure reads:

$$p_H = -\frac{8\eta_0 yz\Pi\varepsilon(a^2-b^2)}{(b^2+\lambda)^2(a^2+\lambda)^{3/2}}. \qquad \text{(3-C7)}$$

At the aggregate surface, $\lambda = 0$, under a high aspect ratio limit, $r_a \gg 1$, the last equation reduces to:

$$p_H \approx -\frac{2\eta_0\omega}{\ln(2r_a)-1/2}\frac{yz}{b^2}. \qquad \text{(3-C8)}$$

The pressure takes its maximal absolute value at the points on the aggregate surface situated at $x = 0, y = \pm b/\sqrt{2}, z = a/\sqrt{2}$:

$$|p_{H,max}| = \frac{\eta\omega r_a}{\ln(2r_a)-1/2}. \qquad \text{(3-C9)}$$

This value is used as a characteristic hydrodynamic pressure on the aggregate surface.

Appendix 3-D. Diffusive flux towards the cavity

We consider nanoparticle diffusion from infinity where nanoparticle volume fraction is φ towards the cavity, representing an oblate ellipsoid of the semi-axes b and a [Fig. 3.2c]; the nanoparticle volume fraction on the cavity surface is $\varphi_c < \varphi$. The diffusion problem is considered in the ellipsoidal reference frame (ξ, η, ϕ) [Fig. 3.2c] related to the cylindrical reference frame (ρ, z, ϕ) as follows [Happel and Brenner (1983)]:

$$z = c\sinh\xi\cos\eta, \quad \rho = c\cosh\xi\sin\eta, \quad \phi = \phi, \qquad c = (a^2-b^2)^{1/2}.$$

In the considered boundary conditions, the particle volume fraction is constant on the surfaces of confocal oblate ellipsoids, thus, only depends on the coordinate ξ describing the position of these ellipsoids [Fig. 3.2c]. The surface flux density vector is everywhere perpendicular to these surfaces and its single non-zero ξ-component reads:

$$j_\xi = -D_p\nabla_\xi\varphi = -\frac{D_p}{c(\cosh^2\xi-\sin^2\eta)^{1/2}}\frac{d\varphi}{d\xi}. \qquad \text{(3-D1)}$$

The volume nanoparticle flux across any coordinate surface $\xi = const$ is obtained by integration of the flux density:

$$J_{V1} = -\oint j_\xi dS = -2\pi \int_0^\pi j_\xi c^2 (\cosh^2\xi - \sin^2\eta)^{\frac{1}{2}} \cosh\xi \sin\eta \, d\eta = 4\pi D_p c \cosh\xi \frac{d\varphi}{d\xi}, \tag{3-D2}$$

where the minus sign at the integral indicates that the nanoparticle flux towards the cavity is opposed to the outward direction of the ξ axis. Isolating $d\varphi$ and integrating over ξ from the cavity surface to the infinity, we get:

$$\varphi - \varphi_c = \int_{\xi_0}^{\infty} \frac{J_{V1}}{4\pi D_p c} \frac{d\xi}{\cosh\xi} = \frac{J_{V1}}{4\pi D_p c} \left(\pi - 2\,\mathrm{atan}\left(e^{\xi_0}\right)\right), \tag{3-D3}$$

where the volume flux J_{V1} is considered to be constant in the conventional approximation of quasi-stationary diffusion and $\xi_0 = \mathrm{atanh}(b/a) = \mathrm{atanh}({r_a}^{-1})$ is the value of ξ at the cavity surface. The expression for J_{V1} as a function of the volume fraction difference $\varphi - \varphi_c$ directly follows from Eq. (3-D3):

$$J_{V1} = \frac{4\pi D_p (a^2 - b^2)^{1/2}}{\pi - 2\,\mathrm{atan}\left(e^{\mathrm{atanh}({r_a}^{-1})}\right)} (\varphi - \varphi_c). \tag{3-D4}$$

For high aspect ratio aggregates $r_a \gg 1$, the cavity is a very oblate ellipsoid, and the equation (3-D4) reduces to Eq. (3.14).

Appendix 3-E. Coagulation kernel

To evaluate the flux of neighbouring aggregates towards the target aggregate, let us consider two slender aggregates of the volumes V and V', semi-lengths a and a' and aspect ratios r_a and ${r_a}'$ rotating in the same horizontal plane, as observed in experiments and shown in Fig. 3.2d. Recall that the aggregate half-thickness is nearly independent of the volume: $b \approx b' \approx const$. The origin of the Cartesian (ρ, z) and polar (r, θ) reference frames is placed in the centre of the target aggregate (V, a, r_a), and the z axis with $\theta = 0$ is aligned with the major axis of the target aggregate. The flux $J_{V \to V'}$ of the neighbouring aggregates towards the targeted aggregate could be evaluated with the help of the cell model widely used for the calculation of mechanical, thermal, or optical properties of composite materials [Christensen (1980); Berthier (1993)]. According to this model, individual structural units (aggregates in our case) are surrounded by representative cells with appropriately chosen boundary conditions on the cell surface. Since all the aggregates perform homogeneous rotation in the same horizontal plane, it is reasonable to choose a disk-like shape for the representative cells with the axis of symmetry perpendicular

to the rotation plane and passing through the aggregate centres [Fig. 3.2d]. The cell thickness is equal to the vertical gap h of the sample and its volume, V_{cell} or V'_{cell} is chosen to respect the volume fraction $\Phi = V/V_{cell} = V'/V'_{cell}$ of the aggregates in the colloid. The cell radii can be easily evaluated from geometrical considerations:

$$R = \left(\frac{V}{\pi h \Phi}\right)^{1/2} = 2b\left(\frac{a}{3h\Phi}\right)^{1/2}, R' = \left(\frac{V'}{\pi h \Phi}\right)^{1/2} = 2b\left(\frac{a'}{3h\Phi}\right)^{1/2}. \quad \text{(3-E1)}$$

The cells of neighbouring aggregates touch the cell of the target aggregate, and the distance r between the centres of two aggregates is equal to $r = R + R'$. The small phase lag ϕ between the aggregates and the field orientation is neglected along with the possible misalignment of two neighbouring aggregates because of magnetic and hydrodynamic interactions between them. Thus, all the aggregates are supposed to be parallel to the instantaneous direction of the rotating field.

The flux $J_{V\to V'}$ can be related to the components F_ρ and F_z of the magnetic force acting between the target and the neighbouring aggregate, as follows [Ezzaier et al. (2017)]:

$$J_{V\to V} = -n_V\left[\tilde{b}_\parallel \int F_z n_z dS + \tilde{b}_\perp \int F_\rho n_\rho dS\right], \quad \text{(3-E2a)}$$

$$\tilde{b}_\parallel \approx \frac{\ln(2r_a)-\frac{1}{2}}{4\pi\eta_0 a} + \frac{\ln(2r_{a'})-\frac{1}{2}}{4\pi\eta_0 a'},\ \ \tilde{b}_\perp \approx \frac{\ln(2r_a)+\frac{1}{2}}{8\pi\eta_0 a} + \frac{\ln(2r_{a'})+\frac{1}{2}}{8\pi\eta_0 a'},\ \ n_z = \cos\theta,\ \ n_\rho = \sin\theta,\ \ dS = hr\, d\theta \quad \text{(3-E2b)}$$

where $\tilde{b}_\parallel$ and $\tilde{b}_\perp$ are longitudinal and transverse components of the tensor of mutual hydrodynamic mobility of both aggregates, evaluated at a high aspect ratio limit, $r_a, r_a' \gg 1$ [Brenner (1974)]; the integrals are taken over the lateral cylindrical surface S of the excluded volume shell surrounding the target aggregate and have a radius equal to the distance r between aggregates' centres; n_z and n_ρ are components of the unit outward vector normal to the surface S; the minus sign corresponds to the positive inward flux. Notice that we do not need to average the flux $J_{V\to V'}$ over all possible aggregate orientations because it is implicitly done by integration of the flux density over the surface S of the excluded volume shell.

The magnetic force between aggregates can be evaluated in non-point dipole limit, i.e. representing the aggregate magnetic moments $m_a = 2aq$ and $m_a' = 2a'q'$ as the dipole moment of two equivalent charges $+q$ and $-q$ (or $+q'$ and $-q'$) placed onto aggregate tips and calculating the force between four pairs of charges belonging to two aggregates [Fig. 3.2d]. A similar approach has been used in our previous work on the permanent magnetic field and

equal-sized aggregates [Ezzaier et al. (2017)]. In the present case of rotating field and unequal aggregates, we get:

$$F_\rho = \frac{qq'}{4\pi\mu_0 r^2}\left[\frac{\sin\theta}{\hat{r}_{NN}^3} + \frac{\sin\theta}{\hat{r}_{SS}^3} - \frac{\sin\theta}{\hat{r}_{NS}^3} - \frac{\sin\theta}{\hat{r}_{SN}^3}\right] \quad \text{(3-E3a)}$$

$$F_z = \frac{qq'}{4\pi\mu_0 r^2}\left[\frac{\cos\theta-(\hat{a}-\hat{a}')}{\hat{r}_{NN}^3} + \frac{\cos\theta+(\hat{a}-\hat{a}')}{\hat{r}_{SS}^3} - \frac{\cos\theta-(\hat{a}+\hat{a}')}{\hat{r}_{NS}^3} - \frac{\cos\theta+(\hat{a}+\hat{a}')}{\hat{r}_{SN}^3}\right] \quad \text{(3-E3b)}$$

$$q = \frac{m_a}{2a} = \frac{\mu_0 M_a V}{2a} \approx \frac{2\pi}{3}\mu_0\chi H_0 b^2 = q',$$

$$\hat{r}_{NN}^2 = 1 + (\hat{a}-\hat{a}')^2 - 2(\hat{a}-\hat{a}')\cos\theta,$$

$$\hat{r}_{SS}^2 = 1 + (\hat{a}-\hat{a}')^2 + 2(\hat{a}-\hat{a}')\cos\theta, \quad \text{(3-E3c)}$$

$$\hat{r}_{NS}^2 = 1 + (\hat{a}+\hat{a}')^2 - 2(\hat{a}+\hat{a}')\cos\theta,$$

$$\hat{r}_{SN}^2 = 1 + (\hat{a}+\hat{a}')^2 + 2(\hat{a}+\hat{a}')\cos\theta,$$

where $\hat{r}_{ik}$ $(i,k = N,S)$ are the distances between the i^{th} pole of the target aggregate and the k^{th} pole of the neighbouring aggregate, normalized by the distance r between the centres of both aggregates; the subscripts "*N*" and "*S*" stand for the north ($+q$ or $+q'$) and south ($-q$ or $-q'$) poles, respectively, $\hat{a} = a/r$ and $\hat{a}' = a'/r$ are the aggregates' half-lengths normalized by r; $M_a \approx M_a{}' \approx \chi H_0$ is the aggregate magnetization evaluated in high aspect ratio limit, $r_a, r_a{}' \gg 1$ neglecting demagnetizing effects. Combining Eqs. (3.20), (3-E1) – (3-E3), after some transformations, we arrive at the following expression for the coagulation kernel:

$$K(V,V') = -\frac{\mu_0\chi^2 H_0^2 b^2 h}{72\eta_0}\frac{\hat{a}+\hat{a}'}{r_a+r_{a'}}[2B_-(r_a,r_a{}')X(\hat{a},\hat{a}') + B_+(r_a,r_a{}')Y(\hat{a},\hat{a}')] \geq 0, \quad \text{(3-E4a)}$$

$$B_\pm(r_a,r_a') = \frac{\ln(2r_a)\pm 1/2}{r_a} + \frac{\ln(2r_{a'})\pm 1/2}{r_{a'}}, \quad \text{(3-E4b)}$$

$$X(\hat{a},\hat{a}') = 4\int_0^{\pi/2}\left(\frac{\cos\theta-(\hat{a}-\hat{a}')}{\hat{r}_{NN}^3} + \frac{\cos\theta+(\hat{a}-\hat{a}')}{\hat{r}_{SS}^3} - \frac{\cos\theta-(\hat{a}+\hat{a}')}{\hat{r}_{NS}^3} - \frac{\cos\theta+(\hat{a}+\hat{a}')}{\hat{r}_{SN}^3}\right)\cos\theta\, d\theta, \quad \text{(3-E4c)}$$

$$Y(\hat{a},\hat{a}') = 4\int_0^{\pi/2}\left(\frac{1}{\hat{r}_{NN}^3} + \frac{1}{\hat{r}_{SS}^3} - \frac{1}{\hat{r}_{NS}^3} - \frac{1}{\hat{r}_{SN}^3}\right)\sin^2\theta\, d\theta, \quad \text{(3-E4d)}$$

$$\hat{a} = \frac{1}{2}\left(\frac{3h\Phi}{b}\right)^{1/2}\frac{r_a}{r_a{}^{1/2}+(r_a')^{1/2}},\ \hat{a}' = \frac{1}{2}\left(\frac{3h\Phi}{b}\right)^{1/2}\frac{r_{a'}}{r_a{}^{1/2}+(r_a')^{1/2}}, \quad \text{(3-E4e)}$$

where the integrals in Eqs. (3-E4c), (3-E4d) are evaluated numerically. One can explicitly express the coagulation kernel through the aggregate volumes V and V' by replacing r_a and $r_a{}'$ in Eqs. (3-E4) by the second expression of Eq. (3.16). As expected, the coagulation kernel in Eq. (3-E4a) is symmetric concerning volume permutation: $K(V,V') = K(V',V)$.

Chapter 4. Field-induced flow recirculation in a closed microfluidic channel[8]

In this Chapter, we aim to reply to the second question related to the target biomedical application formulated in Sec. 1.3: Once the elongated micron-sized aggregates are formed, will they be able to rotate continuously and generate recirculation flows in the blocked blood vessels? The primary hypothesis is that the recirculation in a closed channel may only appear due to the combination of the aggregate rotation and gradients of the aggregate concentration, breaking the symmetry of the magnetic torque density of the whole colloid. The concentration gradients may be easily induced by relatively weak magnetic field gradients superimposed onto the homogeneous rotating magnetic field. Following this idea, we generate the flows in a closed rectangular microfluidic channel and measure the velocity profile by particle image velocimetry (PIV) technique. We also present a theoretical model allowing prediction of the velocity profile and analysis of the recirculation intensity as a function of the control parameters, such as the magnetic field amplitude and frequency, suspending liquid viscosity, aggregate size, and volume fraction. First, we report in Sec. 4.1 the qualitative observations on the generated flows. Then, in Sec. 4.2, we present the theoretical model. At the same time, the quantitative characterisation of the observed flow pattern and the aggregate collective dynamics are reported in Sec. 4.3, where, among others, the experimental velocity profiles are compared to experimental ones. Conclusions will be outlined in Sec 4.4.

4.1 Results of qualitative observations

To check the primary hypothesis formulated at the beginning of this chapter, we realise the most straightforward experimental configuration, in which the rotating magnetic field is combined with a magnetic field gradient. This is achieved using a three-coil system (Sec. 2.3.1),

[8] Main results of this Chapter are reported in the paper [Raboisson-Michel M., J. Queiros Campos, S. Schaub, S. Toe, G. Verger-Dubois, A. Zubarev, and P. Kuzhir. Field-induced recirculation flow of a magnetic colloid under rotating magnetic fields. Sumbitted], while auxiliary results on the modelling of actuated flows are published in a series of papers:

Musickhin, A., Yu Zubarev, A., Raboisson-Michel, M., Verger-Dubois, G., & Kuzhir, P. (2020). Field-induced circulation flow in magnetic fluids. Philosophical Transactions of the Royal Society A, 378(2171), 20190250

Zubarev, A. Y., Raboisson-Michel, M., Verger-Dubois, G., & Kuzhir, P. (2020). To the theory of ferrohydrodynamic circulating flow induced by running magnetic field. The European Physical Journal Special Topics, 229(19), 2961-2966.

Zubarev, A. Y., Chirikov, D., Musikhin, A., Raboisson-Michel, M., Verger-Dubois, G., & Kuzhir, P. (2021). Nonlinear theory of macroscopic flow induced in a drop of ferrofluid. Philosophical Transactions of the Royal Society A, 379(2205), 20200323.

Chirikov, D., Zubarev A., Kuzhir P., Raboisson-Michel M., Verger-Dubois G. To the theory of magnetically induced flow in a ferrofluid cloud: effect of the cloud initial shape Eur. Phys. J. Spec. Top. 231, 1187–1194 (2022)

providing us with a circularly polarised magnetic field at the centre of the system with a weak gradient oriented along the y-axis across the channel length, as defined in Fig. 2.4. By simple optical observations, we will inspect in this Section whether this magnetic field configuration is appropriate for the generation of the recirculating flows.

For this purpose, we injected a dilute magnetic colloid at a nanoparticle volume fraction φ_p =0.16% vol and embedded flow tracers (cf. Sec. 2.1.1) into a microfluidic channel and applied an external rotating magnetic field with a dominant gradient oriented along the y direction [Eq. (2.3)] . Before the magnetic field application, the colloid was homogeneous and did not show any micron-sized agglomerates visible in the Infinity tube microscope at an approximate spatial resolution of 1 μm. However, once the rotating field is on, the primary nanoparticle agglomerates (of a size $d_{H2} = 120 - 140$ nm, cf. Fig. 2.1) are self-assembled into elongated secondary agglomerates with a rod-like shape. These aggregates synchronously rotate with the magnetic field. On the one hand, the aggregate size progressively increases with time until reaching a steady state average length and diameter on the order of $L = 50$ μm and $d = 5$ μm, respectively, as seen in Chapter 3. In this magnetic field configuration, the rotating aggregates migrate in the y direction of the dominant field gradient, i.e. towards the channel's back wall, distinguished in the top view snapshots as the upper horizontal line – see the channel snapshot in Fig. 4.1a. Once achieved the back wall, the aggregates do not stick to it but continue their synchronous rotation with the field in the vicinity of this wall, as checked by comparing the period of aggregate rotation with that of the magnetic field. Moreover, once close to the wall, the aggregates move on the left along the back wall, showing a kind of rolling motion (combination of clockwise rotation with leftward translation) equivalent to a rolling wheel along the road. Reversal of the field rotation direction reverses the sense of the aggregate translation. Such rolling behaviour can be explained by hydrodynamic interactions between the aggregates and the walls. The clockwise spinning propels the ambient fluid layer adjacent to the wall in the right direction so that the aggregates exert a force on the wall in the same right direction. According to the 3rd Newton's law of mechanics, the wall exerts on aggregates a force in the opposite direction, propelling them to the left. The situation is somewhat similar to the gravitational settling of a spherical particle near a vertical wall situated on the right side of the particle: the downward particle translation induces its counter-clockwise spinning [Happel and Brenner (1983)], as schematically shown in Fig. 4.1b.

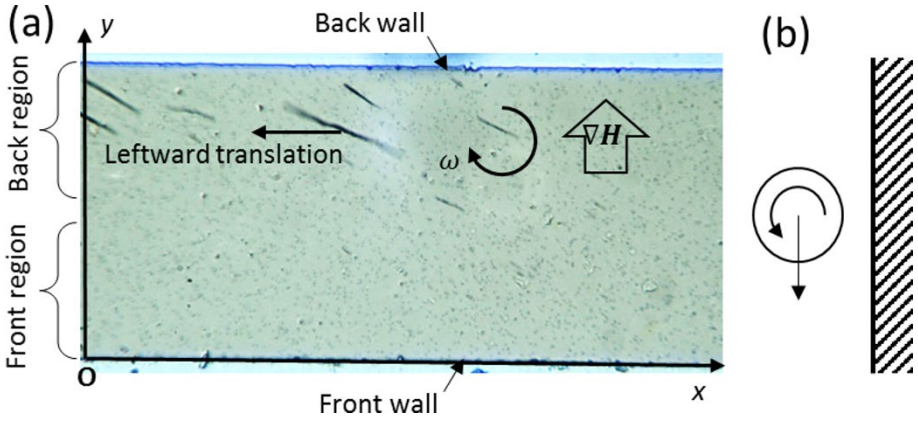

Figure 4.1: Snapshot of the microfluidic channel with the gradient rotating magnetic field clockwise in the channel's x-y plane and the field gradient oriented along the -y-axis (a). The arrow shows the direction of aggregate translation. The aggregate leftward translation in (a) is somewhat similar to the counter-clockwise rotation of a spherical particle induced by a gravitational settling along a vertical wall, as shown in (b).

From the early moments after the field application, we observe not only the aggregate translation, but the motion of the ambient fluid manifested through the displacement of the fluid tracers. The fluid motion visibly achieves a steady state that lasts up to at least 300 s (until the end of the observation period). The characteristic time of the initial transient regime $\tau \sim 100$ s seems to correspond to the largest timescale τ of the two processes: (a) field-induced aggregation and (b) aggregate migration towards the back wall. We will focus on the steady-state flow at $t > 100$ s. Visually, the ambient fluid is convected by moving aggregates to the left in the back region of the channel while it moves to the right in the front region. Thus, we observe the fluid recirculation throughout the 200 s steady-state observation period[9]. Intuitively, this recirculation can be explained by zero total flux that must hold in the considered closed channel: if the back fluid layer is "sucked" to the left by rolling aggregates, the front layer must flow to the right to compensate for the back flux. It is also instructive to notice that aggregate translational motion sometimes appears somewhat chaotic; when the aggregates get close to each other, they describe complicated trajectories that can slow down their overall translation to the left and repel them further from the back wall. The aggregates exhibit an irregular spacing with their neighbours and irregular distance from the back wall, such that, on average, they occupy about 30 % of the channel width in the back region of the channel.

Quantitative features of the observed recirculation flow are obtained through the PIV analysis. However, we will first present theoretical calculations of the velocity profiles (Sec. 4.2). Then, we secure different characteristics of the aggregates (intervening into the model)

[9] A video demonstrating the recirculation flow and a complex dynamic of the rotating aggregates will be avaliable in Supplementary Material of the submitted paper (cf. note « 9 »), whether it is accepted for publication

from experimental snapshots (Sec. 4.3.1), and finally compare theoretical velocity profiles with experimental ones obtained through the PIV analysis (Sec. 4.3.2).

4.2 Theory

We are looking for the velocity profile of a recirculation flow generated in a magnetic colloid in a closed rectangular channel and subject to a non-uniform rotating magnetic field. The problem geometry is shown on the right panel of Fig. 2.4 and Fig. 4.1a. Recall that the channel dimensions along x, y and z directions are denoted by l, h and b, respectively. Let us consider a volume of a dilute magnetic colloid under magnetic field $\boldsymbol{H}$ rotating in xy-plane with a non-zero field gradient (the absolute value of the magnetic field can generally vary along x, y and z). However, the field variation along the channel dimensions is deemed relatively minor, such that the field conserves its circular polarisation at each point of the channel – the condition verified in our experiments. As shown in Chapter 3, the rotating magnetic field creates micron-sized needle-like aggregates composed of a score of magnetic nanoparticles. The volume fraction Φ of the aggregates is defined as the total volume of aggregates divided by the suspension volume. The aggregates rotate synchronously with the field and exhibit a small phase lag between their orientation and the magnetic field vector. This is checked in the limit of low Mason numbers, $Ma \ll 1$, valid for the present work, as has already been checked in Chapter 3, with Ma being defined by Eq. (3.1). We will suppose that all the aggregates have the same size and a shape of a prolate ellipsoid of revolution characterised by the length-to-diameter ratio (aspect ratio) $r_a = L/d \gg 1$. The analysis can, in principle, be generalised for polydisperse size distribution and non-ellipsoidal shape. According to our observations, the rotating aggregates translate along the magnetic field gradient and mostly accumulate behind the middle plane $y > h/2$ of the channel, where the magnetic field is stronger [Fig. 4.1a]. Strictly speaking, we might consider the motion of the solid phase (aggregates) and the suspending liquid phase separately. However, for the finding of the velocity profile of the whole colloid, it is enough to consider the colloid as a single but heterogeneous phase. The spatial heterogeneity will be quantified through a non-uniform distribution of aggregate concentration that must be known from experiments. The experimental timescale of the transient response related to the concentration redistribution is much larger than the rotation period of aggregates. In this context, it is reasonable to consider the momentum balance equation averaged over the rotation period.

Neglecting gravity, this equation takes the following general form valid for a suspension of elongated particles under a magnetic field [Bashtovoi et al. (1985); Pokrovskiy (1978); López-López et al. (2010)]:

$$\rho\left(\frac{\partial \mathbf{v}}{\partial t} + (\mathbf{v}\cdot\nabla)\mathbf{v}\right) = \operatorname{div}\boldsymbol{\sigma}, \tag{4.1a}$$

$$\sigma_{ik} = -P\delta_{ik} + 2\eta_0\gamma_{ik} + \sigma_{ik}^{s} + \sigma_{ik}^{a} + \sigma_{ik}^{M}, \tag{4.1b}$$

$$\sigma_{ik}^{a} = \frac{1}{2}\varepsilon_{ikl}K_l, \qquad \sigma_{ik}^{M} = -\frac{1}{2}\mu_0 H^2\delta_{ik} + H_i B_k, \tag{4.1c}$$

$$K_l = \mu_0(\mathbf{M}\times\mathbf{H})_l, \tag{4.1d}$$

where ρ is the colloid density; η_0 is the suspending liquid (water) viscosity; $\mathbf{v}$ and P are respectively the colloid velocity and pressure at a given point in the channel; σ_{ik} are the components of the symmetric stress tensor $\boldsymbol{\sigma}$, with σ_{ik}^{s} and σ_{ik}^{a} being respectively symmetric and antisymmetric parts of the particle contribution to the viscous stress tensor, and σ_{ik}^{M} being the Maxwell stress tensor; $\gamma_{ik} = (1/2)(\partial v_i/\partial x_k + \partial v_k/\partial x_i)$ is the rate-of-strain tensor; δ_{ik} and ε_{ikl} are Delta-Kronecker and Levi-Civita symbols, respectively; H_i and B_k are the *i*- or *k*-components of the magnetic field intensity vector $\mathbf{H}$ and magnetic flux density vector $\mathbf{B}$, respectively; $H = |\mathbf{H}|$; K_l is the *l*-component of the volume density $\mathbf{K}$ of a magnetic torque experienced by the magnetic colloid of a magnetisation $\mathbf{M}$; $\mu_0 = 4\pi\times10^{-7}$ H/m is the magnetic permeability of the vacuum. The characteristic value of the particle stress σ_{ik}^{s} is on the order of $\sigma^{s}\sim\Phi r^2\eta_0\dot{\gamma}$ with $\dot{\gamma}$ being a characteristic shear rate. In the dilute limit, Φr_a^2"1 valid for our experiments, the particle stress σ_{ik}^{s} becomes negligible as compared to the solvent contribution, $2\eta_0\gamma_{ik}$, to the viscous stress, and is further omitted. With this in mind, and using the continuity equation, $\operatorname{div}\mathbf{v} = 0$, along with the magnetostatics Maxwell equations, $\operatorname{div}\mathbf{B} = 0, \operatorname{rot}\mathbf{H} = \mathbf{0}, \mathbf{B} = \mu_0(\mathbf{H}+\mathbf{M})$, the momentum balance equation (4.1a) becomes similar to that derived for the colloids of spherical magnetic particles [Bashtovoi et al. (1985)]:

$$\rho\left(\frac{\partial \mathbf{v}}{\partial t} + (\mathbf{v}\cdot\nabla)\mathbf{v}\right) = -\nabla P + \eta_0\nabla^2\mathbf{v} + \mu_0(\mathbf{M}\cdot\nabla)\mathbf{H} + \frac{1}{2}\operatorname{rot}\mathbf{K}, \tag{4.2}$$

except for the viscosity η_0 which is replaced by the viscosity of the whole colloid in [Bashtovoi et al. (1985)], the difference coming from the dilute limit considered in the present work. The third and the fourth terms on the right-hand side of Eq. (4.2) stand for the magnetic force

(pulling the colloid along the field gradient) and the magnetic torque (that can make the colloid rotate in the rotating magnetic field). The expressions for these two terms can be simplified for our experimental conditions.

First, we suppose that a characteristic shear rate of the induced shear flow is much smaller than the rotational frequency of the aggregates, $\dot{\gamma}"\omega$. This hypothesis is valid in the considered dilute regime, $\Phi r_a^2"1$, will be justified *a-posteriori* once the velocity profile is calculated and the aggregate concentration determined. At such conditions, the shear contribution to the hydrodynamic torque $\mathbf{T}_h$ experienced by an aggregate can be neglected, and the torque balance in inertialess limit will give us $\mathbf{K} \approx -n\mathbf{T}_h = 2\eta_0\beta\Phi\boldsymbol{\omega}$, with $\boldsymbol{\omega}$ being a vector magnitude of the rotational frequency, $n = \Phi/V_a$ being the number density of aggregates, each having a volume V_a and β is a dimensional rotational friction coefficient evaluated in a high aspect ratio limit $r_a \gg 1$ [Brenner (1974), cf. Eq. (4.3b)]. Second, in our case of a small phase lag θ between the aggregate orientation and instantaneous magnetic field direction, the magnetic force term reduces to $\mu_0(\mathbf{M}\cdot\nabla)\mathbf{H} \approx (1/2)\Phi\chi\mu_0\nabla(H^2)$ under the linear magnetisation approximation, valid in our experimental magnetic field range ($H = 0 - 6$ kA/m), with χ being the aggregate magnetic susceptibility. This last approximate relationship has been strictly demonstrated using a series expansion of the magnetic force on θ parameter. Third, in the low Reynolds number limit, valid for our experiments, the convective term $(\mathbf{v}\cdot\nabla)\mathbf{v}$ can be neglected in the left-hand part of Eq. (4.2). Finally, according to our observations, we consider only the steady state regime at $t \gtrsim 100$ s, meaning that the aggregate volume fraction Φ and the fluid velocity $\boldsymbol{v}$ do not evolve with time. Applying the above conditions, the equation (4.2) takes the following form:

$$-\nabla P + \eta_0\nabla^2\mathbf{v} + \frac{1}{2}\Phi\chi\mu_0\nabla(H^2) + \eta_0\beta(\nabla\Phi\times\boldsymbol{\omega}) = \mathbf{0}, \qquad (4.3a)$$

$$\beta = \frac{r_a^2}{\ln(2r_a)-1/2}. \qquad (4.3b)$$

Tracking back to our experimental geometry, we can provide further simplifications. First, the angular speed $\boldsymbol{\omega}$ has the only non-zero z-component: $\omega_z = -\omega$ corresponding to the clockwise rotation in xy-plane. Second, the channel length is much larger than two other dimensions, l, b, h [Fig. 2.4] and considering the flow field far from the left and right borders of the channel, we can impose the single non-zero x-component of the velocity, $v_x = v(y,z)$ respecting the continuity equation, $\mathrm{div}\,\mathbf{v} = 0$. Third, in the experimental configuration of electromagnets, the $\nabla(H^2)$ term has the only non-zero component along the y axis. Recall that

the momentum balance equation is averaged over the aggregate rotation period so that $\nabla(H^2)$term is given by the right-hand side of Eq. (2.4b).

These approximations allow us to rewrite Eq. (4.3a) in the following component form:

$$\frac{\partial P}{\partial x} = \eta_0 \left(\frac{\partial^2 v}{\partial y^2} + \frac{\partial^2 v}{\partial z^2}\right) - \beta\eta_0\omega \frac{\partial \Phi}{\partial y}, \tag{4.4a}$$

$$\frac{\partial P}{\partial y} = \frac{1}{2}\Phi\chi\mu_0 \frac{\partial H^2}{\partial y} + \beta\eta_0\omega \frac{\partial \Phi}{\partial x}, \tag{4.4b}$$

$$\frac{\partial P}{\partial z} = 0. \tag{4.4c}$$

Since the term $\partial H^2/\partial y = (1/2)\left(\partial {H_{0y}}^2/\partial y\right)_{x=y=0}$ [cf. Eq. (2.4b)] mostly depends on the y-coordinate; it follows from Eqs. (4.4b), (4.4c) that the aggregate volume fraction Φ depends only on y and the pressure P depends on both x and y, but the last dependency admits the following superposition: $P = \mathcal{G}(x) + \mathcal{H}(y)$. With this in mind, on the left-hand side of Eq. (4.4a), $\partial P/\partial x = d\mathcal{G}(x)/dx$ can only depend on x, while the right-hand side can only depend on y and z. At such conditions, the equation (4.4a) can only hold if both sides are independent of x, y and z, or rather $\partial P/\partial x = C$, with C being some unknown constant. Let us now introduce the following scaling factors for several physical magnitudes: $[v] = \beta\omega\Phi_0 h$ for the velocity, $[\Phi] = \Phi_0$ – for the aggregate volume fraction and $[y] = h, [z] = b$ for the space coordinates, with Φ_0 being the average aggregate volume fraction in the suspension (before the aggregates migrate to the back region of the channel). The respective scaled quantities (from now on, denoted by the tilde symbol) are obtained by dividing their dimensional counterparts by the scaling factors. Thus, the equation (4.4a) can be rewritten in the following dimensionless form:

$$\frac{\partial^2 \tilde{v}}{\partial \tilde{y}^2} + \gamma^2 \frac{\partial^2 \tilde{v}}{\partial \tilde{z}^2} = 2C_1 + \frac{\partial \tilde{\Phi}}{\partial \tilde{y}}, \tag{4.5a}$$

$$\int_0^1 \tilde{\Phi}(\tilde{y}) d\tilde{y} = 1, \tag{4.5b}$$

where $\gamma = h/b$ and $C_1 = Ch/(2\beta\eta_0\omega\Phi_0)$ is a dimensionless unknown constant having a meaning of the dimensionless pressure gradient. The equation (4.5b) is nothing but the particle conservation condition. The equation (4.5a) is subjected to the non-slip boundary condition, and a condition of zero flow rate across the channel that should be respected for the considered closed channel:

$$\tilde{v}(0, \tilde{z}) = \tilde{v}(1, \tilde{z}) = \tilde{v}(\tilde{y}, 0) = \tilde{v}(\tilde{y}, 1) = 0, \tag{4.6a}$$

$$\int_0^1 d\tilde{z} \int_0^1 \tilde{v}(\tilde{y},\tilde{z}) d\tilde{y} = 0. \quad (4.6b)$$

Analytical solution of the boundary value problem (4.5a), (4.6a), (4.6b) is obtained by the Fourier series expansion method to the likeliness of the one used initially by Boussinesq in 1868 for calculations of the velocity profile in a rectangular duct – see for instance Cornish (1928). The final expression for the velocity profile in terms of infinite series reads:

$$\tilde{v}(\tilde{y},\tilde{z}) = \sum_{n=1}^{\infty} D_n G_n(\tilde{z}) \sin(n\pi\tilde{y}), \quad (4.7a)$$

$$G_n(\tilde{z}) = \frac{\sinh(n\pi\tilde{z}/\gamma)+\sinh(n\pi(1-\tilde{z})/\gamma)}{\sinh(n\pi/\gamma)} - 1, \quad (4.7b)$$

$$D_n = \frac{2K_n}{n\pi} - \frac{4[1-(-1)^n]}{(n\pi)^3} C_1, \quad (4.7c)$$

$$K_n = \int_0^1 \cos(n\pi\tilde{y})\, \widetilde{\Phi}(\tilde{y}) d\tilde{y}, \quad (4.7d)$$

$$C_1 = \frac{1}{4} \frac{\sum_{n=1}^{\infty} K_n M_n [1-(-1)^n]/(n\pi)^2}{\sum_{n=1}^{\infty} M_n [1-(-1)^n]/(n\pi)^4}, \quad (4.7e)$$

$$M_n = 2\gamma \frac{\tanh[n\pi/(2\gamma)]}{n\pi} - 1. \quad (4.7f)$$

The average dimensionless velocity across the channel thickness b is obtained by integration of Eq. (4.7a) over $\tilde{z}$:

$$\langle\tilde{v}\rangle(\tilde{y}) = \int_0^1 \tilde{v}(\tilde{y},\tilde{z}) d\tilde{z} = -\sum_{n=1}^{\infty} D_n M_n \sin(n\pi\tilde{y}), \quad (4.8)$$

with expressions for D_n and M_n provided in Eqs. (4.7c) and (4.7f), respectively.

Having obtained the exact solution for the velocity profile, let us first analyse some limiting cases. First, in the case of homogeneous aggregate volume fraction $\widetilde{\Phi}(\tilde{y}) = 1$ or $\Phi = \text{const} = \Phi_0$, we obtain zero velocity everywhere in the channel. This result directly follows from Eq. (4.3a), in which the last term on the right-hand side vanishes, and applying the curl operator to the rest three terms, one obtains $\nabla \times (\nabla^2 \mathbf{v}) = \mathbf{0}$ – a linear equation with a unique solution $\mathbf{v} = \mathbf{0}$ satisfying the boundary conditions [Eq. (4.6)]. This points out the necessity of a heterogeneous concentration profile ($\nabla\Phi \neq \mathbf{0}$) for the generation of recirculation flows, in complete agreement with the primary hypothesis of the present paper. Second, in a thick channel limit respecting the strong inequality $h << b << l$, the velocity is almost independent of the $\tilde{z}$ coordinate (except for the regions contiguous to the bottom and top channel walls, $\tilde{z} =$ 0 or 1), and equations (4.7a), (4.8) reduce to

$$\tilde{v}(\tilde{y}) = \langle\tilde{v}\rangle(\tilde{y}) \approx I_1(\tilde{y}) + 3(2I_2 - 1)\tilde{y}^2 + 2(1 - 3I_2)\tilde{y}, \text{at } \gamma = h/b << 1, \quad (4.9a)$$

$$I_1(\tilde{y}) = \int_0^{\tilde{y}} \widetilde{\Phi}(\tilde{y})d\tilde{y},\ I_2 = \int_0^1 I_1(\tilde{y})d\tilde{y}. \quad (4.9b)$$

This approximate solution can be obtained by directly integrating Eq. (4.5a), neglecting the second term on the left-hand side.

Recall that dimensional flow velocity can be obtained by multiplying the dimensionless velocity [Eq. (4.7a) or (4.8)] by the scaling factor $[v]$:

$$v(y,z) = \beta\omega\Phi_0 h\tilde{v}(\tilde{y},\tilde{z}), \quad (4.10a)$$

$$\langle v\rangle(y) = \beta\omega\Phi_0 h\langle\tilde{v}\rangle(\tilde{y}), \quad (4.10b)$$

with $\tilde{y} = y/h$ and $\tilde{z} = z/b$. To get numerical values of the velocity, we need to define the factor β depending on the aggregate aspect ratio r_a [Eq. (4.3b)], the average aggregate volume fraction Φ_0, as well as the aggregate concentration profile $\widetilde{\Phi}(\tilde{y})$ intervening into Eq. (4.7d). In the present study, these unknown quantities are drawn from experiments.

4.3 Quantitative results and discussion

4.3.1 Aggregate size, speed and volume fraction

The experimental distributions of aggregate lengths L and parameters β [Eq. (4.3b)], obtained through image processing are shown in Fig. 4.2a and b, respectively. The average values and standard deviations of these two parameters are equal to $L = 54 \pm 8$ µm and $\beta = 65 \pm 14$.

The average experimental value of the aggregate volume fraction is evaluated to be $\Phi_0 = (13 \pm 5) \times 10^{-5}$ and is consistent in order of magnitude with that $\Phi_0 = (3-6) \times 10^{-5}$ found in Chapter 3. The values of L, β, Φ_0, h, ω most of which intervene in the velocity calculation [Eq. (4.10b)] are summarised in Table 4.1, along with their standard deviations. Having found the values of β and Φ_0, we can now check the low shear rate hypothesis in the present model. As inferred from Eq. (4.10a), the shear rate in the xy-plane scales as $\dot{\gamma} = |dv/dy| \sim \beta\Phi_0\omega \sim 0.01\omega$, thus, the supposed limit $\dot{\gamma}"\omega$ holds in our experiments.

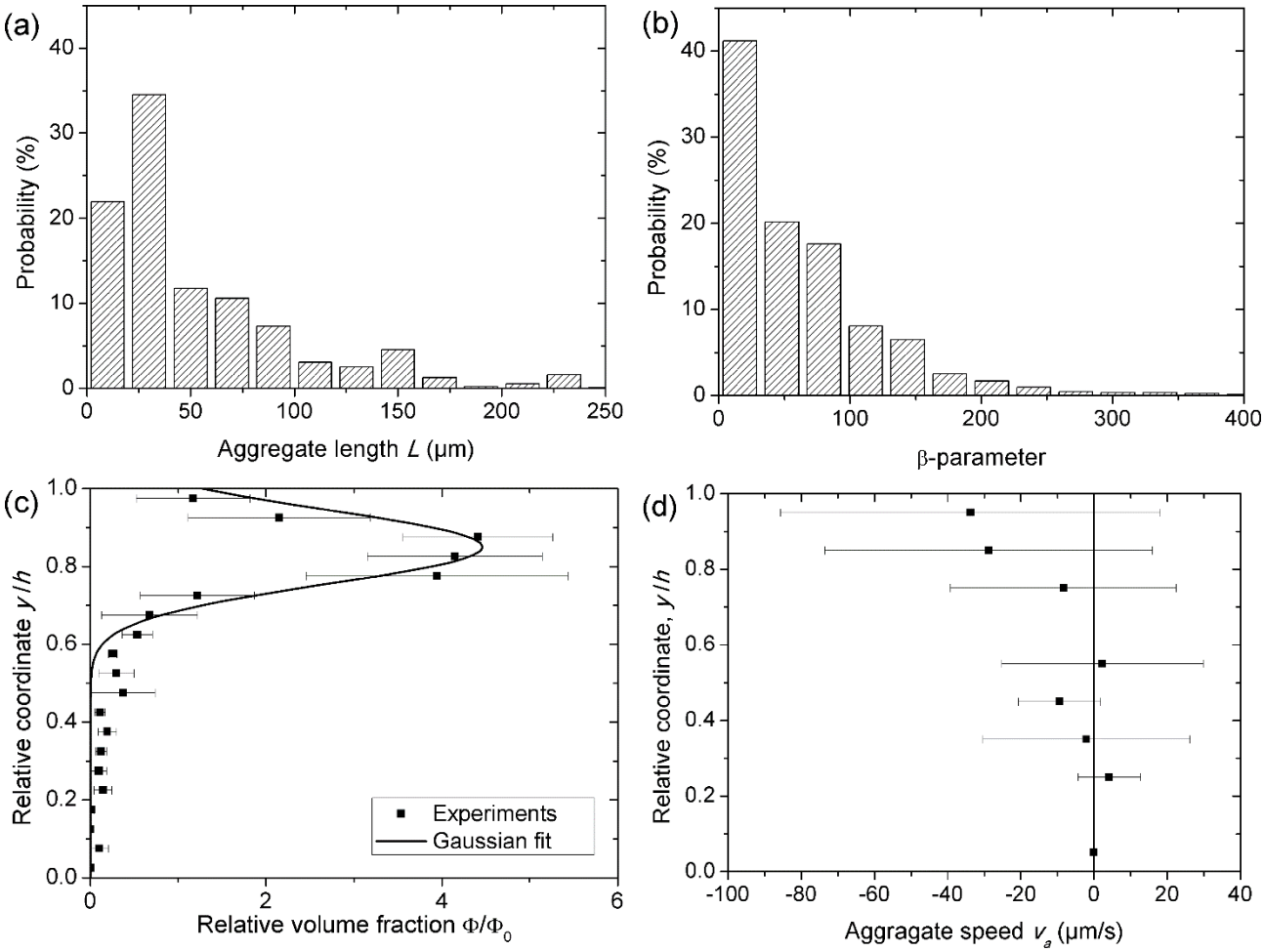

Figure 4.2: Experimental histograms of the aggregate length (a) and β-parameter (b) distributions. Experimental profiles of the aggregate volume fraction (c) and aggregate translational speed (d) across the channel y-dimension. The solid line in (c) stands for the Gaussian fit of the concentration profile with the adjustable parameters $\tilde{y}_0 = 0.85$ and $\delta = 0.067$.

Table 4.1: Values of experimental parameters intervening in velocity calculation

Parameter name	Value	Standard deviation
Aggregate length L (μm)	54	8
β-parameter	65	14
Aggregate volume fraction Φ_0	13×10^{-5}	5×10^{-5}
Channel width h (μm)	550	10
Field angular frequency ω (rad/s)	$2\pi \times 5$	0

The aggregate concentration profile $\Phi(y)$ across the channel was obtained through image processing, and it was normalised by the average value Φ_0, namely $\widetilde{\Phi}(\tilde{y}) = \Phi(y = \tilde{y}h)/\Phi_0$. The experimental profile $\widetilde{\Phi}(\tilde{y})$ is represented by dots in Fig. 4.2c, while the error bars correspond to the standard deviation between six measurement series. As observed in the

snapshot of Fig. 4.1a, the concentration profile is non-uniform: the aggregate volume fraction remains near zero in the front part of the channel at $\tilde{y} \lesssim 0.6$; it shows an abrupt increase at $0.6 \lesssim \tilde{y} \lesssim 0.85$ followed by a decrease near the back wall at $0.85 \lesssim \tilde{y} < 1$. This last decrease is related to geometrical constraints. When spinning under a rotating field, the aggregates cannot penetrate the back wall, so the distance between their geometrical centres and the back wall cannot be smaller than the aggregate half-length. This creates a somewhat depletion layer near the back wall with a smaller aggregate volume fraction. For calculations of the velocity profile, we fitted the experimental concentration profile with a gaussian function (solid line in Fig. 4.2c), as follows:

$$\widetilde{\Phi}(\tilde{y}) = A \exp\left(-\frac{(\tilde{y}-\tilde{y}_0)^2}{(2\delta)^2}\right), \tag{4.11a}$$

$$A = \left[\delta\sqrt{\pi}\left(\mathrm{erf}\left(\frac{1-\tilde{y}_0}{2\delta}\right) + \mathrm{erf}\left(\frac{\tilde{y}_0}{2\delta}\right)\right)\right]^{-1}, \tag{4.11b}$$

where $\mathrm{erf}(X)$ stands for the error function of X; the value of the normalisation constant A is chosen to respect the particle conservation condition [Eq. (4.5b)]; and the fitting parameters $\tilde{y}_0 = 0.85$ and $\delta = 0.067$ represent the position of the Gaussian peak and the distribution width, respectively. This concentration profile gives the following expression for the constant K_n [Eq. (4.7d)] (exact at a relative error of $\sim \exp(-4\pi^2) \sim 10^{-17}$) intervening in the velocity profile calculation:

$$K_n \approx \frac{2\delta}{\sqrt{\pi}} A \sum_{k=1}^{\infty} \left\{\frac{k \exp(-k^2/4)}{k^2-(2\pi\delta n)^2}\left[\sin\left(\frac{k\tilde{y}_0}{2\delta}\right) + (-1)^n \sin\left(\frac{k(1-\tilde{y}_0)}{2\delta}\right)\right]\right\}. \tag{4.12}$$

Let us now inspect the velocities of the aggregate translation along the channel axis obtained through image processing, detailed in Sec. 2.5.3. The average aggregate speed is plotted in Fig. 4.2d as a function of the relative coordinate $\tilde{y}$. The error bars correspond to the standard deviation between six recorded movies. The errors appear too large because of some chaos in the translational motion of spinning aggregates induced by interactions with neighbouring aggregates. Indeed, it is often observed that the geometrical centre of an aggregate spins around a neighbouring larger aggregate. Our image processing procedure perceives this as a reciprocal translation of aggregates with significant positive and negative speeds. Despite this artefact, the velocity profile in Fig. 4.2d agrees with the visual observations: the aggregates globally exhibit a leftward translation in the back part of the channel, at $0.7 \lesssim \tilde{y} < 1$. However, their translational speed $v_a \sim 30\ \mu\mathrm{m/s}$ is far below the value $\omega L/2 \approx 850\ \mu\mathrm{m/s}$ expected for rolling motion without slip. It is well below the speed, $\sim 0.5\ \mathrm{cm/s}$ of the dense nanoparticle clouds composed of rotating aggregates in experiments

of Pernal et al. (2020); Willis et al. (2020). This should be because of the considerable difference in characteristic sizes of millimetres-scaled clouds in those studies and micron-scaled individual aggregates in the present work, knowing that the magnetic force scales with a cube of the characteristic size. At the same time, the translational speed of our aggregates is a few times higher than that of the entire suspension. This likely indicates that the aggregate translational motion results from the interplay between the convection along the main flow and hydrodynamic interaction with the back-channel wall. Because of solid data dispersion, we have not achieved any clear dependence between the aggregate speed and aggregate length.

4.3.2 Velocity profiles

Let us track back to the single-phase description of the magnetic colloid and focus on the velocity profiles of the recirculation flow in the closed microchannel, recalling that experimental and theoretical profiles describe the effective velocities of the whole colloid without distinguishing aggregate motion from the suspending fluid motion. An example of the velocity vector field obtained for a moment $t = 150\,\mathrm{s}$ elapsed from the moment of the magnetic field application is shown in Fig. 4.3. It is clear from this figure that the velocity field is, in general, strongly perturbed by the presence of rotating aggregates provided that their length is only a few times smaller than the channel width, as also seen in the size distribution [Fig. 4.2a]. One observes clockwise flow vortexes within the area swapped by the aggregate clockwise rotation. Interference between the vortexes created by neighbouring aggregates gives a rather complicated flow pattern. However, one clearly distinguishes a regular rightward flow in the channel's front layer free of aggregates. As already discussed, this rightward flow arises to compensate for the leftward one induced by the aggregate translation along the back wall.

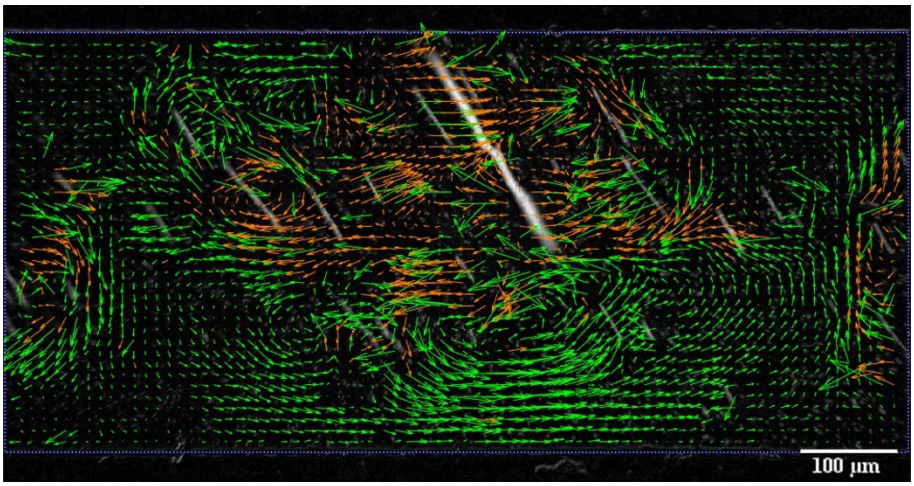

Figure 4.3: Velocity vector field deduced from the PIV analysis taken at the moment $t = 150\ s$. The coloured arrows stand for the velocity vectors whose x and y components enter (green arrows) the 10×5 px/frame window or lie outside this window (brown arrows). White thin rods stand for the position of aggregates, within which the instantaneous velocity profile cannot be established.

To smooth the effects of the flow irregularities introduced by rotating aggregates, the longitudinal (x-) component of the velocity profiles were averaged over either the observation window length l or observation period T, with the respective average magnitudes $\langle v_x(y,t)\rangle_l$ or $\langle v_x(x,y)\rangle_T$ defined in Sec. 2.5.2, with the time t being counted from the beginning of the steady-state regime, thus 100 s after the moment of the magnetic field application. The experimental colourmaps of the $\langle v_x(y,t)\rangle_l$ and $\langle v_x(x,y)\rangle_T$-dependencies are shown in Fig. 4.4a and b, respectively. First, we observe a recirculation flow in both these figures: the back layer (upper half of the colourmaps) exhibits the leftward flow with negative longitudinal speeds, and the front layer (lower half of the colourmaps) shows a rightward flow with positive speeds. Second, a few white-coloured vertical bands sometimes appear in the spatiotemporal colourmap $\langle v_x(y,t)\rangle_l$ [Fig. 4.4a]. These bands correspond to near zero velocity and point out the recirculation flow's go-and-stop (or rather fast and slow) sequence. This sequence visually corresponds to the fluctuation of the aggregate amount (or rather an instantaneous volume fraction $\Phi_0(t)$) in the observation window: smaller Φ_0 results in slower recirculation, higher Φ_0 result in stronger flows, in agreement with Eq. (4.10). However, excluding these fluctuations from consideration, we can claim that the steady state velocity profile globally holds for the whole analysed period of 200 s starting from the beginning of the steady-state regime until the end of the experiment. Third, the spatial colour maps $\langle v_x(x,y)\rangle_T$ in Fig. 4.4b show the velocity field averaged over time is globally independent of the longitudinal coordinate with some fluctuations likely appearing as a subsequently relatively small number of aggregates per observation window, increasing dispersion of the statistical averaging.

Independence of the velocity profile on x is likely ensured thanks to the fact that the observation window is central to the channel centre, and it is a few times shorter than the channel's full length, such that the fringing effects from the left and the right borders of the channel are not perceived.

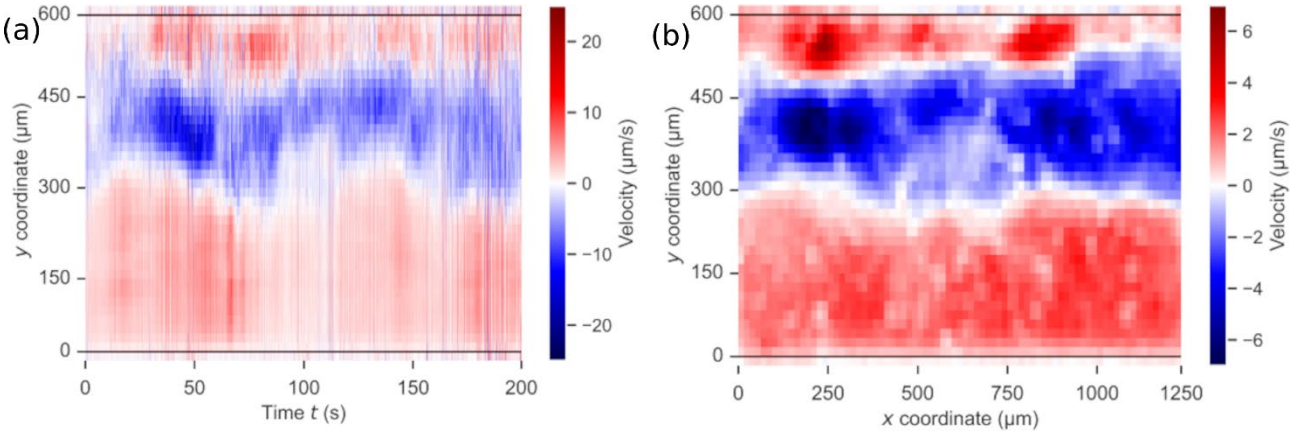

Figure 4.4: Spatiotemporal $\langle v_x(y,t)\rangle_l$ (a) and 2D spatial $\langle v_x(x,y)\rangle_T$ (b) experimental velocity maps averaged over one of six movies. The red and blue colours stand respectively for the rightward and leftward flows.

Finally, let us consider the velocity profiles $\langle v_x(y)\rangle_{l,T} \equiv \langle v\rangle(y)$ averaged over time and length of the observation window, as detailed in Sec. 2.5.2. Such averaging allows smoothing longitudinal and temporal fluctuations and focuses on the net effect of the rotating magnetic field on generated recirculation flows. The experimental averaged velocity profiles $\langle v\rangle(y)$ are compared with the calculated ones in Fig. 4.5. Points correspond to the data averaged over six experimental runs, with the velocity profiles averaged over two image stacks (corresponding to two orthogonal aggregate orientations) of each run. Solid lines correspond to the upper and the lower limits of the calculated profile, which were obtained as $v_{up} = v(1+\varepsilon)$ and $v_{low} = v(1-\varepsilon)$, where $v = \langle v\rangle(y)$ is the velocity profile calculated using Eqs. (4.7), (4.10b), (4.12) using the average experimental values of β, Φ_0, h, and $\varepsilon = ((\Delta\beta/\beta)^2 + (\Delta\Phi_0/\Phi_0)^2 + (\Delta h/h)^2)^{1/2}$ is the relative velocity error evaluated using experimental standard deviations $\Delta\beta, \Delta\Phi_0, \Delta h$ of β, Φ_0, h [cf. Table 4.1].

As inferred from this figure, both experimental and theoretical velocity profiles reflect recirculation flows. In the close vicinity to the back wall, $0.85 \lesssim \tilde{y} < 1$, a distinguishable rightward flow is observed in experiments and confirmed by the model. This flow is likely associated with the propulsion of the fluid layer to the right along the wall by the aggregates spinning in a clockwise direction. In the region still situated in the back part of the channel but further from the wall, $0.5 \lesssim \tilde{y} \lesssim 0.85$, an intense leftward flow is observed and physically corresponds to the aggregates translating along the wall and "sucking" the ambient fluid with

them. However, notice that this leftward motion is predicted in the frame of the single-phase model without considering aggregate motion but rather the effective motion of the whole colloid. The front layer of the channel, $0 < \tilde{y} \lesssim 0.5$ exhibits an intense rightward flow. As pointed out, this layer is almost free of aggregates [cf. Fig. 4.2c] The rightward flow arises to compensate for the left in the back layer. By integrating the experimental velocity profile, we have checked that the zero total flux condition is satisfied at a maximal error of 1% (as regards the rightward or leftward flux). Notice that experimental data fit rather well into the confidence interval of the theoretical model (the shaded region between the two solid lines in Fig. 4.5), considering that the model is entirely free of adjustable parameters. This could be an argument for the validity of the single-phase approach used in our model.

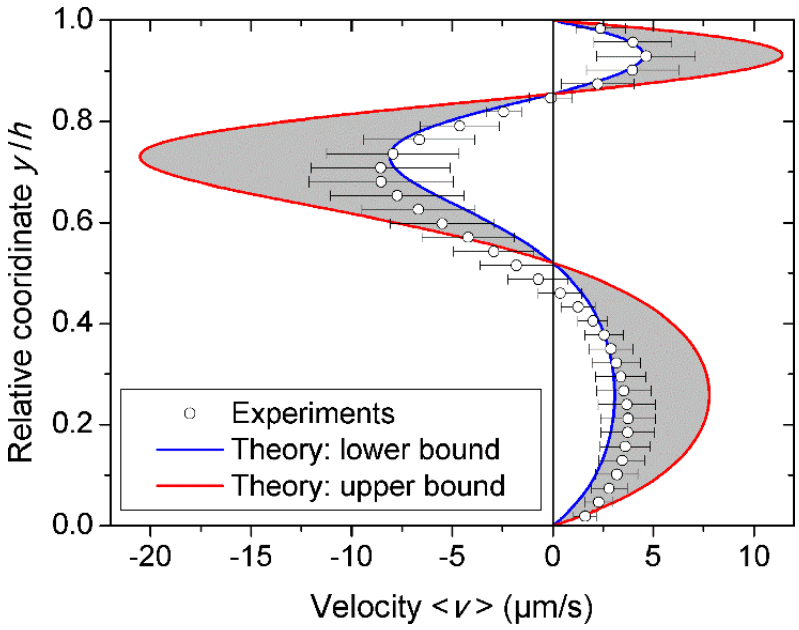

Figure 4.5: Experimental (symbols with error bars) and theoretical (solid lines) velocity profiles $\langle v_x(\tilde{y})\rangle_{l,T} \equiv \langle v\rangle(\tilde{y})$ averaged over time and length of the observation window. The shaded region encompasses the region of the model validity.

It could be interesting to provide some quantitative characteristics of the recirculation flow from the application perspective. The rightward and leftward velocities achieve a maximal absolute value of about 5 and 9 μm/s, respectively; the leftward (equal to rightward) flow rates achieve 2.35×10^5 $\mu m^3/s$, with the average rightward and leftward speeds of 3 and 5 μm/s, respectively. Projecting these results to the clot dissolution application, we constate that these speed levels are about an order of magnitude higher than an effective speed (~ 0.8 μm/s) of the diffusive transport of the streptokinase thrombolytic drug through the blocked blood vessels [Clements (2016)]. Of course, the comparison should be carried out for equivalent channel sizes and fluid viscosities. It is, therefore, instructive to analyse the effect of different parameters on

the recirculation intensity. According to Eq. (4.10), the flow speed scales as $v \sim \beta\omega\Phi_0 h$. First, the recirculation is expected to be a few times more intense in millimetric-sized channels than in the present experimental channel with a width of $h \sim 500$ μm. Second, the aggregate volume fraction Φ_0 has been found to increase linearly with the nanoparticle volume fraction φ_0 [Ezzaier et al. (2017)], such that one may increase the recirculation speed by increasing φ_0 above the actual experimental value of 1.6×10^{-3}. Of course, there should be certain constraints on the maximal admissible nanoparticle concentration in the actual application. Third, at first glance, the recirculation speed is linear in the magnetic field frequency ω but independent of the field amplitude H and suspending liquid viscosity η_0. However, the aggregates collide and fragment into smaller pieces during their spinning under a rotating magnetic field. Their final size, or rather aspect ratio $r = L/d$, has been determined to be affected by ω, H and η_0, as follows: $r \propto [\mu_0 H^2/(\eta_0\omega)]^{1/2}$. Thus, using the definition of the parameter β [Eq. (4.3b)] in the velocity scaling and neglecting the logarithmic term, we obtain $v \propto \mu_0 H^2/\eta_0$. This scaling holds in the limits $r \gg 1$, $Ma \gg 1$ and for the linear aggregate magnetisation (low magnetic fields). Within these limits, the recirculation speed appears independent of the field frequency but quadratic in the magnetic field intensity and inversely proportional to the suspending liquid viscosity. Thus, to achieve the same recirculation intensity by changing the aqueous solvent ($\eta_0 \sim 10^{-3}$ Pa × s) by the human blood ($\eta_0 \sim 7 \times 10^{-2}$ Pa × s), one needs to apply the magnetic field amplitude of about $H \sim 55$ kA/m at the same other conditions. More detailed studies coupling the hydrodynamic effects with the blood clot dissolution are required to validate the feasibility of this technique, and we will somehow check them in the next Chapter 5 on the model of the alginate bead dissolution.

Another essential feature of the observed recirculation flow is the duration of the steady-state regime, which starts at the time $t \gtrsim 100$ s from the moment of magnetic field application. As already mentioned, because of the heating of electromagnets, we were unable to determine with confidence the end of the steady state in experiments; we know that it lasts for at least 200 s from its beginning. However, we observe that the aggregates migrating to the left along the back wall does not come back but are accumulated near the left end of the channel once they arrive there. We can anticipate the end of the recirculation flow when most of the aggregates have moved to the left end, which is expected to occur at the timescale, $\tau \sim l/v_a \sim 130$ s, where we have taken an average aggregate speed $v_a \approx 15$ μm/s [Fig. 4.2d]. This time is likely underestimated because the "disappearance" of some aggregates can be, in principle, compensated by the appearance and growth of other aggregates. Indeed, a previous study has

revealed that, in the absence of macroscopic flows, the aggregates stop appearing when the supersaturation is still high, and this is likely because of strong repulsive dipolar interactions between them significantly hampering the evolution to the equilibrium state [Ezzaier et al. (2017)]. Removing the aggregates from a major channel part can likely trigger a new nucleation/aggregate growth sequence. However, longer experimental observations with careful observation of the aggregate fate are required to confirm or decline this hypothesis.

4.4 Conclusion

This chapter focuses on the generation of the recirculation flows of a magnetic colloid within a closed microfluidic channel via the application of an external rotating magnetic field. The magnetic colloid consists of iron oxide magnetic nanoparticles dispersed at a volume fraction $\varphi_0 = 1.6 \times 10^{-3}$ in an aqueous sodium citrate solution and slightly destabilised by the partial screening of electrostatic repulsion between nanoparticles. Upon magnetic field application, the colloid undergoes reversible phase separation, and the field-induced aggregates synchronously rotate with the magnetic field (as already shown in Chapter 3) and can generate macroscopic flows under certain conditions. The main results of the present Chapter can be summarised as follows:

1. In a closed channel, macroscopic recirculation appears due to the combination of the synchronous rotation of aggregates and the asymmetry of their concentration profile across the channel. The required concentration gradient is easily obtained by super-positioning a weak magnetic field gradient to the homogeneous rotating magnetic field. Remarkably, we have never managed to reach recirculation in either a homogeneous rotating field or in a stable magnetic colloid free of field-induced phase separation. Thus, the claimed mechanism is qualitatively different from those revised in Sec. 1.2.3 and responsible for the vortex flows generated in a cylindrical vessel with a perfectly stable ferrofluid (interplay between magnetisation relaxation and diffusion of the internal angular momentum [Zaitsev and Shliomis (1972); Shliomis (2021)] or in a suspension of magnetic microparticles subject to triaxial fields (3D mixing by complex percolated field-induced structures [Martin (2013)]. Quantitatively, we achieve recirculation flows at low-frequency fields (5 Hz) and low particle concentration $\varphi_0 = 1.6 \times 10^{-3}$ as opposed to the ferrofluid rotation in the cylindrical vessel. On the other hand, we do not need any branched percolated structures to generate the flow.
2. The generated flow pattern is relatively simple and physically understandable. The magnetic field gradient orthogonal to the main channel axis and oriented towards one of the channel walls makes the aggregate "concentrated" near this (first) wall, but any sticking is

avoided by short-ranged hydrodynamic repulsion from the wall. The spinning aggregates propel the ambient fluid in their rotation directions, thus creating a weak flux in one direction in close vicinity to the channel wall and a more substantial flux in the opposite direction further from the wall. To compensate for the difference between these fluxes, a third flux appears near the opposite (second) wall in the same direction as the weak flux near the first wall. The PIV technique quantitatively measured the experimental velocity profiles, which confirms the earlier arguments. The peak velocities values of the experimental velocity profiles are on the order of $v{\sim}10\ \mu\mathrm{m/s}$ within the channel of a width of $h{\sim}500\ \mu\mathrm{m}$ at the magnetic field amplitude and frequency of $H \approx 6\ kA/m$ and $\omega = 2\pi \times 5$ rad/s (5 Hz), respectively.

3. A theoretical model based on the solution of the momentum balance equation completed with a magnetic torque term allows excellent quantitative agreement with experimental velocity profiles without adjustable parameters. The model employs a single-phase description of the magnetic colloid, with the aggregates considered only implicitly through their rotational friction coefficient and macroscopic concentration profile. Thus, the model captures the observed flow pattern through the macroscopic magnetic torque density variation across the channel rather than through the flow fields generated by asymmetrically placed spinning aggregates. Combined with the results on the steady-state aggregate size under rotating fields [Chapter 3], our model predicts the following scaling of the flow velocity with the governing parameters of the system: $v{\sim}\varphi_0\mu_0 H^2 h/\eta_0$ with the field frequency ω ruled out from v because of the two counterbalancing effects: (a) increase of the aggregate angular speed with ω, and (b) decrease of the aggregate length with ω.

From the application perspective, we achieve the recirculation velocities on the order of 5-10 μ/s and the rightward (or leftward) flow rates of about $2 \times 10^5\ \mu\mathrm{m}^3/\mathrm{s}$, the values being an order of magnitude higher than those related to the diffusive transport of the streptokinase thrombolytic drug through the blocked blood vessels. We warrant, however, that this comparison should be handled with care because of the different viscosities and channel sizes in both cases. The genuine biochemical system of the target application (fibrin clots, blood medium, etc.) is still too far from our scientific approach. However, the present Chapter allows us to establish a solid physical insight into the problem of field-induced flow generation, and we are tempted in the next Chapter 5 to check whether we manage to accelerate the mass transport and a "clot" dissolution on the experimental model of alginate bead that "replaces" the blood clot of the future system.

Chapter 5. Field-enhanced mass transport and polymer bead dissolution

In this chapter, we are aimed to reply to the last question related to the target biomedical application and formulated in Sec. 1.3: will the recirculation in a clotted vessel, once induced, be sufficiently intense to be able to rapidly deliver the thrombolytic drug towards the clot and dissolve it faster compared to the lysis rate provided by diffusion-limited drug transport without recirculation? For this purpose, we used a simple, reproducible model for the system. A microfluidic channel is used as a proxy for a blood capillary, with a width of 1 mm and a thickness of 300µm (see fig 2.6). The clot is likened to a bead of calcium alginate gel which citrate ions can dissolve in solution. On the one hand, this experimental model simplistically simulates at the extreme the fibrinolytic drug cation in a physiological system. On the other hand, the geometry and the physicochemistry of this system are close to those used in the previous Chapters, such that we can directly correlate the results on the intensity of the field-induced flow recirculation for interpretation of the convective mass transport of the citrate ions and dissolution of the alginate bead provoked by them. We firstly report the experimental results in Sec. 5.1. Then, in Sec. 5.2, we present a theoretical model of the convective mass transport and the bead dissolution and qualitatively compare experimental results to the model predictions. Finally, we present an extrapolation of the obtained results on the blood clot dissolution in Sec. 5.3. The conclusions of this chapter are drawn in Sec. 5.4.

5.1 Experimental results

5.1.1 Interaction between citrate ions and calcium alginate

Before analysis of the alginate bead dissolution in the microfluidic channel, let us briefly inspect the physicochemical mechanism of this dissolution. According to Roger et al. (2006), citrate can dissolve an alginate gel. This is due to the specific structure of the gel. First, when the sodium alginate precursor is in contact with the calcium ionic bath [Sec. 2.3.3, Fig. 2.2], sodium alginate molecules create ionic bonds with calcium ions in the cross-linking bath during the manufacturing process. This is translated by the gelation reaction schematised in Fig.5.1.

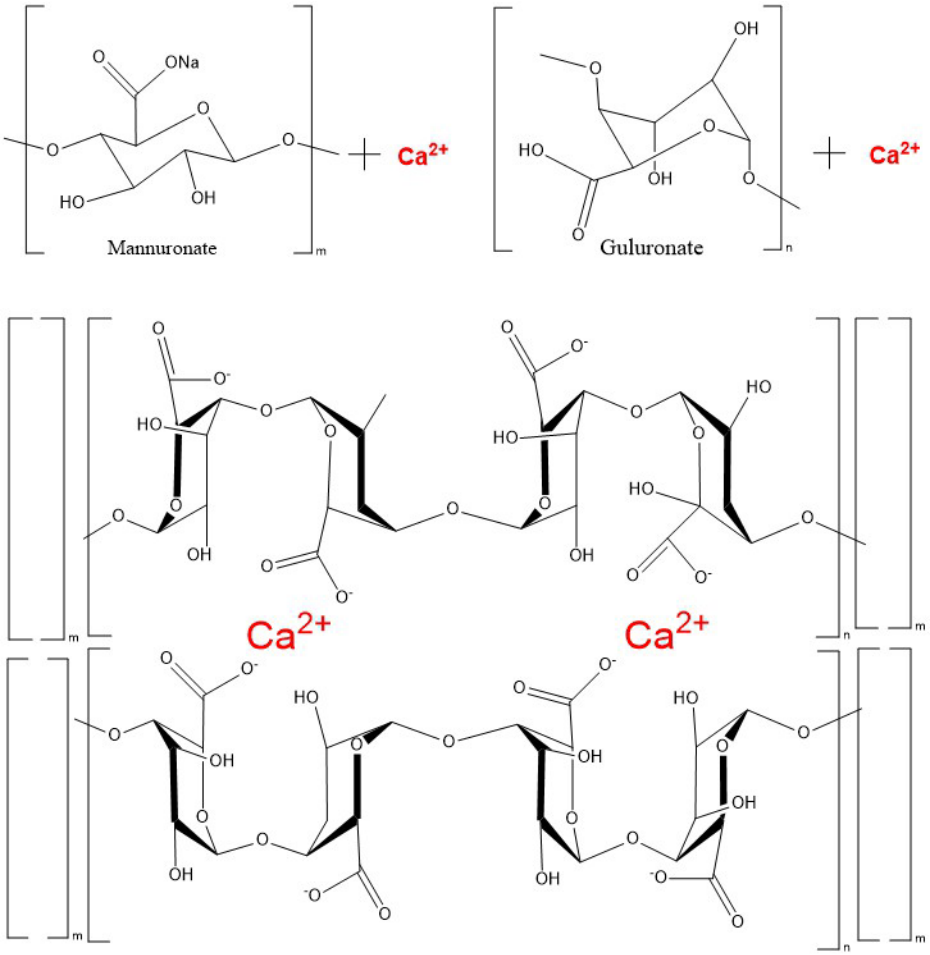

Figure 5.1: The formation mechanism for calcium alginate. Sodium alginate $(NaC_6H_7O_6)_{sol}$ crosslinks with calcium chloride ($CaCl_2$) to generate calcium alginate $(C_{12}H_{14}CaO_{12})_{gel}$. The two chemicals are rearranged, so they bond (like the eggbox model) to form a gelatinous substance.

Two alginate chains are thus linked to the same calcium ion. However, trisodium citrate $Na_3C_6H_5O_7$ has three carboxylic sites, which make the chelation with the calcium ions of the gel. Therefore, when citrate is added in contact with alginate gel, it captures the calcium ions, which causes the gel to dissolve by breaking the bonds between alginate chains. This dissolution corresponds to the reaction:

$$3Ca^{2+} + 2Ci_3^- \rightarrow Ca_3Ci_2, \tag{5.1}$$

as proposed by Delaney et al. (2010) and schematised in Fig. 5.2.

The reaction (5.1) assumes that all three carboxylic groups of the trisodium citrate are deprotonated. However, at our experimental conditions with pH~5.5, only about two of three carboxylic groups are deprotonated, so the complexation of calcium by citrate ions likely goes according to the reaction:

$$Ca^{2+} + Ci^{3-} \rightarrow CaCi^-, \tag{5.2}$$

which highlights that at the considered pH and moderate calcium concentration, one calcium binds two carboxylic groups of the trisodium citrate, while the third group remains rarely bound, avoiding polymerisation of trisodium citrate entities into calcium citrate gel. Once the alginate chemistry is achieved, let us characterise the alginate bead dissolution process through the diminution of its surface, or rather its horizontal cross-section.

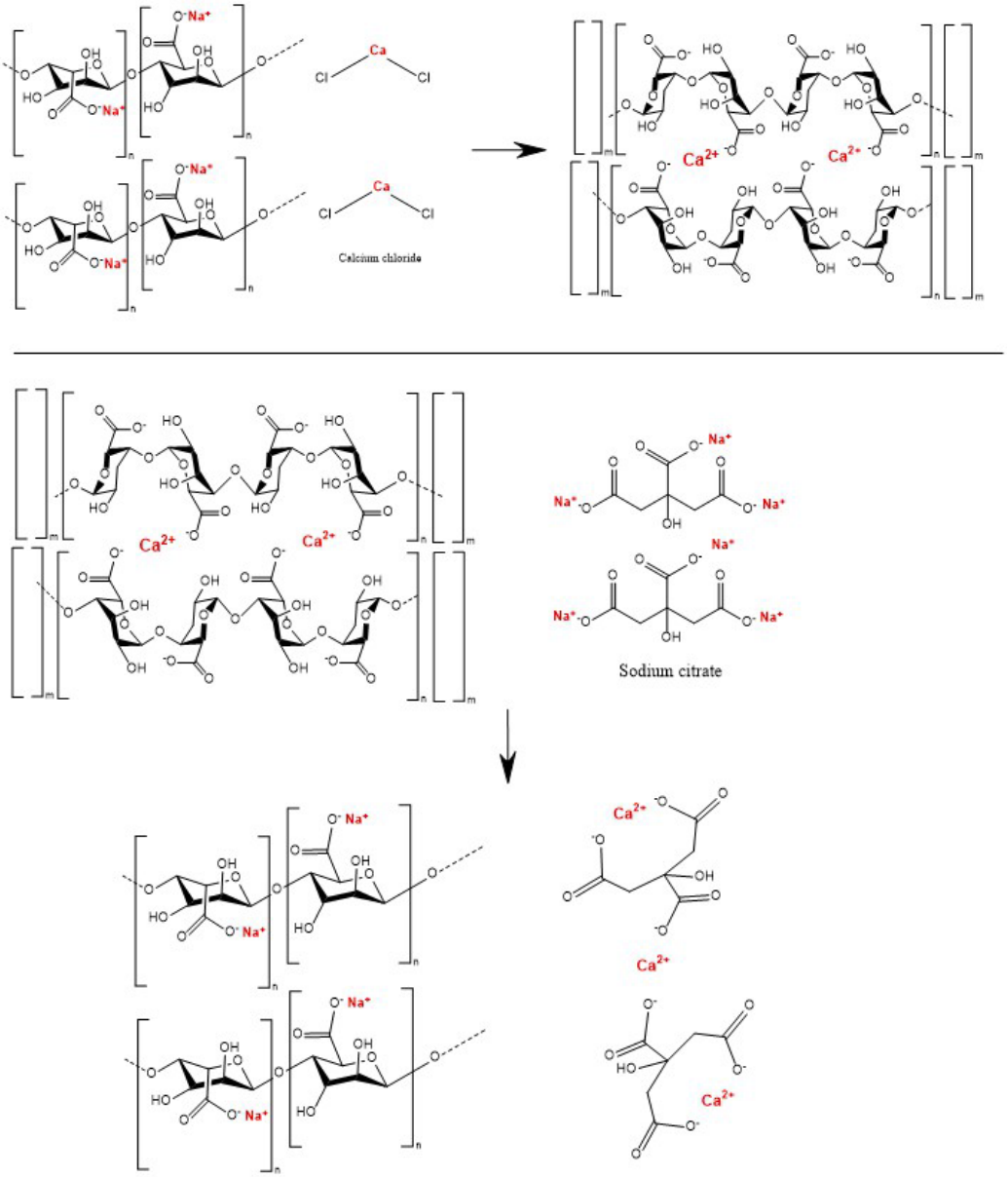

Figure 5.2: Reversible cross-linking of alginate by dications: during the cross-linking, calcium forms highly stable complexes with alginate to form networks, while during the reversal, a competing ligand such as sodium citrate chelates with calcium, and the cross.

5.1.2 Monitoring of the bead surface

As described in Sec. 2.4.3, in experiments, we place a calcium alginate bead into a microfluidic channel [Fig. 2.6] inject the magnetic colloid and clip the channel so that the squeezed alginate bead separates the channel into two compartments on each side of the bead. Then, we applied a rotating magnetic field at 5 Hz and 6.4 kA/m amplitude with a slight gradient along the y-axis [Sec. 2.4.4, Fig. 2.5] and generate the recirculation flow of the magnetic colloid within the channel, as analysed in detail in Chapter 4. The dissolution of the alginate bead is recorded, and the obtained snapshots are presented in Fig. 5.3 for one of four experimental runs with and without the magnetic field.

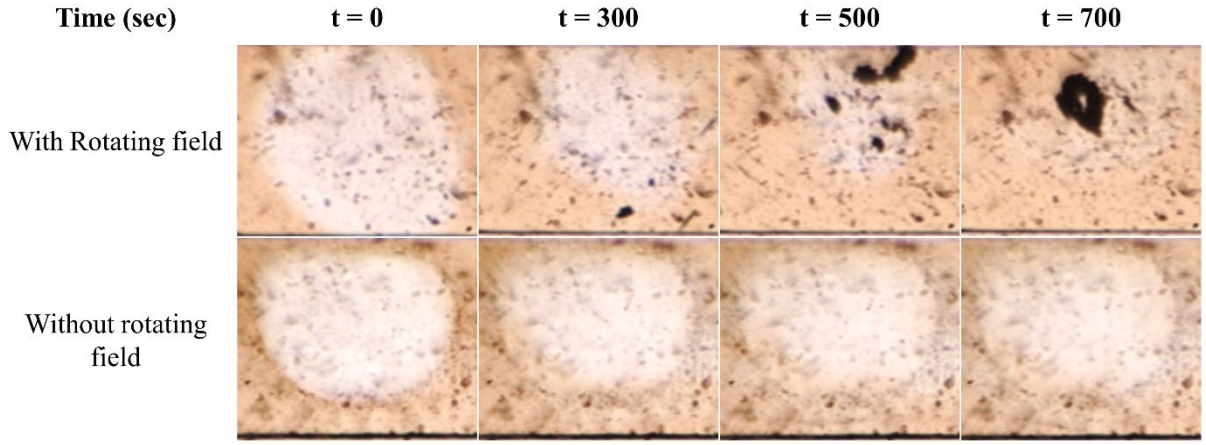

Figure 5.3: Snapshots of the alginate bead dissolution in the microfluidic channel in the rotating magnetic field's presence and absence.

We observed the disaggregation of the alginate bead during the first 10 minutes of the experiment when the recirculation flux was induced, whereas it never occurred during the same duration when the magnetic field was turned off. To quantify this phenomenon, we proceed to track the bead's surface variation over time thanks to the ImageJ software. Figure 5.4 shows the average over 4 experiments of the normalised surface S_n introduced in Eq. (2.5). We found the time the bead's surface was halved, t = 310±5 sec, and after 700 sec, the bead was largely dissolved. However, a small alginate deposit was still observable on the bottom of the microfluidic channel, which gave the relative surface $S_n(700\ \mathrm{s}) \approx 0.33$. It was observed that starting from about 300 s, the bead lost contact with one of the walls (upper or down) and its dissolution (in terms of the relative surface) was slowed once the liquid gap between the bead surface and the channel wall was formed. This deceleration of the decrease of the relative surface is well observed by the change of the slope at $t \sim 300$ s in Fig. 5.4. However, at elapsed times $t \gtrsim 700\ s$, the bead detached from another channel wall and became spinning swiftly (presumably with the field frequency) in the direction of the magnetic field rotation thanks to

magnetic particle aggregates adsorbed to the bead surface. After detachment, we observed a speedy dissolution of the spinning bead (thanks to strongly enhanced convective fluxes towards the spinning bead). Unfortunately, the spinning bead hurried along the channel and exited the observation window, so it was impossible to quantify the dissolution rate after detachment with confidence. In the absence of a magnetic field, the dissolution is much slower, and the bead achieves the relative surface $S_n \approx 0.94$ at $t = 1200$ s.

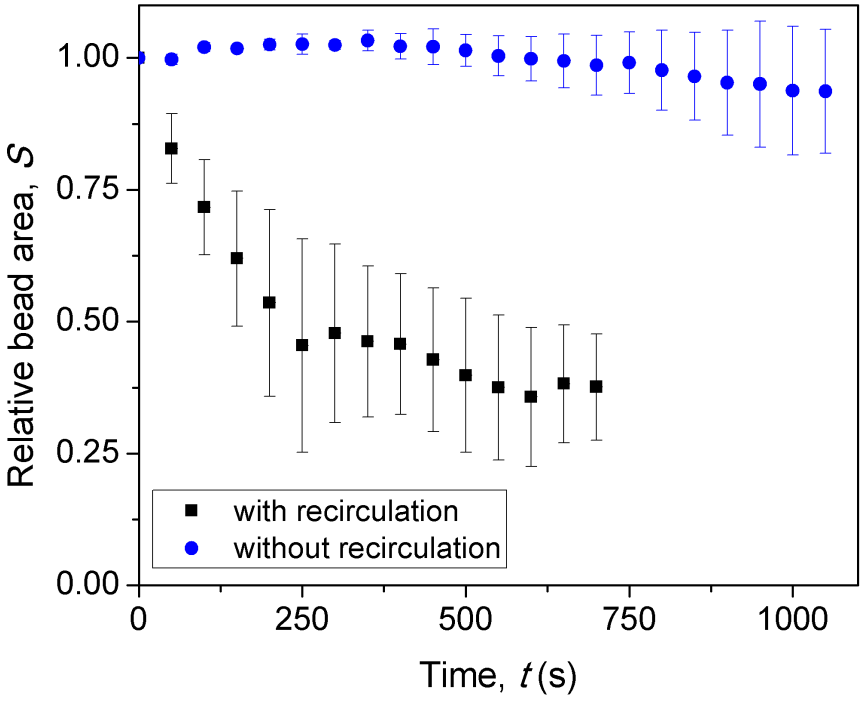

Figure 5.4: Evolution of the relative surface of the alginate bead with time as a signature of the dissolution process in the presence (black squares) and the absence (blue circles) of the applied rotating magnetic field.

This difference between the two curves can be explained as follows. In both cases, the neighbouring sodium citrate molecules chelate the calcium cross-linking ions, which re-solubilises the alginate according to Fig. 5.2. However, in the case of the induced recirculating flow, the latter constantly renews the depleted layer with new unbound sodium citrate molecules and evacuates the product of the bead dissociation – the alginate chains. Such convective transport is expected to enhance the bead dissolution compared to the purely diffusive transport of sodium citrate ions and dissolution products dictated by the concentration gradients. It is also possible that in the case of recirculating flow, the bead dissolution is even more accelerated by the hydrodynamic stresses on the bead surface, dislodging loose soluble alginate polymer strands. To check this last scenario, we conducted supplementary experiments with a magnetic colloid composed of uncoated IONP dissolved in water at $pH \sim 5.5$ at the same volume fraction of 0.16% vol and not containing citrate ions. This magnetic colloid showed very similar

behaviour in the presence of the magnetic field: i.e. agglomeration into needle-like aggregates rotating synchronously with the field and generating a recirculation flow in the microfluidic channel. However, in the absence of sodium citrate, no bead dissolution or erosion has been observed during 700 s despite an intense recirculating flow. This allows us to exclude the scenario of erosion of the bead surface by the hydrodynamic stresses.

Finally, it is worth mentioning that depending on the pore size of the calcium alginate beads' matrix and the trisodium alginate concentration in the vicinity of the beads; the bead dissolution can occur either on the surface of the bead or in the bead if citrate ions can diffuse inside. We observed both behaviours in our experiments, at least in the case without recirculating flux. A slight dilatation of the bead at short times (observed in Fig. 5.4, as well as in the snapshots of Fig. 5.5) likely means that the calcium alginate is progressively dissolved within the bead in the absence of the magnetic field through either/both release and diffusion of calcium ions outside the bead or/and diffusion of citrate ions capturing calcium inside the bead.

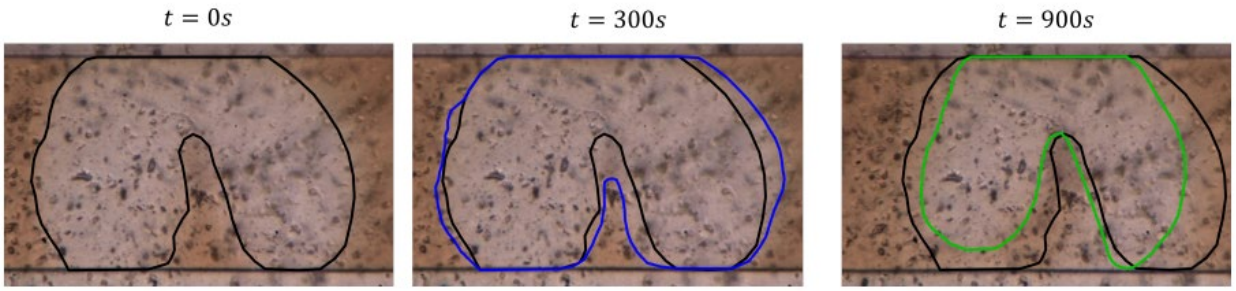

Figure 5.5: Experimental demonstration of the slight bead dilatation at short times followed by surface dissolution at longer times in the absence of the field-induced recirculation. In all snapshots, the black line shows the initial bead contour; the blue and green lines show the contour positions at 300s and 900s, respectively.

However, we believe that dissolution at the bead surface remains the dominant mechanism at least for a long time (and in the case of recirculation flows) because it results in a more substantial decrease of the bead surface as compared to slight dilatation caused by the bulk dissolution process. Ignoring the bulk dissolution scenario, in the next section, we will try to make a theoretical prediction of the evolution of the bead size with time and compare it with experiments.

5.2 Theory and comparison with experiments

In this section, we tempt to provide a very approximate (semi-quantitative) prediction of the dissolution rate or dissolution time of the alginate bead in the two experimental cases: (a) purely diffusive molecular transport in the absence of the applied magnetic field (Sec. 5.2.2) and (b)

convective diffusion in the presence of the rotating magnetic field, which induces the flow recirculation (Sec. 5.2.3). To gain the very first physical insight, our calculations will be done at maximal (but still physically relevant) simplifications (described in Sec. 5.2.1) allowing us obtaining explicit mathematical expressions and scaling laws, along with a semi-quantitative comparison with experiments (Sec. 5.2.4).

5.2.1 Basic assumptions

Let us consider an alginate bead placed in the middle of the microfluidic channel, as shown in Fig. 5.6. Such a centered position (not always respected in experiments) should not alter the final results if the diffusive or convective processes occur at length scales shorter than the channel length.

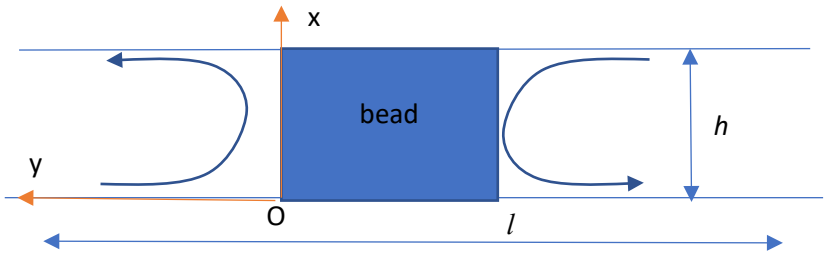

Figure 5.6: Problem geometry of a bead in the microfluidic channel.

For both cases mentioned above, (a) and (b) we will adopt the following considerations:

1) Once at the surface of the alginate bead, one citrate ion (bearing approximately two deprotonated carboxylate groups at a considered pH=5.5) can bind one calcium ion from calcium alginate according to the reaction described by Eq. (5.2). As a result, the alginate bead is supposed to be dissolved progressively by the detachment of single alginate chains rather than erosion of larger strands containing multiple chains.

2) Most important diffusive or convective processes defining the dissolution rate are the transport of citrate ions towards the bead and evacuation of the dissociated alginate chains from the bead surface toward the bulk citrated solution.

3) Normally, citrate ions can penetrate the alginate bead and bind Ca ions inside the bead, thus producing the bead dissolution in the whole volume of the bead. However, citrate transport through the cross-linked alginate network is believed to be relatively slow, and the bead dissolution is considered to happen only on its surface.

4) As in the case of many chemical reactions, the surface reaction rate of the citrate ions with a calcium alginate network is considered much higher than the diffusive or convective transport

of reagents. This implies that: (a) the bead dissolution is governed by the slowest timescale (diffusive or convection-diffusive); (b) since the reagent arriving at the bead surface (citrate ions) is "consumed" very quickly, its concentration at the surface is close to zero: $c_1(t, x, y = 0) \approx 0$ [Levič (1962)]; (c) since a fast reaction, the desorbed alginate chains do not have time to rearrange their conformation, the concentration of the desorbed alginate chains at the bead surface is supposed to be equal to the chain concentration in the bulk of the alginate bead: $c_2(t, x, y = 0) \approx 0.214$ mmol/L, as evaluated in Sec. 5.2.4.

5) If evacuation of the alginate chains from the bead surface is not sufficiently fast, this could hinder access of citrate ions towards the Ca bridges "hidden" by non-evacuated alginate chains. This could lead to the accumulation of citrate ions at the surface ($c_1(t, x, y = 0) \neq 0$) and should reduce the flux of citrate ions towards the bead. On the other hand, the release of alginate chains cannot be faster than transporting citrate ions toward the surface. If the transport of citrate ions is slow enough, a part of the alginate strands situated on the bead surface will not dissociate, and the surface concentration of the dissociated alginate chains will be lower than the total alginate concentration: $c_2(t, x, y = 0) < 0.214$ mmol/L. This will reduce the outward flux of alginate chains until it becomes equal to the citrate flux. We suppose, therefore, equality of the inward (citrate) and outward (alginate) fluxes, taking into account the stoichiometry of this exchange. If there are N Ca bonds per one alginate chain, we suppose that bringing $N/2$ citrate ions per unit time will statistically liberate one alginate chain. This imposes the following balance of molar fluxes (in mol/s) J_1 of citrate ions and J_2 of evacuated alginate chains:

$$J_1 = \frac{N}{2} J_2. \tag{5.3}$$

6) The bead is squeezed by the microfluidic channel's upper and lower walls (with a gap of 300 µm between both); its shape is no longer spherical. For maximal simplification, we will neglect any curvature of the bead surface and consider a parallelepiped shape with the Cartesian system of coordinates introduced in Fig. 5.6, which is different from that used in Chapter 4.

5.2.2 Purely diffusive transport

At the considered plain surface of the alginate bead, the diffusive transport of citrate ions and alginate chains happens only along the longitudinal y-axis. It is always unsteady and is described by the second Fick's law, taking the flowing 1D-form:

$$\frac{\partial c}{\partial t} = D \frac{\partial^2 c}{\partial y^2}, \tag{5.4}$$

where c and D are molar concentration and diffusivity of either citrate ions or alginate chains, both denoted from now on by subscript "1" and "2", respectively. This equation is subject to the following initial and boundary conditions, some of which have been postulated in Assumption (4) of Sec. 5.2.1:

$$\begin{cases} c_1(t=0,y) = C_1 \\ c_1(t,y=0) = 0 \quad \text{for citrate,} \\ c_1(t,y\to\infty) = C_1 \end{cases} \tag{5.5}$$

$$\begin{cases} c_2(t=0,y) = 0 \\ c_2(t,y=0) = C_2 \ \text{for alginate,} \\ c_2(t,y\to\infty) = 0 \end{cases} \tag{5.6}$$

where C_1 and C_2 are the molar concentration of citrate (far from the bead) and alginate chains (at the bead surface), respectively.

The solution of the initial-boundary value problem (5.4), (5.5) or (5.4), (5.6) is well known [see for instance Chhabra and Shankar (2018)], and we will directly write down the expression for the absolute value of the fluxes of citrate ions and alginate chains at the bead surface:

$$J_{max,i} = C_i\sqrt{\frac{D_i}{\pi t}}A, i = 1,2, \tag{5.7}$$

where A is the channel cross-section. Notice that Eq. (5.7) gives maximal values of the fluxes of citrate ions (subscript "1") or alginate chains (subscript "2"). For this reason, the fluxes are highlighted by the subscript "max". According to the possible accumulation of citrate ions, as discussed in Assumption (5), both maximal fluxes must be compared. If we find $J_{max,1} > \frac{N}{2}J_{max,2}$, the citrate ions will accumulate on the bead surface, and their concentration will become non-zero at the surface, say $C_1{}'$ and the citrate flux will decrease to $J_1 = (C_1 - C_1{}')\sqrt{\frac{D_1}{\pi t}}A$ in order to get equal to the flux $\frac{N}{2}J_2$ of evacuated alginate chains, according to Eq. (5.3). On the contrary, if we find $J_{max,1} < \frac{N}{2}J_{max,2}$, this means that the alginate chains are evacuated faster than they are desorbed from the bead surface. This implies that the bead surface will contain some amount of non-desorbed alginate chains, and the concentration of the detached chains, say $C_2{}'$ will be lower than the total alginate concentration C_2 in the bulk of the bead. In such a way, the alginate flux will decrease to $J_2 = C_2{}')\sqrt{\frac{D_2}{\pi t}}A$ until it becomes equal to

the citrate flux, as stipulated by Eq. (5.3). In both considered cases, both real (not maximal) fluxes are equal between them and are defined by the minimal value between $J_{max,1}$ and $\frac{N}{2}J_{max,2}$:

$$J_1 = \frac{N}{2}J_2 = \min(J_{max,1}; \frac{N}{2}J_{max,2}). \tag{5.8}$$

According to Eq. (5.7), we finally get the following expression for the desorption rate of alginate chains:

$$J_2 = \begin{cases} J_{max,2} \text{ if } \frac{2C_1}{NC_2}\sqrt{\frac{D_1}{D_2}} > 1 \\ \frac{2}{N}J_{max,1} \text{ if } \frac{2C_1}{NC_2}\sqrt{\frac{D_1}{D_2}} < 1 \end{cases} \tag{5.9}$$

During the dissolution process, the free citrate ions (not bounded by calcium) are constantly consumed, while the alginate chains are constantly released. This can change the concentrations C_1 and C_2 at the time, in which case the expression (5.7) is, strictly speaking, no longer valid. However, we show that at elapsed times shorter than $t \sim \frac{l^2}{D} \sim 10^5$ s, this effect can be neglected, as in the present experimental case (here, $l \approx 10$ mm is the channel length).

Finally, the decrease of the bead volume with time can be obtained by balancing the rate of the decrease of the number of moles of alginate to the desorption rate of alginate:

$$C_2 \frac{dV}{dt} = -2J_2, \tag{5.10}$$

where factor 2 is introduced into the right-hand side of Eq. (5.10) to consider the dissolution from both sides of the bead. Combining with (5.9) and integrating over time, we get the following equation of the evolution of the bead volume:

$$V(t) = \begin{cases} V_0 - 4\sqrt{\frac{D_2 t}{\pi}}A \text{ if } \frac{2C_1}{NC_2}\sqrt{\frac{D_1}{D_2}} > 1 \\ V_0 - \frac{8C_1}{NC_2}\sqrt{\frac{D_1 t}{\pi}}A \text{ if } \frac{2C_1}{NC_2}\sqrt{\frac{D_1}{D_2}} < 1 \end{cases} \tag{5.11}$$

showing a smooth decrease of the bead volume with time. The ratio of the bead volume at a given time t to its initial value is equal to the relative bead surface S_n (cf. Sec. 5.1.2, Fig. 5.4) and directly follows from Eq. (5.11):

$$S_n(t) = \frac{V(t)}{V_0} = \begin{cases} 1 - \frac{4}{l_b}\sqrt{\frac{D_2 t}{\pi}} \text{ if } \frac{2C_1}{NC_2}\sqrt{\frac{D_1}{D_2}} > 1 \\ 1 - \frac{8C_1}{NC_2 l_b}\sqrt{\frac{D_1 t}{\pi}} \text{ if } \frac{2C_1}{NC_2}\sqrt{\frac{D_1}{D_2}} < 1 \end{cases} \quad (5.12)$$

where l_b is the initial bead dimension along the channel (effective length).

5.2.3 Convective diffusion

First, we have to evaluate whether the recirculating flow generated by the rotating magnetic field is strong enough to enhance the molecular transport toward and out of the alginate bead surface. We will therefore evaluate a characteristic ratio of the convective and diffusive fluxes referred to as the Péclet number:

$$Pe = \frac{Gh^2}{D}, \quad (5.13)$$

where $G \sim 0.09\ \mathrm{s}^{-1}$ is the characteristic shear rate near the bead surface, which is evaluated as the slope (at the back wall) of the experimental velocity profile in Fig. 4.5; $h = 1000\ \mu m$ is the width of the microfluidic channel (Table 2.2).

Evaluation gives $Pe_1 \sim 140$ for citrate ions ($D_1 = 0.65 \times 10^{-9}\ m^2/s$) and $Pe_2 \sim 2700$ for alginate chains ($D_2 \approx 3.3 \times 10^{-11}\ m^2/s$, cf. Sec. 5.2.4). Since the Péclet number is relatively high (we will go back to this assumption), the convective flux dominates over the diffusive one everywhere in the fluid except for a thin boundary layer adjacent to the alginate bead. Within this layer, the fluid velocity is low because of the non-slip hydrodynamic boundary condition, and the diffusive flux is comparable with the convective one. This physics is ideally quantified by a diffusive boundary layer theory [Levič (1962)]. This theory is based on the two following statements: (a) the steady state is rapidly achieved; (b) the concentration of molecules changes across the boundary layer much faster than along it, so $\partial c/\partial y" \partial c/\partial x$ and $\partial^2 c/\partial y^2" \partial^2 c/\partial x^2$. Moreover, we suppose that the velocity component perpendicular to the xy-plane is zero ($v_z = 0$) while the molecular concentration is independent of z, i.e., $\partial c/\partial z = 0$. Under these assumptions, the convective diffusion equation takes the following 2D form:

$$v_x \frac{\partial c}{\partial x} + v_y \frac{\partial c}{\partial y} = D \frac{\partial^2 c}{\partial y^2}, \quad (5.14)$$

where the two terms on the left-hand side of this equation often appear to be comparable, so the 1st term cannot be neglected.

The boundary conditions for the citrate ions delivery and alginate chains evacuation read:

$$\begin{cases} c_1(x=0,y)=C_1 \\ c_1(x,y=0)=0 \\ c_1(x,y\to\infty)=C_1 \end{cases} \text{ for citrate,} \tag{5.15}$$

$$\begin{cases} c_2(x=0,y)=0 \\ c_2(x,y=0)=C_2 \\ c_2(x,y\to\infty)=0 \end{cases} \text{ for alginate.} \tag{5.16}$$

This boundary value problem is quite similar to that of the convective diffusion towards an infinite plane in the presence of flow past this plane. Thus, we will follow the main steps of the mathematical resolution of the "infinite plane problem", generalising it to an arbitrary velocity profile near the bead surface. Following Levič (1962), equation (5.14) can be rewritten in (x,ψ)-coordinate system, where ψ is the fluid stream function:

$$\left(\frac{\partial c}{\partial x}\right)_{\psi} = D\frac{\partial}{\partial \psi}\left(v_x\frac{\partial c}{\partial \psi}\right), \tag{5.17}$$

where the subscript ψ at $\frac{\partial c}{\partial x}$ denotes that c is derived in regards to x at constant ψ.

Recall that the velocity profile presented in Fig. 4.5 is at the locations far enough from the alginate bead surface, while the velocity v_x and the stream function ψ in Eq. (5.17) corresponds to the flow in the close vicinity of the bead surface. At the present stage, we were unable to get the velocity distribution close to the bead surface. However, for most of the known cases of laminar flow past a plane (within the laminar hydrodynamic boundary layer) or laminar flow past different shaped solid objects, the velocity profile near the solid surface takes the following general form:

$$v_x = \dot{\gamma}(x)y; \quad v_y = -\frac{1}{2}\frac{d\dot{\gamma}(x)}{dx}y^2; \quad \psi = \frac{1}{2}\dot{\gamma}(x)y^2, \tag{5.18}$$

with $\dot{\gamma}(x)$ being a wall shear rate.

Replacing (5.18) in (5.17) and introducing a new variable

$$X = \sqrt{2}D\int_0^x \sqrt{\dot{\gamma}(x)}dx, \tag{5.19}$$

we get:

$$\left(\frac{\partial c}{\partial X}\right)_{\psi} = \frac{\partial}{\partial \psi}\left(\sqrt{\psi}\frac{\partial c}{\partial \psi}\right). \tag{5.20}$$

Using the similarity method, we introduce another variable

$$\xi = \frac{\psi^{1/2}}{X^{1/3}}, \tag{5.21}$$

which reduces the partial differential equation (5.20) to an ordinary differential equation

$$\frac{d^2c}{d\xi^2} = -\frac{4}{3}\xi^2\frac{dc}{d\xi}, \tag{5.22}$$

associated to the boundary conditions

$$\begin{cases} c_1(\xi = 0) = 0 \\ c_1(\xi \to \infty) = C_1 \end{cases} \text{for citrate}, \tag{5.23}$$

$$\begin{cases} c_2(\xi = 0) = C_2 \\ c_2(\xi \to \infty) = 0 \end{cases} \text{for alginate.} \tag{5.24}$$

The solution to the boundary value problem (5.22), (5.23) or (5.22), (5.24) is straightforward:

$$\begin{cases} c_1(\xi) = \frac{(2/3)^{2/3}}{\Gamma(4/3)} C_1 \int_0^{\xi} \exp\left(-\frac{4}{9}\theta^3\right) d\theta \ \text{ for citrate,} \\ c_2(\xi) = \frac{(2/3)^{2/3}}{\Gamma(4/3)} C_2 \int_{\xi}^{+\infty} \exp\left(-\frac{4}{9}\theta^3\right) d\theta \ \text{ for alginate,} \end{cases} \tag{5.25}$$

where $\Gamma(z)$ is the Gamma function of an argument z; the parameter ξ is related to the Cartesian x, y coordinates through Eqs. (5.18), (5.19), (5.21).

The flux density of the citrate ions or alginate chains at the alginate bead surface is

$$j_i(\tilde{x}) = -D_i\left(\frac{\partial c_i}{\partial y}\right)_{y=0} = (-1)^i \frac{3^{-\frac{2}{3}}}{\Gamma\left(\frac{4}{3}\right)} \frac{D_i C_i}{h} Pe_i^{\frac{1}{3}} \left(\int_0^{\tilde{x}} \sqrt{\tilde{\gamma}(s)} ds\right)^{-\frac{1}{3}}, i = 1,2, \tag{5.26}$$

where we have introduced the dimensionless coordinate $\tilde{x} = x/h$, also the dimensionless shear rate $\tilde{\gamma}(\tilde{x}) = \dot{\gamma}(x)/G$ with respect to some characteristic dimensional shear rate G; the Péclet number, Pe, is given in terms of G by Eq. (5.13).

The total flux (in mol/s) over the alginate bead surface is finally obtained by integrating the flux density:

$$J_i = A\left|\int_0^1 j_i(\tilde{x})\, d\tilde{x}\right| = KbD_iC_iPe_i^{\frac{1}{3}}, \ \ K = \frac{3^{-\frac{2}{3}}}{\Gamma(\frac{4}{3})}\int_0^1 \left(\int_0^{\tilde{x}} \sqrt{\tilde{\gamma}(\tilde{x})} d\tilde{x}\right)^{-\frac{1}{3}} d\tilde{x} \ , \ \ i = 1,2. \tag{5.27}$$

This last equation is the exact result valid for a high Péclet number limit at a precise shear rate profile $\dot{\gamma}(x)$ along the bead surface. Once it is retrieved from experiments or simulations, we can calculate the exact value of the K constant and consequently of the flux. However, for rough

estimations, we put after this $K \sim 1$, since, for example, for the shear rate independent of x (or $\tilde{\gamma}(\tilde{x}) = 1$), we get $K \approx 0.81$.

Evaluations show that the purely diffusive flux [Eq. (5.7)] becomes less than the convective flux [Eq. (5.27)] at elapsed times of about 1 min for citrate ions. Since the convective flux is a relatively weak function of the Péclet number (proportional to $Pe_i^{1/3}$) it could still be of the same order of magnitude as the diffusive flux within the considered range $Pe_i = 140 - 2700$. We should therefore take into account the finite values of the Péclet number, and it is convenient to use an interpolation formula

$$J_{max,i} \approx bD_i C_i Pe_i^{\frac{1}{3}} + C_i \sqrt{\frac{D_i}{\pi t}} A, \tag{5.28}$$

as often proposed in convective diffusion problems [Levič (1962); Russel et al. (1989)].

Again, Eq. (5.28) provides the maximum fluxes of citrate ions or alginate chains (so, the subscript "max" appear), while the minimal value gives the accurate fluxes. From now, we will interest ourselves in the flux of the alginate chains intervening in the bead dissolution kinetics:

$$J_2 = \min\left(\frac{2}{N} J_{max,1}; J_{max,2}\right). \tag{5.29}$$

We evaluate that the citrate concentration in the bulk solution in the microfluidic channel will decrease at the timescale of 5000 s. So, as in Sec. 5.2.2, we can neglect the variation of the citrate concentration with time on the timescale of our experiments.

Finally, combining (5.10) with (5.28) and (5.29), we get the following relationships for the decrease of the alginate bead volume and relative surface with time:

$$V(t) = \begin{cases} V_0 - \frac{4C_1}{NC_2} bD_1^{\frac{2}{3}} (Gh^2)^{\frac{1}{3}} t - \frac{8C_1}{NC_2} \sqrt{\frac{D_1 t}{\pi}} A \text{ if } J_2 = \frac{2}{N} J_{max,1}, \\ V_0 - 2bD_2^{\frac{2}{3}} (Gh^2)^{\frac{1}{3}} t - 4\sqrt{\frac{D_2 t}{\pi}} A \text{ if } J_2 = J_{max,2}, \end{cases} \tag{5.30}$$

$$S_n(t) = \frac{V(t)}{V_0} = \begin{cases} 1 - \frac{4C_1}{NC_2 l_b} D_1^{\frac{2}{3}} \left(\frac{G}{h}\right)^{\frac{1}{3}} t - \frac{8C_1}{NC_2 l_b} \sqrt{\frac{D_1 t}{\pi}} \text{ if } J_2 = \frac{2}{N} J_{max,1}, \\ 1 - \frac{2}{l_b} D_2^{\frac{2}{3}} \left(\frac{G}{h}\right)^{\frac{1}{3}} t - \frac{4}{l_b} \sqrt{\frac{D_2 t}{\pi}} \text{ if } J_2 = J_{max,2}. \end{cases} \tag{5.31}$$

5.2.4 Evaluation of experimental parameters and comparison with experiments

To evaluate the evolution of the bead relative surface with time using Eqs. (5.12), (5.31), we need to define different experimental parameters intervening in these equations. First, the trisodium citrate concentration (far from the bead) and diffusivity are respectively $C_1 = 0.158\ \mathrm{mol/L}$ and $D_1 = 0.65 \times 10^{-9}\ \mathrm{m^2/s}$. Second, the concentration of the alginate chains within the alginate bead is defined through the measured weight fraction of alginate in the bead, $\varphi_{w,AL} = 0.03$ (3%wt):

$$C_2 = \frac{\varphi_{w,AL}\rho_{bead}}{M_{w,AL}}, \tag{5.32}$$

where $\rho_{bead} \approx 10^3\ \mathrm{kg/m^3}$ is the density of the alginate bead and $M_{w,AL} = 140 \pm 20\ \mathrm{kg/mol}$ is the molecular weight of the alginate chains. We get $C_2 \approx 2.14 \times 10^{-4}\ \mathrm{mol/L}$. The values of the diffusion coefficient of alginate chains found in literature differ by several orders of magnitude between different bibliographic sources. So, we decided to evaluate it through the gyration radius R_g, which in its turn, can be evaluated supposing a "blob" conformation [Larson (1999)]:

$$R_g \approx \frac{l_{AL} n^{1/2}}{6^{1/2}}, \tag{5.33}$$

$$D_2 = \frac{k_B T}{6\pi\eta R_g}, \tag{5.34}$$

where $l_{AL} \approx 0.6\ \mathrm{nm}$ and $n \approx 725$ are, respectively, the average length of the alginate monomer and the number of monomers per chain for the given molecular weight of alginate. We get $R_g \approx 6.6\ \mathrm{nm}$ and $D_2 \approx 3.3 \times 10^{-11}\ \mathrm{m^2/s}$.

The number N of Ca bridges per alginate chain can be evaluated if we know the cross-linking density expressed through the number of Ca bridges per unit volume of the alginate bead measured by the ICP-OES spectrometry. For this purpose, a few selected alginate beads were carefully washed with Milli-Q water to remove the excess Ca ions from the supernatant. The alginate beads were completely dissolved with concentrated citric acid, and the obtained liquid phase (after appropriate dilution) was subject to the ICP measurements. The measurements gave, $c_{w,Ca} \approx 0.058\ \frac{\mathrm{g\ Ca}}{\mathrm{g\ bead}}$. After that, the desired quantity N is evaluated as

$$N = 2 c_{w,Ca} \frac{M_{w,AL}}{M_{w,Ca}}, \tag{5.35}$$

where $M_{w,Ca} = 40\ g/mol$ is the calcium molecular weight, and the factor 2 on the right-hand side of the last equation accounts for the fact that one Ca ion is counted twice for the bridge between the first and the second alginate chain and the bridge between the second and the first alginate chain. Evaluation gives $N \approx 400$.

The geometric parameters entering into the model are the channel width $h = 1\ mm$ and the bead effective length $l_b \approx 1.5\ mm$. Finally, the effective shear rate was estimated in Sec. 5.2.3 and is equal to where $G \approx 0.09\ s^{-1}$.

Based on the above evaluated physical parameters, we plotted in Fig. 5.7 theoretical dependencies of the relative bead surface as a function of time, obtained using Eq. (5.12) in the absence of recirculation and Eq. (5.31) in the presence of recirculation.

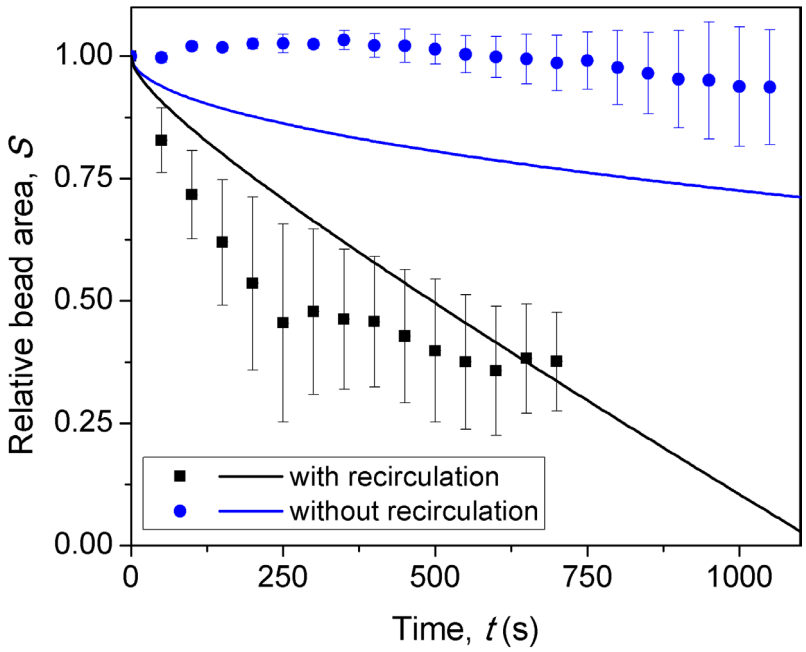

Figure 5.7: Theoretical and experimental temporal dependencies of the relative surface of the alginate bead.

The model does not introduce any adjustable parameter and agrees with experiments only qualitatively or semi-quantitatively in the best case. First, the model does not predict a moderate bead dilatation at short times in the absence of recirculation because it ignores possible bulk bead dissolution. Second, the model overestimates the dissolution speed of the bead in the absence of recirculation, likely because of the same assumption of negligible bulk dissolution, in which case the bead could be dissociated through the disintegration of macroscopic bead parts (containing multiple alginate chains); this macroscopic part is very "heavy" and cannot be rapidly evacuated from the bead by diffusion. On the other hand, a better agreement between theory and experiments is observed for the bead dissolution in the presence of recirculation

flows generated by rotating magnetic fields, which probably highlights the relevance of the model assumptions introduced in Sec. 5.2.1. Recall that starting from $t{\sim}700\ s$, the alginate bead detached from the channel walls and started to spin and to dissolve much more rapidly because of enhanced convective transport under rotation. This effect is not taken into account by the present model. Despite these drawbacks, our model predicts a correct timescale for the bead dissolution in the presence of recirculation ($\tau_d{\sim}500\ s$ vs $\sim 300\ s$ in experiments), which can be arbitrarily defined as the time required to decrease the bead size by a factor of two. So, we believe the model is pertinent for deserving general trends regarding the effect of different physical parameters (magnetic field intensity and frequency, nanoparticle concentration, dissolving agent concentration, etc.) on the dissolution timescale. We will try in Section 5.3 to prospect these trends to the blood clot lysis in the natural in-vivo environment.

5.3 Extrapolation to the fibrinous clot

In this Section, we will try to predict how efficient (or not) the blood clot dissolution would be by the proposed technique based on an enhanced molecular transport through the blocked blood vessels. We will first make a physical extrapolation of the results on the alginate bead dissolution to the blood clot lysis (Sec. 5.3.1). After that, we will briefly present the biochemical aspects of the clot lysis (Sec. 5.3.2), highlighting the complexity of the chemical reactions requiring a further deep investigation.

5.3.1 Physical extrapolation

Let us first assume that the blood clot lysis follows the same physics as the alginate bead dissolution, i.e., the thrombolytic drug is convected towards the clot by field-induced recirculation flow; once at the clot surface, it reacts very quickly with the clot detaching the fibrine degradation products (FDP) from it; the FDP are then evacuated from the clot surface by the convective flux of the recirculating flow. This simple mechanism will be questioned in Sec. 5.3.2. But if this mechanism holds, the characteristic timescale of the clot lysis can be predicted from Eq. (5.31) by putting $S_n = 1$. For rough estimation, we may neglect the zero-Péclet number contribution and suppose that the thrombolytic drug is in (a slight) excess, the condition $J_2 = J_{max,2}$ holds, as was the case for alginate beads. We get the following scaling behaviour:

$$\tau_d{\sim}l_b h^{\frac{1}{3}} {D_2}^{-\frac{2}{3}} G^{-\frac{1}{3}}, \tag{5.36}$$

in which we still must define how the characteristic shear rate G depends on the imposed physical parameters. Recall that in Sec. 4.4, we have established the following scaling law for the recirculation flow speed:

$$v \sim \frac{\varphi_0 \mu_0 H^2 h}{\eta_0}. \tag{5.37}$$

Thus, the characteristic shear rate scales as $G \sim v/h$, and the timescale scaling (5.36) takes the final form as follows:

$$\tau_d \sim l_b d_v^{\frac{1}{3}} D_2^{-\frac{2}{3}} (\varphi_0 \mu_0 H^2)^{-\frac{1}{3}} \eta_0^{\frac{1}{3}}, \tag{5.38}$$

where we have replaced the channel width h with the blood vessel diameter d_v.

At the same, for characteristic sizes $l_b \sim 1\ mm$ and $d_v \sim 1\ mm$, same nanoparticle concentration $\varphi_0 \sim 0.16\ \%vol$, and magnetic field intensity $H \sim 6\ kA/m$, the clot lysis time will be increased in the order of magnitude equivalent to the alginate bead dissolution time by the factor of

$$\left(\frac{D_{AL}}{D_{FDP}}\right)^{\frac{2}{3}} \left(\frac{\eta_b}{\eta_w}\right)^{\frac{1}{3}} \approx 5.4,$$

with $D_{AL} \approx 3.3 \times 10^{-11}$ m^2/s, $D_{FDP} \approx 5 \times 10^{-11}$ m^2/s being diffusion coefficients of the alginate chains in water and the FDP in blood [Diamond and Anand (1993)], respectively; $\eta_b \approx 7 \times 10^{-2}\ Pa \times s$ and $\eta_w \approx 10^{-3}\ Pa \times s$ is the blood and water viscosity, respectively. This evaluation leads to $\tau_d \sim 27$ min for blood clot lysis (instead of 5 min for alginate bead dissolution), which is still a reasonable time for the ischemic stroke treatment. To decrease further this time, one can play on nanoparticle concentration (within the biocompatibility limits) and the magnetic field intensity (within the electromagnetic design limits). Thus, by increasing the nanoparticle concentration up to 1%vol and the magnetic field intensity up to 50 kA/m, one can reduce the lysis time by a factor of 7.5 down to a value of $\tau_d \sim 3.6$ min. This is quite a promising evaluation showing the physical feasibility of the novel technique of ischemic stroke treatment.

Notice further that, as it was discussed in Sec. 4.3.2, the frequency ω of the rotating magnetic field is expected to not influence the dynamics of the clot lysis, at least in the considered low Mason number (or equivalently low frequency) limit (cf. Eq. (3.1), Sec. 4.2) for which the length of the magnetic aggregates decreases with the frequency. This would allow, after specific optimisation, using the standard AC voltage frequency of 50 Hz without the necessity for frequency generators that could considerably reduce the cost of the medical

equipment associated with the proposed medical treatment technique. On the other hand, the lysis time seems to decrease with decreasing size d_v of the blood vessels. However, this decrease is relatively smooth, such that reducing the blood vessel size from $d_v \sim 1\ mm$ to $\sim 50\ \mu m$ (20-fold decrease), the lysis time will be increased by a factor of 2.7. For example, at $\varphi_0 \sim 1\ \%vol$ and $H \sim 50\ kA/m$, we will get $\tau_d \sim 10$ min.

It is worth noticing that the current estimation [Eq. (5.38)] does not show any effect of the thrombolytic drug concentration. This is because of the assumption (5) of the model (Sec. 5.2.1) postulating a hindered convection of the dissolution reagent towards the clot if the evacuation of the dissolution products is not fast enough. It was supposed to occur above some critical concentration of the thrombolytic drug, while below this concentration, the lysis time is expected to be proportional to the ratio of the FDP concentration to the thrombolytic drug concentration [cf. 1st line of Eqs. (5.30), (5.31)]. At this point, we cannot confirm whether such hindered diffusion scenario applies to clot dissolution.

Furthermore, the physical sequence of the clot lysis process could be different from that of the alginate bead dissolution. First, the drug has to be pumped from non-occluded vessels (where it circulates thanks to the normal blood flow) to the occluded vessel. Then, the recirculation flow will constantly renew the reacted drug and constantly evacuate FDP. In the case of an alginate bead, the dissolving agent was already present in the channel. This difference could result in a longer effective clot lysis time compared to the one evaluated through the scaling law (5.38). So, experiments in conditions closer to the target application have to be conducted in future.

At this point, we can evaluate the characteristic time τ_p of the drug "pumping" within the occluded vessel and compare it to the time τ_D of purely diffusive transport in the absence of recirculation. The timescale τ_p can be simply obtained as $\tau_p \sim L_c/v$, where $L_c \sim 200 - 500\ \mu m$ is a typical distance between the inlet of the occluded vessel and the clot (inferred from MRI images in [Nishimura et al. (2010); Nguyen et al. (2011)]), and the recirculation velocity v is given by the scaling (5.37). Taking the "worst" values $L_c = 500\ \mu m$ and $v = 5\ \mu m/s$ [cf. Chapter 4], we obtain the maximum time of the convective delivery of molecules towards the clot on the order of $\tau_p \sim 100\ s$ for $\varphi_0 \sim 0.16\ \%vol$, $H \sim 6\ kA/m$ and the aqueous medium at $\eta_w \approx 10^{-3}\ Pa \times s$. Keeping the same magnetic field and particle concentration but replacing the aqueous medium with blood, the delivery time will be increased by a factor of $\eta_b/\eta_w \sim 70$,

so up to $\tau_p \sim 2\ h$. However, by increasing the magnetic field intensity and the particle volume fraction, the delivery time will be changed by a factor of

$$\frac{(\varphi_0 H^2)_w \times \eta_b}{(\varphi_0 H^2)_b \times \eta_w} \approx 0.16,$$

concerning the time in our microfluidic experiments of Chapter 4. Here subscripts "w" and "b" refer to our experiments in water and future manipulation with a blood medium at higher magnetic fields and particle concentrations. We evaluate that the delivery time could be reduced to about $\tau_p \sim 16$ s at $\varphi_0 \sim 1\ \%vol$ and $H \sim 50\ kA/m$. This is possibly a very optimistic optimisation, not considering the flow perturbations at the inlet of the occluded vessel. Anyway, the delivery time τ_p should be summed with the dissolution time τ_d to evaluate the effective duration of the clot lysis from the moment the thrombolytic drug achieves the inlet of the occluded vessel. Let us now evaluate the delivery time of the thrombolytic drug by pure diffusion from the inlet of the occluded vessel towards the clot. The diffusion coefficient of the tissue plasminogen activator (tPA) in blood can be evaluated by Eq. (5.34), in which the water viscosity is $\eta_w \approx 10^{-3}\ Pa \times s$ should be used (as long as the medium surrounding the blood proteins is mostly water), and the tPA gyration radius is $R_g \approx 3.3\ nm$ [Rathore et al. (2012)]. This gives $D_{t-PA} \sim 6.7 \times 10^{-11}\ m^2/s$ and the delivery time $\tau_D \sim {L_c}^2/D_{t-PA} \sim 1\ h$. This time appears to be higher than the convective deliver time τ_p. So, with the slower diffusion-limited dissolution of the blood clot (Sec. 5.2.4, Fig. 5.7), slower diffusive drug transport is expected to be predictably less efficient for clot lysis than field-enhanced clot dissolution and field-enhanced drug delivery.

We should also highlight that the physical limits, extensively discussed in the present chapter, are not the only ones that could influence (in a positive or negative sense) the clot lysis dynamics. Biochemical aspects briefly reviewed in the next Section 5.4.2 could be as important as purely physical aspects.

5.3.2 Biochemical aspects

In vivo, fibrin polymerisation results from the aggregation of fibrinogen fragments, a 340 kDa monomer, after thrombin cut. The fibrin structure is presented in Fig. 5.8.

When a clot has formed and fulfilled its haemostatic function, it is typically dissolved by the fibrinolytic system to restore impaired blood circulation. The main enzyme involved in this cascade is plasmin, a serine protease with an affinity for trypsin and cleaving lysine and arginine residues in the polypeptide chain. Plasmin is present in the blood in the zymogen form, and

plasminogen is produced in the liver, having a molecular mass of 92 kDa and an average plasma concentration of 1.5 to 2 μM. This precursor is activated by the action of factors such as tissue plasminogen activator (tPA), urokinase-type plasminogen activator (uPA) or streptokinases and staphylokinases. The tPA and staphylokinase are fibrin-selective, remaining bound to it and are therefore protected from rapid inhibition, while streptokinase and uPA are non-fibrin-selective enzymes, activating indiscriminate free blood plasminogen like that bound to fibrin. Lysis of fibrin by plasmin results in the formation of degradation products (FDP) - soluble fragments, which are similar to the proteolytic fragments of fibrinogen, the difference being in the presence or absence of fibrinopeptides.

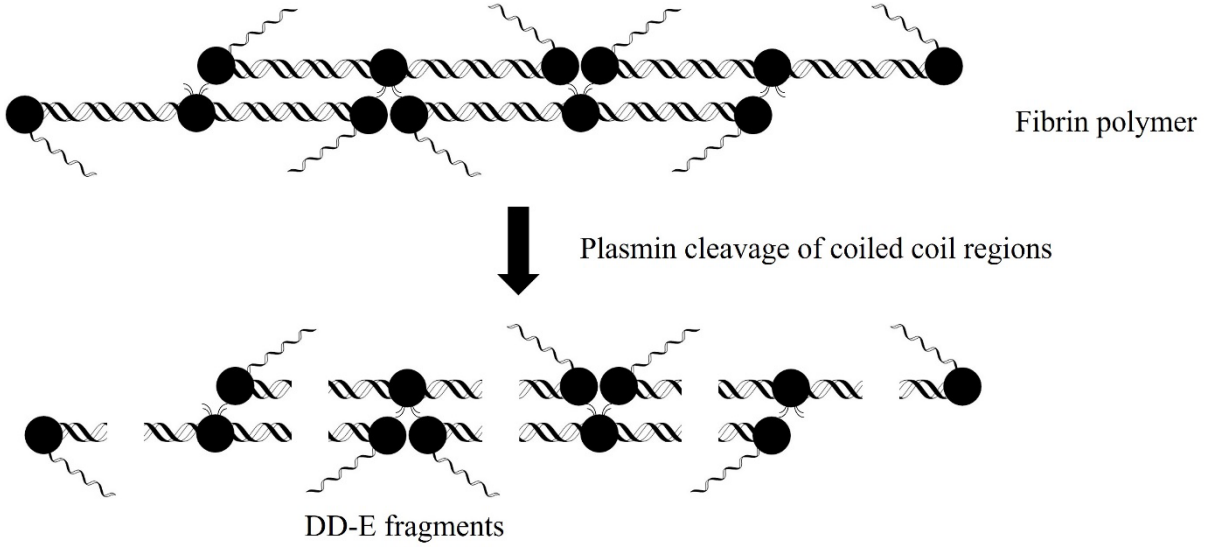

Figure 5.8: A structural model for the fibrin fibre disaggregation. This simplified model depicts the extension of the fiber arising from stretching of the coiled coil region. Protofibrins are linked together by unstructured αC regions.

We give the name internal lysis or intrinsic lysis to the process which imitates the phenomenon physiology of fibrinolysis. Two main proteins control thrombolysis: the inhibitor of plasminogen activator type 1 (PAI-1), which inhibits tPA and α2-antiplasmin, which inhibits plasmin. When used to treat patients with thrombolytic disorder, tPA is administered in sufficient concentrations to counteract the inhibitory action of PAI-1 (saturation of the protein-ligand type) which can lead to bleeding episodes. On another side, plasmin injection is rapidly inhibited by plasma α2-antiplasmin, causing the make it safer but ineffective, because it is neutralised too quickly by α2-antiplasmin. To simulate this process in vitro, either tPA mixed with platelet-rich plasma, i.e., tPA and plasminogen are mixed with fibrinogen to coagulate so that the clot thus formed can be dissolved through the activation of the plasmin present on the surface of the fibrin matrix.

This short overview of the fibrinolysis process clearly shows that there is an important number of chemical reactions and biochemical reagents, which could result in reaction times comparable to the timescales of the convective diffusion of the reagents, such that the diffusion-limited approximation used in our model could appear to be no longer valid. Thus, the lysis process should be handled with care, considering the realistic reaction rates for the complete scheme of the lysis.

5.4 Conclusion

This chapter focuses on the dissolution of an alginate hydrogel bead embedded in a closed microfluidic channel serving as a proxy of a fibrin clot thanks to induced recirculation flows via the application of an external rotating magnetic field. We observed a 50% volume decrease of the artificial clot in 300 sec by the chelating agent in the presence of field-induced recirculation flow when the purely diffusive transport of such an agent was ineffective. We also developed a theoretical model using a diffusion-limited approximation for the dissolution rate of the alginate bead, along with a diffusive boundary layer approach for the convective diffusion of the reagents toward and out of the bead. This model allows a satisfactory semi-quantitative prediction of the characteristic dissolution time without adjustable parameters. Coupling this model with experimental results on alginate beads, we could predict the timescale of the clot lysis process in a realistic in vivo environment. At physically realistic parameters, the lysis time could be in the range of 4-30 min, depending on the blood vessel size, magnetic field intensity and nanoparticle concentration. However, we warrant the reader about the possible increase of this time because of the draining of the thrombolytic drug from non-occluded to occluded vessels (with strong flow perturbations at the inlet) and the relatively long reaction time of the entire sequence of the lysis process.

While the formation of a fibrin clot is far more complex than that of an alginate hydrogel, their mechanism remains quite similar as they are initially soluble polymeric chains that, once reticulated, become insoluble and "semi-rigid". The cleavage of their cross-linking compound can also disaggregate both structures by a simple chelating agent (sodium citrate and plasmin). This is because using an alginate gel as a proxy to test our hypothesis was relevant. By extension, the dissolution of a fibrin clot in vitro by the induction of a recirculation flow should keep some similarity to the dissolution of the alginate bead.

Conclusions and perspectives

In the classical treatment of brain strokes through intravenous injection of a thrombolytic drug, the time scale for the action of a thrombolytic agent such as tissue plasminogen activator (tPA) takes over an hour to diffuse from the intravenous entry point to the brain capillaries where the clot is localised, and it leaves a small window of treatment of 3 to 4 h to prevent neuro-damaging sequels to the patient. Pulse Therapeutics, a USA start-up company, has recently proposed an alternative treatment allowing a considerable shortening of the drug delivery and clot lysis. The technique is based on the injection of a magnetic colloid together with a thrombolytic agent, which generates recirculation fluxes in occluded vessels under applied AC rotating magnetic fields. In this PhD thesis, we aimed to realise an in-vitro microfluidic model of an artificial clot's lysis and understand the effect of the applied magnetic field on the drug transport and clot lysis processes. As a first attempt at this problematic, we primarily focused on the purely physical phenomena and eliminated biochemical aspects by using aqueous media (instead of blood or blood plasma) as a dispersing liquid for our citrate-coated iron oxide nanoparticles (IONPs) and using a calcium alginate polymer microbead as a proxy of a fibrinous blood clot. Furthermore, to mimic the slight colloidal destabilisation of IONPs commonly observed in physiological media, we dispersed our citrate coated IONPs in a 0.35M aqueous sodium chloride solution at pH≈5.5 that led to slight primary agglomeration through screening of interparticle electrostatic repulsion with a small fraction of ~100 nm agglomerates appeared. This primary agglomeration is necessary for strong magnetic interactions, allowing effective remote control over IONPs at applied magnetic fields as weak as ~0.01 T.

For rapid dissolution of artificial clots, we need to realise and perfectly master at least the three following steps of the process: (a) individual nanoparticles (or rather their primary agglomerates) must be able to rapidly self-assemble into micron-sized elongated aggregates upon application of a rotating magnetic field; (b) the so formed aggregates, through their spinning under applied rotating field, must be able to generate recirculating flows in initially quiescent liquid, as opposed to individual IONPs or their primary agglomerates, which are subject to strong Brownian motion; (c) the field-induced recirculation must be strong enough to promote a rapid delivery of a dissolution agent toward an artificial clot and rapid clot dissolution thanks to the continuous

renewal of the delivered dissolution reagent and continuous evacuation of the clot degradation products. The main results concerning these three steps can be summarised as follows:

(a) After applying a circularly polarised rotating magnetic field, self-assembling primary IONP agglomerates into needle-like aggregates, synchronously rotating with the magnetic field, is observed. The aggregates achieve a maximal length of L_{max}~100 μm at a magnetic field $H \approx 9\ kA/m$ and IONP volume fraction $\varphi_0 = 1.6 \times 10^{-3}$. This final length is dictated by the balance between their hydrodynamic interactions and cohesive magnetic interactions allowing for the scaling $L_{max} \propto \nu^{-1/2}$ with the field frequency in the range $5 \leq \nu \leq 25$ Hz. The kinetics of the self-assembly is governed by the aggregate growth (through diffusive convection of neighbouring nanoparticles toward rotating aggregates) and the aggregate coalescence (arising due to their dipole-dipole interactions). Both these mechanisms are incorporated into the population balance equation allowing a correct prediction (without adjustable parameters) of the aggregate size distribution, average aggregate size and aggregation timescale, τ_a~1 min in acceptable agreement with experiments and compatible with the target biomedical application.

(b) It has also been found that in the presence of a weak magnetic field gradient ($|\nabla B| \approx 0.3$ T/m) superimposed to a homogeneous rotating field, the rotation of aggregates generates macroscopic recirculation flows in a closed microfluidic channel simulating a blood capillary, thanks to the asymmetry of their concentration profile across the channel. The generated flow attained experimental peak velocities in the order of v~10 μm/s within the channel of a width of h~500 μm at the magnetic field amplitude and frequency of $H \approx 6$ kA/m and $\nu = 5$ Hz. A momentum balance equation incorporating antisymmetric stresses allowed a decent quantitative agreement with experiments on field-induced velocity profiles measured by particle image velocimetry (PIV).

(c) Such flow has been demonstrated to enhance the dissolution of a calcium alginate polymer bead placed in the microfluidic channel. The dissolution was achieved through convective transport of the trisodium citrate dissolved at 0.158 M in the magnetic colloid filling the channel at $\varphi_0 = 1.6 \times 10^{-3}$. In the presence of the rotating magnetic field ($H \approx 6$ kA/m, $\nu = 5$ Hz) coupled with a weak gradient ($|\nabla B| \approx 0.3$ T/m), a 50% volume decrease of the alginate bead was reached within 5 minutes when the diffusive transport in the absence of the field could not dissolve it. Our model, based on the diffusive boundary layer approach, highlights the importance of the convective

diffusion of the dissolution agent (trisodium citrate) towards the alginate bead and the bead degradation product (desorbed alginate chains) out of the bead. The model predicts the bead dissolution kinetics in a semiquantitative agreement with experiments. Extrapolation of our theory and experimental data to the fibrinous blood clots suggests that depending on factors such as the blood vessel size, magnetic field intensity, the IONP concentration and diffusivities of biomolecules, the dissolution of the clot could be achieved in the time interval of 4-30 min. While the alginate model is a simple one compared to the intricate cascade of factors intervening in the regulation of the dissolution of a fibrinous clot, their similar insoluble reticulated polymeric chains can be both disaggregated by the cleavage of their crosslinking compound by a chelating agent. This similar mode of action tends to comfort us regarding the qualitative effects of the magnetic colloid on the treatment of the fibrinous clot in an ischemic stroke.

The next order of progression will concern biochemical aspects of the blood clot dissolution in a natural physiological environment. First, a biocompatible magnetic colloid should be synthesised, and its surface chemistry should be carefully designed to achieve an optimal state of primary IONP colloidal agglomeration in the blood or blood plasma medium. This means that the primary agglomerates must fit the size range when they remain stable in the absence of a magnetic field but can rapidly and reversibly self-assemble into micron-sized aggregates under applied AC (and/or DC) magnetic fields. This will impose a tedious study of the plasma protein interactions with the functionalised nanoparticle surface concerning the colloidal stability and biocompatibility.

The fluid dynamics and mass transport problems (whose fundamentals were developed in the present manuscript) should also be adapted to actual biomedical conditions. For example, an artificial branched endovascular network can be created through 3D printing, allowing a more accurate simulation of the drug pumping from non-occluded to occluded vessels with a closer look into the flow field near the entrance to the occluded vessel. On the other hand, a complete diffusive, convective and reaction mass exchange scheme between the blood solutes (including a thrombolytic agent), fibrine clot matrix and fibrine degradation products (FDP) should be considered for better understanding and optimisation of the field-enhanced clot lysis process.

Finally, unlike the results reported in Chapter 4, we have recently managed to get a well-ordered collective motion of magnetic aggregates "rolling" over a microfluidic channel wall thanks to their spinning in the presence of a rotating magnetic field. Very briefly, a more substantial (but

still reasonable) IONP primary agglomeration (surprisingly) gives a better monodispersity of the field-induced aggregates. It leads to a more ordered aggregate displacement at speeds of about 0.8 mm/s – a value comparable to typical bloodstream velocities in the human vascular system. If these preliminary results are validated after a detailed statistical study, they open a new locomotion strategy, possibly providing a more efficient thrombolytic drug delivery in our target application. In fact, the IONPs could be replaced by nanometric drug carrying magneto-liposomes. Their field-induced spinning aggregates can deliver the drug through controlled swimming along the blood vessel walls towards the clot. In contrast, the drug release can be initiated through, for example, inductive heating of the magneto-liposomes near the target site by application of GHz AC electromagnetic fields, as typically used in magnetic hyperthermia treatment. From the general perspective, this new type of field-induced locomotion is interesting *per se* for fluid mechanics (through coupling between external torque and hydrodynamic wall interactions) and is not restricted to the clot lysis application but could be extended, among others, to cancer treatment through localised drug delivery and controlled drug release at the target site.

In a longer perspective, *in vivo* studies of the blood clot lysis under applied magnetic fields should be undertaken by trying to combine the field-enhanced clot dissolution with real-time visualization through MPI.

Bibliography

Adamczyk, Z., Van De Ven, T.G.M., 1981. Deposition of brownian particles onto cylindrical collectors. Journal of Colloid and Interface Science 84, 497–518. https://doi.org/10.1016/0021-9797(81)90240-X

Aldous, D.J., 1999. Deterministic and Stochastic Models for Coalescence (Aggregation and Coagulation): A Review of the Mean-Field Theory for Probabilists. Bernoulli 5, 3. https://doi.org/10.2307/3318611

Bacri, J.-C., Cebers, A.O., Perzynski, R., 1994. Behavior of a magnetic fluid microdrop in a rotating magnetic field. Phys. Rev. Lett. 72, 2705–2708. https://doi.org/10.1103/PhysRevLett.72.2705

Bashtovoi, V G, Krakov, M S, and Reks, A G. 1985. "Instability of a flat layer of magnetic liquid for supercritical magnetic fields". United States.

Berthier, S., 1993. Optique des milieux composites. Polytechnica, Paris.

Blums, E., Cebers, A., Maiorov, M.M., 1996. Magnetic Fluids: DE GRUYTER. https://doi.org/10.1515/9783110807356

Boroun, S., Larachi, F., 2020. Anomalous anisotropic transport of scalars in dilute ferrofluids under uniform rotating magnetic fields – Mixing time measurements and ferrohydrodynamic simulations. Chemical Engineering Journal 380, 122504. https://doi.org/10.1016/j.cej.2019.122504

Brenner, H., 1974. Rheology of a dilute suspension of axisymmetric Brownian particles. International Journal of Multiphase Flow 1, 195–341. https://doi.org/10.1016/0301-9322(74)90018-4

Buyevich, Yu.A., Ivanov, A.O., 1992. Equilibrium properties of ferrocolloids. Physica A: Statistical Mechanics and its Applications 190, 276–294. https://doi.org/10.1016/0378-4371(92)90037-Q

Buyevich, Y.A., Ivanov, A.O., Zubarev, A.Yu., 1990. Statistical thermodynamics of ferrocolloids. Journal of Magnetism and Magnetic Materials 85, 33–36. https://doi.org/10.1016/0304-8853(90)90011-E

Cēbers, A., 2002. Dynamics of an elongated magnetic droplet in a rotating field. Phys. Rev. E 66, 061402. https://doi.org/10.1103/PhysRevE.66.061402

Chang, D., Lim, M., Goos, J.A.C.M., Qiao, R., Ng, Y.Y., Mansfeld, F.M., Jackson, M., Davis, T.P., Kavallaris, M., 2018. Biologically Targeted Magnetic Hyperthermia: Potential and Limitations. Front. Pharmacol. 9, 831. https://doi.org/10.3389/fphar.2018.00831

Chaves, A., Rinaldi, C., Elborai, S., He, X., Zahn, M., 2006. Bulk Flow in Ferrofluids in a Uniform Rotating Magnetic Field. Phys. Rev. Lett. 96, 194501. https://doi.org/10.1103/PhysRevLett.96.194501

Cheng, Z., Juli, C., Wood, N.B., Gibbs, R.G.J., Xu, X.Y., 2014. Predicting flow in aortic dissection: Comparison of computational model with PC-MRI velocity measurements. Medical Engineering & Physics 36, 1176–1184. https://doi.org/10.1016/j.medengphy.2014.07.006

Chhabra, R., Shankar, V., 2018. Coulson and Richardson's Chemical Engineering. Elsevier. https://doi.org/10.1016/C2017-0-02843-4

Chiriac, H., Radu, E., Țibu, M., Stoian, G., Ababei, G., Lăbușcă, L., Herea, D.-D., Lupu, N., 2018. Fe-Cr-Nb-B ferromagnetic particles with shape anisotropy for cancer cell destruction by magneto-mechanical actuation. Sci Rep 8, 11538. https://doi.org/10.1038/s41598-018-30034-3

Chirikov, D., Zubarev, A., Kuzhir, P., Raboisson-Michel, M., Verger-Dubois, G., 2022. To the theory of magnetically induced flow in a ferrofluid cloud: effect of the cloud initial shape. Eur. Phys. J. Spec. Top. 231, 1187–1194. https://doi.org/10.1140/epjs/s11734-022-00523-8

Christensen, R.M., McCoy, J.J., 1980. Mechanics of Composite Materials. Journal of Applied Mechanics 47, 460–461. https://doi.org/10.1115/1.3153710

Cousin, F., Dubois, E., Cabuil, V., 2003. Tuning the interactions of a magnetic colloidal suspension. Phys. Rev. E 68, 021405. https://doi.org/10.1103/PhysRevE.68.021405

Clements, M.J., 2016. A mathematical model for magnetically-assisted delivery of thrombolytics in occluded blood vessels for ischemic stroke treatment. https://doi.org/10.15781/T2JH3DM9Q

Cousin, F., Dubois, E., Cabuil, V., 2001. Approach of the critical point of gas–liquid transitions in an electrostatically stabilized colloidal suspension. The Journal of Chemical Physics 115, 6051–6057. https://doi.org/10.1063/1.1400128

Cowley, M.D., 1989. **Ferrohydrodynamics.** By R. E. R OSENSWEIG . Cambridge University Press, 1985. 344 pp. £45.

Creighton, F. M., 13 November 2012. "Magnetic-based systems for treating occluded vessels," U.S. patent no. 8,308,628 .

Cueille, S., Sire, C., 1997. Smoluchowski's equation for cluster exogenous growth. Europhys. Lett. 40, 239–244. https://doi.org/10.1209/epl/i1997-00454-4

Diamond, S.L., Anand, S., 1993. Inner clot diffusion and permeation during fibrinolysis. Biophysical Journal 65, 2622–2643. https://doi.org/10.1016/S0006-3495(93)81314-6

Douziech-Eyrolles, L., Marchais, H., Hervé, K., Munnier, E., Soucé, M., Linassier, C., Dubois, P., Chourpa, I., 2007. Nanovectors for anticancer agents based on superparamagnetic iron oxide nanoparticles. Int J Nanomedicine 2, 541–550.

Dubois, E., Cabuil, V., Boué, F., Perzynski, R., 1999. Structural analogy between aqueous and oily magnetic fluids. The Journal of Chemical Physics 111, 7147–7160. https://doi.org/10.1063/1.480007

Dubois, E., Perzynski, R., Boué, F., Cabuil, V., 2000. Liquid−Gas Transitions in Charged Colloidal Dispersions: Small-Angle Neutron Scattering Coupled with Phase Diagrams of Magnetic Fluids. Langmuir 16, 5617–5625. https://doi.org/10.1021/la000053u

Estelrich, J., Escribano, E., Queralt, J., Busquets, M., 2015. Iron Oxide Nanoparticles for Magnetically-Guided and Magnetically-Responsive Drug Delivery. IJMS 16, 8070–8101. https://doi.org/10.3390/ijms16048070

Ezzaier, H., Alves Marins, J., Razvin, I., Abbas, M., Ben Haj Amara, A., Zubarev, A., Kuzhir, P., 2017. Two-stage kinetics of field-induced aggregation of medium-sized magnetic nanoparticles. J. Chem. Phys. 146, 114902. https://doi.org/10.1063/1.4977993

Ezzaier, H., Marins, J., Claudet, C., Hemery, G., Sandre, O., Kuzhir, P., 2018. Kinetics of Aggregation and Magnetic Separation of Multicore Iron Oxide Nanoparticles: Effect of the Grafted Layer Thickness. Nanomaterials 8, 623. https://doi.org/10.3390/nano8080623

Gabayno, J.L.F., Liu, D.-W., Chang, M., Lin, Y.-H., 2015. Controlled manipulation of Fe_3O_4 nanoparticles in an oscillating magnetic field for fast ablation of microchannel occlusion. Nanoscale 7, 3947–3953. https://doi.org/10.1039/C4NR06143H

Goel, S., Duda, D.G., Xu, L., Munn, L.L., Boucher, Y., Fukumura, D., Jain, R.K., 2011. Normalization of the Vasculature for Treatment of Cancer and Other Diseases. Physiological Reviews 91, 1071–1121. https://doi.org/10.1152/physrev.00038.2010

Gräfe, C., Slabu, I., Wiekhorst, F., Bergemann, C., von Eggeling, F., Hochhaus, A., Trahms, L., Clement, J.H., 2016. Magnetic particle spectroscopy allows precise quantification of nanoparticles after passage through human brain microvascular endothelial cells. Phys. Med. Biol. 61, 3986–4000. https://doi.org/10.1088/0031-9155/61/11/3986

Happel, J., Brenner, H., 1983. Low Reynolds number hydrodynamics: with special applications to particulate media, 1st pbk. ed. ed, Mechanics of fluids and transport processes. M. Nijhoff ; Distributed by Kluwer Boston, The Hague ; Boston : Hingham, MA, USA.

Hassan, M.K., Hassan, M.Z., 2008. Condensation-driven aggregation in one dimension. Phys. Rev. E 77, 061404. https://doi.org/10.1103/PhysRevE.77.061404

Hejazian, M., Nguyen, N.-T., 2016. Magnetofluidic concentration and separation of non-magnetic particles using two magnet arrays. Biomicrofluidics 10, 044103. https://doi.org/10.1063/1.4955421

Hejazian, M., Phan, D.-T., Nguyen, N.-T., 2016. Mass transport improvement in microscale using diluted ferrofluid and a non-uniform magnetic field. RSC Adv. 6, 62439–62444. https://doi.org/10.1039/C6RA11703A

Hergt, R., Dutz, S., Müller, R., Zeisberger, M., 2006. Magnetic particle hyperthermia: nanoparticle magnetism and materials development for cancer therapy. J. Phys.: Condens. Matter 18, S2919–S2934. https://doi.org/10.1088/0953-8984/18/38/S26

Holm, C., Weis, J., 2005. The structure of ferrofluids: A status report. Current Opinion in Colloid & Interface Science 10, 133–140. https://doi.org/10.1016/j.cocis.2005.07.005

Hong, C.-Y., Jang, I.J., Horng, H.E., Hsu, C.J., Yao, Y.D., Yang, H.C., 1997. Ordered structures in Fe3O4 kerosene-based ferrofluids. Journal of Applied Physics 81, 4275–4277. https://doi.org/10.1063/1.364800

Hynninen, A.-P., Dijkstra, M., 2005. Phase Diagram of Dipolar Hard and Soft Spheres: Manipulation of Colloidal Crystal Structures by an External Field. Phys. Rev. Lett. 94, 138303. https://doi.org/10.1103/PhysRevLett.94.138303

Jordan, A., Scholz, R., Maier-Hauff, K., Johannsen, M., Wust, P., Nadobny, J., Schirra, H., Schmidt, H., Deger, S., Loening, S., Lanksch, W., Felix, R., 2001. Presentation of a new magnetic field therapy system for the treatment of human solid tumors with magnetic fluid hyperthermia. Journal of Magnetism and Magnetic Materials 225, 118–126. https://doi.org/10.1016/S0304-8853(00)01239-7

Kaczmarek, K., Hornowski, T., Kubovčíková, M., Timko, M., Koralewski, M., Józefczak, A., 2018. Heating Induced by Therapeutic Ultrasound in the Presence of Magnetic Nanoparticles. ACS Appl. Mater. Interfaces 10, 11554–11564. https://doi.org/10.1021/acsami.8b02496

Kalikmanov, V. I., 2013. "Nucleation theory," in Lecture Notes in Physics (Springer Dordrecht), Vol. 860.

Kim, H., Sau, M., Furst, E.M., 2020. An Expanded State Diagram for the Directed Self-Assembly of Colloidal Suspensions in Toggled Fields. Langmuir 36, 9926–9934. https://doi.org/10.1021/acs.langmuir.0c01616

Korchinski, D.J., Taha, M., Yang, R., Nathoo, N., Dunn, J.F., 2015. Iron Oxide as an Mri Contrast Agent for Cell Tracking: Supplementary Issue. Magn Reson Insights 8s1, MRI.S23557. https://doi.org/10.4137/MRI.S23557

Kröger, M., Vermant, J., 2000. The Structure and Rheology of Complex Fluids. Applied Rheology 10, 110–111. https://doi.org/10.1515/arh-2000-0024

Kuzhir, P., López-López, M.T., Bossis, G., 2009. Magnetorheology of fiber suspensions. II. Theory. Journal of Rheology 53, 127–151. https://doi.org/10.1122/1.3005405

Landau, L. D. and Lifshitz, E. M., 1980. Statistical Physics, 3rd ed. (Pergamon, Oxford,), Vol. 1.

Landau, L.D., Lifšic, E.M., Pitaevskij, L.P., Landau, L.D., 2009. Electrodynamics of continuous media, 2. ed., rev.enlarged, repr. ed, Course of theoretical physics / L. D. Landau and E. M. Lifshitz. Elsevier Butterworth-Heinemann, Amsterdam Heidelberg.

Larson, R.G., 1999. The structure and rheology of complex fluids. New York: Oxford university press.

Laskar J. M., & Philip J., Raj B., 2010. Experimental investigation of magnetic-field-induced aggregation kinetics in nonaqueous ferrofluids. Physical review. E, Statistical, nonlinear, and soft matter physics. 82. https://doi.org/10.1103/PhysRevE.82.021402.

Lebedev, A.V., Engel, A., Morozov, K.I., Bauke, H., 2003. Ferrofluid drops in rotating magnetic fields. New J. Phys. 5, 57–57. https://doi.org/10.1088/1367-2630/5/1/357

Leulmi, S., Chauchet, X., Morcrette, M., Ortiz, G., Joisten, H., Sabon, P., Livache, T., Hou, Y., Carrière, M., Lequien, S., Dieny, B., 2015. Triggering the apoptosis of targeted human renal cancer cells by the vibration of anisotropic magnetic particles attached to the cell membrane. Nanoscale 7, 15904–15914. https://doi.org/10.1039/C5NR03518J

Levič, V.G. 1962. Physicochemical hydrodynamics, 2. ed. ed, Prentice Hall international series in the physical and chemical engineering sciences. Prentice-Hall, Englewood Cliffs, NJ.

Li, J., Liu, F., Gupta, S., Li, C., 2016. Interventional Nanotheranostics of Pancreatic Ductal Adenocarcinoma. Theranostics 6, 1393–1402. https://doi.org/10.7150/thno.15122

Li, Q., Liu, X., Chang, M., Lu, Z., 2018. Thrombolysis Enhancing by Magnetic Manipulation of Fe3O4 Nanoparticles. Materials 11, 2313. https://doi.org/10.3390/ma11112313

Liu, C., Lomakin, A., Thurston, G.M., Hayden, D., Pande, A., Pande, J., Ogun, O., Asherie, N., Benedek, G.B., 1995. Phase Separation in Multicomponent Aqueous-Protein Solutions. J. Phys. Chem. 99, 454–461. https://doi.org/10.1021/j100001a067

Liu, J., Lawrence, E.M., Wu, A., Ivey, M.L., Flores, G.A., Javier, K., Bibette, J., Richard, J., 1995. Field-Induced Structures in Ferrofluid Emulsions. Phys. Rev. Lett. 74, 2828–2831. https://doi.org/10.1103/PhysRevLett.74.2828

López-López, M.T., Kuzhir, P., Durán, J.D.G., Bossis, G., 2010. Normal stresses in a shear flow of magnetorheological suspensions: Viscoelastic versus Maxwell stresses. Journal of Rheology 54, 1119–1136. https://doi.org/10.1122/1.3479043

Mao, L., Koser, H., 2007. Overcoming the Diffusion Barrier: Ultra-Fast Micro-Scale Mixing Via Ferrofluids, in: TRANSDUCERS 2007 - 2007 International Solid-State Sensors, Actuators and Microsystems Conference. Presented at the TRANSDUCERS 2007 - 2007 International Solid-State Sensors, Actuators and Microsystems Conference, IEEE, Lyon, France, pp. 1829–1832. https://doi.org/10.1109/SENSOR.2007.4300511

Martin, J.E., Snezhko, A., 2013. Driving self-assembly and emergent dynamics in colloidal suspensions by time-dependent magnetic fields. Rep. Prog. Phys. 76, 126601. https://doi.org/10.1088/0034-4885/76/12/126601

Martin, J.E., Solis, K.J., 2015. Fully alternating, triaxial electric or magnetic fields offer new routes to fluid vorticity. Soft Matter 11, 241–254. https://doi.org/10.1039/C4SM01936A

Massart, R., 1981. Preparation of aqueous magnetic liquids in alkaline and acidic media. IEEE Trans. Magn. 17, 1247–1248. https://doi.org/10.1109/TMAG.1981.1061188

Mohapatra, D.K., Philip, J., 2019. Effect of surface charge screening on critical magnetic fields during field induced structural transitions in magnetic fluids. Journal of Applied Physics 125, 244301. https://doi.org/10.1063/1.5109204

Momtazi, L. 2014. Synthesis and Characterization of Magnetic Nanocarriers for Cancer Drug Delivery. Doctoral dissertation, UNIVERSITY OF OSLO

Montiel Schneider, M.G., Martín, M.J., Otarola, J., Vakarelska, E., Simeonov, V., Lassalle, V., Nedyalkova, M., 2022. Biomedical Applications of Iron Oxide Nanoparticles: Current Insights Progress and Perspectives. Pharmaceutics 14, 204. https://doi.org/10.3390/pharmaceutics14010204

Musickhin, A., Yu Zubarev, A., Raboisson-Michel, M., Verger-Dubois, G., Kuzhir, P., 2020. Field-induced circulation flow in magnetic fluids. Phil. Trans. R. Soc. A. 378, 20190250. https://doi.org/10.1098/rsta.2019.0250

Neumann, A., Gräfe, K., von Gladiss, A., Ahlborg, M., Behrends, A., Chen, X., Schumacher, J., Blancke Soares, Y., Friedrich, T., Wei, H., Malhorta, A., Aderhold, E., Bakenecker, A.C., Lüdtke-Buzug, K., Buzug, T.M., 2022. Recent developments in magnetic particle imaging. Journal of Magnetism and Magnetic Materials 550, 169037. https://doi.org/10.1016/j.jmmm.2022.169037

Nguyen, J., Nishimura, N., Fetcho, R.N., Iadecola, C., Schaffer, C.B., 2011a. Occlusion of Cortical Ascending Venules Causes Blood Flow Decreases, Reversals in Flow Direction, and Vessel Dilation in Upstream Capillaries. J Cereb Blood Flow Metab 31, 2243–2254. https://doi.org/10.1038/jcbfm.2011.95

Nguyen, J., Nishimura, N., Fetcho, R.N., Iadecola, C., Schaffer, C.B., 2011b. Occlusion of Cortical Ascending Venules Causes Blood Flow Decreases, Reversals in Flow Direction, and Vessel Dilation in Upstream Capillaries. J Cereb Blood Flow Metab 31, 2243–2254. https://doi.org/10.1038/jcbfm.2011.95

Nishimura, N., Rosidi, N.L., Iadecola, C., Schaffer, C.B., 2010a. Limitations of Collateral Flow after Occlusion of a Single Cortical Penetrating Arteriole. J Cereb Blood Flow Metab 30, 1914–1927. https://doi.org/10.1038/jcbfm.2010.157

Pernal, S.P., Willis, A.J., Sabo, M.E., Moore, L.M., Olson, S.T., Morris, S.C., Creighton, F.M., Engelhard, H.H., 2020. An in vitro Model System for Evaluating Remote Magnetic Nanoparticle Movement and Fibrinolysis. IJN Volume 15, 1549–1568. https://doi.org/10.2147/IJN.S237395

Pokrovskiy V.N., 1978. Statistical mechanics of diluted suspensions, Nauka, Moscow.

Prokopieva, T.A., Danilov, V.A., Kantorovich, S.S., Holm, C., 2009. Ground state structures in ferrofluid monolayers. Phys. Rev. E 80, 031404. https://doi.org/10.1103/PhysRevE.80.031404

Promislow, J.H.E., Gast, A.P., 1997. Low-energy suspension structure of a magnetorheological fluid. Phys. Rev. E 56, 642–651. https://doi.org/10.1103/PhysRevE.56.642

Qian, J., Law, C.K., 1997. Regimes of coalescence and separation in droplet collision. J. Fluid Mech. 331, 59–80. https://doi.org/10.1017/S0022112096003722

Queiros Campos, J., Boulares, M., Raboisson-Michel, M., Verger-Dubois, G., García Fernández, J.M., Godeau, G., Kuzhir, P., 2021a. Improved Magneto-Microfluidic Separation of Nanoparticles

through Formation of the β-Cyclodextrin–Curcumin Inclusion Complex. Langmuir 37, 14345–14359. https://doi.org/10.1021/acs.langmuir.1c02245

Queiros Campos, J., Checa-Fernandez, B.L., Marins, J.A., Lomenech, C., Hurel, Ch., Godeau, G., Raboisson-Michel, M., Verger-Dubois, G., Bee, A., Talbot, D., Kuzhir, P., 2021b. Adsorption of Organic Dyes on Magnetic Iron Oxide Nanoparticles. Part II: Field-Induced Nanoparticle Agglomeration and Magnetic Separation. Langmuir 37, 10612–10623. https://doi.org/10.1021/acs.langmuir.1c02021

Queiros Campos, J., Checa-Fernandez, B.L., Marins, J.A., Lomenech, C., Hurel, Ch., Godeau, G., Raboisson-Michel, M., Verger-Dubois, G., Bee, A., Talbot, D., Kuzhir, P., 2021c. Adsorption of Organic Dyes on Magnetic Iron Oxide Nanoparticles. Part II: Field-Induced Nanoparticle Agglomeration and Magnetic Separation. Langmuir 37, 10612–10623. https://doi.org/10.1021/acs.langmuir.1c02021

Raffel, M., Willert, C.E., Scarano, F., Kähler, C.J., Wereley, S.T., Kompenhans, J., 2018. PIV Uncertainty and Measurement Accuracy, in: Particle Image Velocimetry. Springer International Publishing, Cham, pp. 203–241. https://doi.org/10.1007/978-3-319-68852-7_6

Rajan, A., Sahu, N.K., 2020. Review on magnetic nanoparticle-mediated hyperthermia for cancer therapy. J Nanopart Res 22, 319. https://doi.org/10.1007/s11051-020-05045-9

Rathore, Y.S., Rehan, M., Pandey, K., Sahni, G., Ashish, 2012. First Structural Model of Full-Length Human Tissue-Plasminogen Activator: A SAXS Data-Based Modeling Study. J. Phys. Chem. B 116, 496–502. https://doi.org/10.1021/jp207243n

Revia, R.A., Zhang, M., 2016. Magnetite nanoparticles for cancer diagnosis, treatment, and treatment monitoring: recent advances. Materials Today 19, 157–168. https://doi.org/10.1016/j.mattod.2015.08.022

Roger, S., Talbot, D., Bee, A., 2006. Preparation and effect of Ca2+ on water solubility, particle release and swelling properties of magnetic alginate films. Journal of Magnetism and Magnetic Materials 305, 221–227. https://doi.org/10.1016/j.jmmm.2006.01.005

Rosensweig, R.E., 1985. Directions in ferrohydrodynamics. Journal of Applied Physics 57 (8), 4259-4264

Russel, W.B., Saville, D.A., Schowalter, W.R., 1989. Colloidal Dispersions, 1st ed. Cambridge University Press. https://doi.org/10.1017/CBO9780511608810

Sandre, O., Browaeys, J., Perzynski, R., Bacri, J.-C., Cabuil, V., Rosensweig, R.E., 1999. Assembly of microscopic highly magnetic droplets: Magnetic alignment versus viscous drag. Phys. Rev. E 59, 1736–1746. https://doi.org/10.1103/PhysRevE.59.1736

Shen, Z., Wu, A., Chen, X., 2017. Iron Oxide Nanoparticle Based Contrast Agents for Magnetic Resonance Imaging. Mol. Pharmaceutics 14, 1352–1364. https://doi.org/10.1021/acs.molpharmaceut.6b00839

Sherman, Z.M., Swan, J.W., 2016. Dynamic, Directed Self-Assembly of Nanoparticles *via* Toggled Interactions. ACS Nano 10, 5260–5271. https://doi.org/10.1021/acsnano.6b01050

Shliomis, M.I., 2021. How a rotating magnetic field causes ferrofluid to rotate. Phys. Rev. Fluids 6, 043701. https://doi.org/10.1103/PhysRevFluids.6.043701

Sjöstrand, S., Evertsson, M., Jansson, T., 2020. Magnetomotive Ultrasound Imaging Systems: Basic Principles and First Applications. Ultrasound in Medicine & Biology 46, 2636–2650. https://doi.org/10.1016/j.ultrasmedbio.2020.06.014

Socoliuc, V., Bica, D., 2002. Experimental investigation of magneticinduced phase-separation kinetics in aqueous ferrofluids, in: Dékány, I. (Ed.), Adsorption and Nanostructure, Progress in Colloid and Polymer Science. Springer Berlin Heidelberg, Berlin, Heidelberg, pp. 131–135. https://doi.org/10.1007/3-540-45405-5_25

Socoliuc, V., Popescu, L.B., 2013. The role of the magnetically induced anisotropy of the pair correlation function in the dichroism of magnetic fluids. Journal of Magnetism and Magnetic Materials Volume 347, December 2013, Pages 146-152. https://doi.org/10.1016/j.jmmm.2013.07.067

Stikuts, A.P., Perzynski, R., Cēbers, A., 2020. Spontaneous order in ensembles of rotating magnetic droplets. Journal of Magnetism and Magnetic Materials 500, 166304. https://doi.org/10.1016/j.jmmm.2019.166304

Swan, J.W., Bauer, J.L., Liu, Y., Furst, E.M., 2014. Directed colloidal self-assembly in toggled magnetic fields. Soft Matter 10, 1102–1109. https://doi.org/10.1039/C3SM52663A

Swan, J.W., Vasquez, P.A., Whitson, P.A., Fincke, E.M., Wakata, K., Magnus, S.H., Winne, F.D., Barratt, M.R., Agui, J.H., Green, R.D., Hall, N.R., Bohman, D.Y., Bunnell, C.T., Gast, A.P., Furst, E.M., 2012. Multi-scale kinetics of a field-directed colloidal phase transition. Proc. Natl. Acad. Sci. U.S.A. 109, 16023–16028. https://doi.org/10.1073/pnas.1206915109

Szpak, A., Fiejdasz, S., Prendota, W., Strączek, T., Kapusta, C., Szmyd, J., Nowakowska, M., Zapotoczny, S., 2014. T1–T2 Dual-modal MRI contrast agents based on superparamagnetic iron oxide nanoparticles with surface attached gadolinium complexes. J Nanopart Res 16, 2678. https://doi.org/10.1007/s11051-014-2678-6

Talbot, D., Queiros Campos, J., Checa-Fernandez, B.L., Marins, J.A., Lomenech, C., Hurel, C., Godeau, G.D., Raboisson-Michel, M., Verger-Dubois, G., Obeid, L., Kuzhir, P., Bee, A., 2021. Adsorption of Organic Dyes on Magnetic Iron Oxide Nanoparticles. Part I: Mechanisms and Adsorption-Induced Nanoparticle Agglomeration. ACS Omega 6, 19086–19098. https://doi.org/10.1021/acsomega.1c02401

Thielicke, W., Sonntag, R., 2021. Particle Image Velocimetry for MATLAB: Accuracy and enhanced algorithms in PIVlab. JORS 9, 12. https://doi.org/10.5334/jors.334

Tsebers, A. O., 1982. Role of surface interactions in stratification of magnetic fluids, Vol. 18, No. 4, 21-27, 1982; English translation: Magnetohydrodynamics, Vol. 18, No. 4, 345-350.

Van De Ven TGM. 1989. Colloidal hydrodynamics. Academic press, New York

Wang, B. 2012 Rheology and magnetolysis of tumor cells. Doctoral dissertation, Université Nice Sophia Antipolis.

Wang, B., Bienvenu, C., Mendez-Garza, J., Lançon, P., Madeira, A., Vierling, P., Di Giorgio, C., Bossis, G., 2013. Necrosis of HepG2 cancer cells induced by the vibration of magnetic particles. Journal of Magnetism and Magnetic Materials 344, 193–201. https://doi.org/10.1016/j.jmmm.2013.05.043

Willis, A.J., Pernal, S.P., Gaertner, Z.A., Lakka, S.S., Sabo, M.E., Creighton, F.M., Engelhard, H.H., 2020. Rotating Magnetic Nanoparticle Clusters as Microdevices for Drug Delivery. IJN Volume 15, 4105–4123. https://doi.org/10.2147/IJN.S247985

Zaitsev, V.M., Shliomis, M.I., 1972. Coupled magnetoacoustic waves in a conducting paramagnetic fluid. Fluid Dyn 4, 15–17. https://doi.org/10.1007/BF01014963

Zubarev, A.Y., Iskakova, L.Yu., 2002. Theory of structural transformations in ferrofluids: Chains and "gas-liquid" phase transitions. Phys. Rev. E 65, 061406. https://doi.org/10.1103/PhysRevE.65.061406

Zubarev, A.Yu., Chirikov, D., Musikhin, A., Raboisson-Michel, M., Verger-Dubois, G., Kuzhir, P., 2021. Nonlinear theory of macroscopic flow induced in a drop of ferrofluid. Phil. Trans. R. Soc. A. 379, 20200323. https://doi.org/10.1098/rsta.2020.0323

Zubarev, A.Yu., Ivanov, A.O., 1997. Kinetics of a magnetic fluid phase separation induced by an external magnetic field. Phys. Rev. E 55, 7192–7202. https://doi.org/10.1103/PhysRevE.55.7192

Zubarev, A.Yu., Raboisson-Michel, M., Verger-Dubois, G., Kuzhir, P., 2020. To the theory of ferrohydrodynamic circulating flow induced by running magnetic field. Eur. Phys. J. Spec. Top. 229, 2961–2966. https://doi.org/10.1140/epjst/e2020-000119-3